Vortex state studies in a weakly pinned low T_c superconductor - $Ca_3Rh_4Sn_{13}$

Suresh Babu M

Department of Physics

Indian Institute of Technology Guwahati

This dissertation is submitted for the degree of

Doctor of Philosophy

October 2015

Dedicated to my family...

Declaration

I hereby declare that this thesis entitled **"Vortex state studies in a weakly pinned low T_c superconductor - $Ca_3Rh_4Sn_{13}$"** is the result of my own doctoral research work. This work was carried out under the supervision of Dr. Dilip Pal at the Department of Physics, Indian Institute of Technology Guwahati. To the best of my knowledge, the work presented in this thesis has not been submitted to any other Institute/University for the award of any degree.

Suresh Babu M
Research Scholar (Roll No: 09612132)
Department of Physics
Indian Institute of Technology Guwahati
Guwahati-781039, India

Certificate

It is certified that the work contained in the thesis entitled **"Vortex state studies in a weakly pinned low T_c superconductor - $Ca_3Rh_4Sn_{13}$"** by Suresh Babu M, a student of Department of Physics, Indian Institute of Technology Guwahati, for the award of the degree of Doctor of Philosophy has been carried out under my supervision. This work has not been submitted elsewhere for any degree.

Dr. Dilip Pal
Associate Professor
Department of Physics
IIT Guwahati
Guwahati-781039, India

Acknowledgements

I would like to begin by thanking my thesis supervisor Dr. Dilip Pal for introducing me to the world of Superconductivity and all the selfless help that he has rendered to me all times. I thank him for his excellent guidance and for pointing out my drawbacks which helped me to improve myself. Most of all, I would like to thank him for showing tremendous patience and tolerance as a supervisor. I always remember the long hours spent with him during the data analysis and writing papers.

I thank Dr. P. K Padmanabhan for helping me in molecular dynamic simulations. I also thank him for helping me whenever I approached him. I am also thankful to my doctoral committee members Prof. A. Srinivasan (Chairman), Prof. Saurabh Basu and Dr. Sandip Paul for reviewing my progress and for giving me their valuable comments and suggestions. I am thankful to the present and former head of the departments, Dr. P. Poulose and Prof. Saurabh Basu, for their friendly and approachable behaviour. I am also thankful to all the faculty members and staff of Physics department for their friendly behaviour and help. I am very thankful to the tax payers of India because without their tax i.e., their hard earned money, I could not get the MHRD fellowship.

I would like to express my sincere gratitude to Prof. A. K. Grover, Tata Institute of Fundamental Research (TIFR) mumbai (present Vice Chancellor, Punjab University) for his help in the whole experimental research work. During my visit in TIFR, he treated me as his own student and provided good support and full freedom for performing the experiments. I also express my sincere gratitude to Prof. Ramakrishnan and Prof. Thamizhavel of TIFR Mumbai for letting me avail various experimental facilities and for their immense support during my tenure there. I am also grateful to Prof. C. V. Tomy and his research student Santosh Kumar of IIT Bombay for providing me the ac susceptibility measurement facility. I also express my sincere thanks to Dr. Swati, Anil and Ulhas for their help in various experiments and making my TIFR visits successful.

I thank all my teachers especially Dr. Binoy Thomas, Dr. George Mamman, Dr. Binu P J, Dr. E M Mohammed, Dr. Hyson, Dr. Binoy Das, Dr. Seena and Dr. N Shaji whose efforts and blessings have helped me to reach here. I am thankful to my fellow research mates Dr. Padam Rajender, PC Lalngilnea and Ram Kumar for their friendly behaviour, helping nature

and cooperation. I am thankful to my senior, Dr. Sangeetha for her help in various research activities. I am thankful to my IITG friends Onkar, Deepanwita, Bappa, Jayjith, Bhargab, Shyni, Rejitha, Samit, Munendhar, Enam, Mukesh, Indrajith, Sanjeev, Deep, Abijit, Partha, Rohit, Himanshu, Sonu, Renjith, Jiss, Arun, Sandeep, Anoop, Sooraj .. etc. and others for creating a pleasant work environment and for helping me throughout my PhD career. I am also thankful to my friends Binu, Manoj, Jinaraj, Syam, Princy, Rajeev, Sreelesh etc. I am also thankful to Unnikrishnan B M and Padam Rajender for their help in correcting my thesis.

Last but not the least, I am extremely grateful to my parents, sister and family members for their love, care, support and encouragement throughout my life. I thank them for staying beside me in my good and bad days. I thank my well wishers and all people who have helped me directly or indirectly, whose name I may have inadvertently forgotten.

Synopsis

In type–II superconductors, the mixed phase of the (H-T) phase diagram has been constantly under purview both from experimental and theoretical view points, since its inception. After the discovery of high T_c superconductors [1], vortex phase diagram of conventional low T_c type–II superconductors like Nb [2, 3], 2H-$NbSe_2$ [4–6], YNi_2B_2C [7, 8], $Ca_3Rh_4Sn_{13}$ [9–12], etc. have been revisited several times to search for similarities/differences with that of the high T_c superconductors [9, 13–17]. This (H-T) phase diagrams are affected by a lot of parameters like coherence length (ξ), penetration depth (λ), static disorder, anisotropy, quantum fluctuations, temperature fluctuations, order parameter, etc. Hence, it is the natural interest of a physicist to study the various vortex phases and its transformations in the (H-T) phase space of a low T_c type–II superconductor to prove its genericness with that of the high T_c superconductors.

The critical current density (J_c), which arises due to the presence of inhomogeneities in the atomic lattice, has the potential to provide the information about the correlation volume (V_c) within the vortex matter, via the collective pinning description ($J_c \propto V_c^{-1/2}$) [18, 19]. Apart from the direct measurement, the information of this material attribute J_c, can be derived from the width of the magnetization hysteresis loop [20]. The two well documented anomalous features of the magnetization hysteresis loops observed in the mixed phase of the type–II superconductors are the second magnetization peak (SMP) and the peak effect (PE) phenomena. The PE phenomenon is interpreted as a rapid collapse of the elastic moduli of the vortex solid compared with that of the pinning force at the incipient flux line lattice melting transition [2, 21–25]. The SMP on the other hand is now widely accepted as a fingerprint of transition from a Bragg glass (BG) phase (i.e., a vortex state without topological dislocations) to a multi-domain vortex glass (VG) phase, a state with dislocations [11, 26–28].

Evidence has mounted over the years that the SMP line in the vortex phase diagram is temperature independent both in high T_c superconductors, like $Bi_2Sr_2CaCu_2O_8$ (BSCCO), $YBa_2Cu_3O_{7-\delta}$ (YBCO), etc., as well as in low T_c cubic superconductors, like $Ca_3Rh_4Sn_{13}$ [11, 14, 29], etc. In high T_c superconductor BSCCO, where the intrinsic pinning strength varies with the oxygen concentration, the usual temperature independent onset field of the SMP was reported to increase/decrease with enhancement in temperature and the notion of 'inverse melting' over a limited range of (H,T) values in a few crystals [16, 30]. But till today there is no report about the variation of the SMP line with various pinning strengths in low T_c superconductors.

Signatures of metastable effects across the SMP and PE regions have been observed and possible connections between the quenched random disorder and the spinodal nature of the above features have been derived [26, 31–33]. Further the small angle neutron scattering (SANS) measurements in MgB_2 have demonstrated the occurrence of a metastable state not related to pinning with a slightly different vortex lattice structure from that of the original structure [34]. Different vortex lattice structures, which may be a metastable one, leave an imprint as two depinning currents in a single current-voltage (I-V) characteristics [35]. Experiments have already been done to find the characteristic time scales for such metastable structures [36]. The coherent dynamics of the vortex lattice at various regions of the mixed phase is very intriguing.

Numerous reports about paramagnetic Meissner effect (PME) (a positive magnetization signal in the superconducting region) in both bulk and nano superconductors while field cooling the sample have raised considerable interest [3, 37–41]. One of the most probable explanation is the flux trapping on field cooling of the materials and its subsequent compression [40]. Theoretical model based on Ginzburg-Landau theory shows that various metastable states with positive and negative signs of magnetizations are possible in this PME region [42]. Hence, exploring the metastable magnetic states close to the normal to superconducting phase boundary will be of considerable interest.

The ternary stannide $Ca_3Rh_4Sn_{13}$ is an isotropic weakly pinned low T_c superconductor which shows most of the anomalous properties like SMP, PE, positive magnetization on field cooling (PMFC), etc. in its magnetization data [9, 10, 12, 40, 43–45]. Hence, this material provides an ideal platform to investigate both the static and dynamics properties of the mixed phase and its metastability effects. This thesis is focused on the results of magnetization

studies of one batch of these crystals ($T_c \propto 8.37$ K), which have slightly higher pinning strength (or J_c) than the previously reported $Ca_3Rh_4Sn_{13}$ single crystals [11].

The following chapters will be included in the thesis:

Chapter 1: This chapter briefly introduces the basic aspects of superconductivity and physics of vortices in type–II superconductors. It contains the Abrikosov's mean field description for explaining the incomplete shielding of the type–II superconductors. The three important deformations (compressed, tilt and shear deformations) of the hexagonal vortex lattice are discussed in detail. The effect of thermal fluctuations and quenched random disorder in the vortex lattice are included. The relation connecting J_c with the correlation volume (V_c) of the vortex lattice and the width of the magnetization hysteresis loop is discussed. For an easy understanding of the reported results of the thesis, brief descriptions of the SMP, PE, paramagnetic Meissner effect, surface superconductivity, etc. are included in this chapter. A short summary of the impacts of the metastability effects in the static magnetization measurements of type–II superconductors are also included in this chapter.

Chapter 2: This chapter explains the experimental tools used to carry out the present work. A small introduction about the preparation of the $Ca_3Rh_4Sn_{13}$ single crystal is included along with the X-ray Laue diffraction pattern of the crystal. The working principles of commercial superconducting quantum interference device - vibrating sample magnetometer (SQUID-VSM) is discussed in this chapter. The basic measurement principles of the ac susceptibility measurements are also discussed.

Chapter 3: This chapter deals with the magnetization studies on one of the single crystal sample of $Ca_3Rh_4Sn_{13}$ which is a weakly pinned low T_c type–II superconductor. The vortex phase diagram of the single crystal (*cf.* Fig.1) shows a well ordered Bragg glass phase which is sandwiched between the multi-domain vortex glass and an amorphous vortex state in a portion of the field–temperature phase space. The non-monotonic variation of the SMP anomaly in the magnetization hysteresis loops is akin to the inverse melting phenomenon reported earlier only in samples of high T_c superconductors [30]. This chapter also narrates a step change in the equilibrium magnetization across the SMP and PE regions, which is a suggestive feature of the first order phase transition. We have determined a lower field limit (like a spinodal line) of the transition to the vortex glass phase via the identification of the SMP anomaly in the ac susceptibility measurements, where shaking of the vortex matter can facilitate the accession of the underlying equilibrium phase.

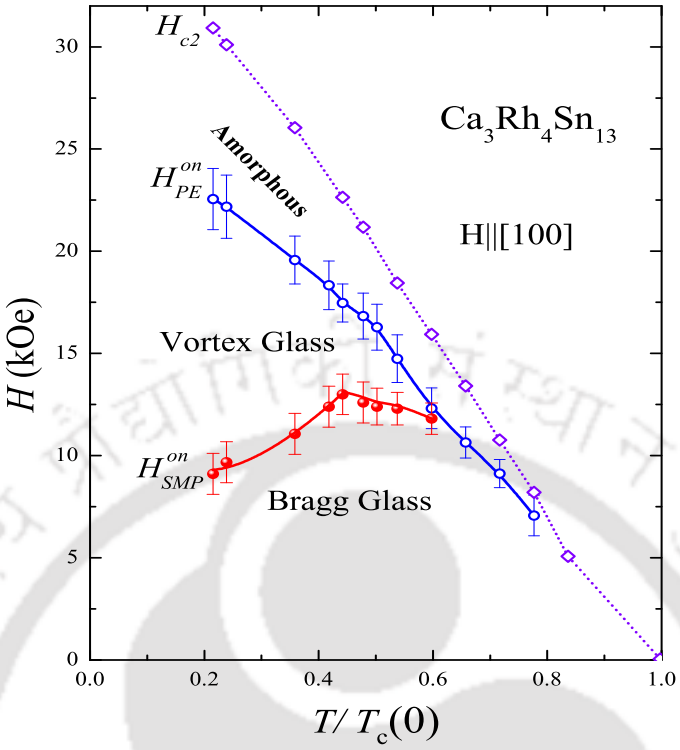

Figure 1: *Vortex phase diagram in $Ca_3Rh_4Sn_{13}$ with H||[100]. The onset positions of the SMP and PE anomalies are denoted as H^{on}_{SMP} and H^{on}_{PE}, respectively. The non-monotonic behavior of the H^{on}_{SMP} indicates the inverse melting nature of the vortex system.*

We have also made attempts to understand the spectral fluctuations in noise in magnetization data of $Ca_3Rh_4Sn_{13}$ single crystal across the SMP and PE anomalous region. The signature of $1/f$ noise deep inside the mixed phase of this superconductor is observed. This may be the indication of the self-organized critical nature of the ordered state of the vortex lattice. Further across the SMP region, a single resonance frequency appears in the power spectra and it persists till the superconducting to normal phase boundary. While crossing the PE anomaly another set of resonance peaks in the low frequency range emerges which is distinctly different from the one which appeared in the SMP, indicating the underlying difference in the origin and nature of the SMP and PE phenomena. The zero temperature molecular dynamics simulation studies of the dynamic vortices also show the $1/f$ nature of the noises in its power spectrum.

Chapter 4: This chapter is devoted to the stable field mode dc magnetization studies of the $Ca_3Rh_4Sn_{13}$ single crystal. The observation of sudden shifts in the *M-H* curve in

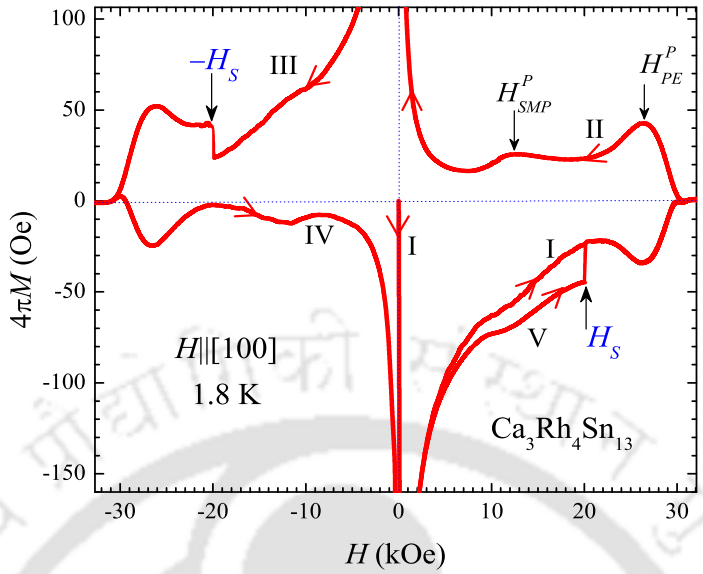

Figure 2: *Five quadrant M-H loop of $Ca_3Rh_4Sn_{13}$ single crystal at T = 1.8 K recorded by the stable field mode method. The sudden magnetization shift observed in the third (III) and fifth (V) quadrants are denoted as $-H_S$ and H_S, respectively.*

the stable field mode magnetization measurements (*cf.* Fig. 4.2) revealed the existence of two J_c states in the same magnetic field and temperature. The two critical current densities indicate the possibility of two vortex lattice structure configurations present in the system. The relaxation of magnetization allows it to go to the new J_c state. Increasing the applied magnetic field after field cooling the sample also results in the new J_c state.

Chapter 5: The positive magnetization on field cooling (PMFC) and surface superconductivity effects of the $Ca_3Rh_4Sn_{13}$ single crystal are studied in this chapter. The field dependance of the PMFC region is studied. The observed paramagnetic state is found to be metastable and the diamagnetic state can be restored by changing the external measurement conditions. The vibration amplitude dependance of the $Ca_3Rh_4Sn_{13}$ single crystal enables the switching of the metastable magnetic states from paramagnetic to diamagnetic region in the PMFC region (*cf.* Fig. 5.3). We have tried to explain the switching behavior using the notion that the paramagnetic effect is a surface effect which is amalgamated with the conventional diamagnetic effect which arises from the bulk. The phase diagram constructed shows a clear distinction between the surface superconductivity and upper critical field in

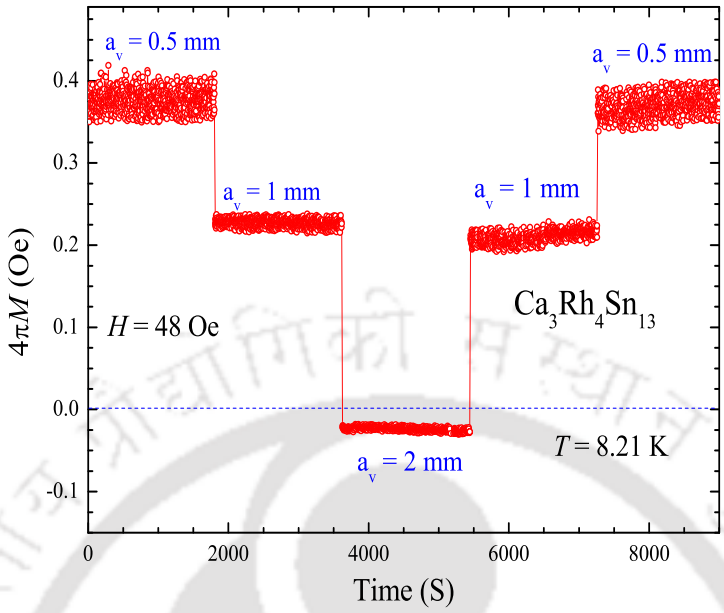

Figure 3: *Magnetization vs. time plots while changing the vibration amplitudes (a_v) at the PMFC region of the field-cooled cool-down magnetization curve at H = 48 Oe and T = 8.21 K. A momentarily change in a_v switches the magnetization from one state to another. Changes in a_v are made in a time interval of 1800 seconds everywhere.*

the low temperature region and they eventually merge near the superconducting transition temperature.

Chapter 6: This chapter is devoted for the comprehensive summary of the over all work undertaken in the present thesis.

Publications/Conference Proceedings

1. **M. Suresh Babu** and D. Pal, Study of the noise in the magnetization data across the second magnetization peak and peak effect region in $Ca_3Rh_4Sn_{13}$, *Physica C: Superconductivity* **505** (2014) 85-88.

2. **M. Suresh Babu** and D. Pal, Step change in equilibrium magnetization across the second magnetization peak and peak effect region of a weakly pinned low T_c superconductor, $Ca_3Rh_4Sn_{13}$, *Physica B: Condensed Matter* **448** (2014) 188-190.

3. **M. Suresh Babu** and D. Pal, Structural transitions in driven vortices of weakly pinned superconductors, *AIP Conf. Proc.* **1591** (2014) 1636.

4. **M. Suresh Babu**, A. Thamizhavel, S. Ramakrishnan, C. V. Tomy, A. K. Grover and D. Pal, Identification of the inverse melting line in the vortex phase diagram of a low T_c superconductor, $Ca_3Rh_4Sn_{13}$, *Superconductor Science and Technology* **26** (2013) 125016.

5. **M. Suresh Babu**, A. Thamizhavel, S. Ramakrishnan, A. K. Grover and D. Pal, Observation of two critical current densities in a weakly pinned single crystal of $Ca_3Rh_4Sn_{13}$, *AIP Conf. Proc.* **1536**, (2013) 855.

6. **M. Suresh Babu** and D. Pal, Noise Analysis of Driven Vortices of type–II Superconductors – A Molecular Dynamics Study, *AIP Conf. Proc.* (*accepted for publication*).

7. **M. Suresh Babu**, A. Thamizhavel, S. Ramakrishnan, A. K. Grover and D. Pal, Switching of magnetization in the positive magnetization region of a weakly pinned low T_c superconductor, $Ca_3Rh_4Sn_{13}$ (*Under Review:- Appl. Phys. Lett.*).

8. **M. Suresh Babu**, A. Thamizhavel, S. Ramakrishnan, A. K. Grover and D. Pal, Determination of two critical current densities from the magnetization measurements of a low T_c type–II superconductor, $Ca_3Rh_4Sn_{13}$ (*Communicated*).

Conference Presentations

1. 59^{th} DAE Solid State Physics Symposium (DAE-SSPS-2014), Department of Physics, VIT University, Vellore, India 16-20 December 2014.

2. International Conference on Magnetic Materials and Applications (ICMAGMA-2014), Department of Physics, Pondicherry University, Pondicherry, India 15-17 September 2014.

3. Asia Sweden Meeting on Understanding Functional Materials From Lattice Dynamics (ASMFLD-2014), Department of Physics, IIT Guwahati, Guwahati, India 9-11 January 2014.

4. 58^{th} DAE Solid State Physics Symposium (DAE-SSPS-2013), Department of Physics, Thapar University, Patiala, India 17-21 December 2013.

5. International Conference on Magnetic Materials and Applications (MagMA-2013), Department of Physics, IIT Guwahati, Guwahati, India 5-7 December 2013.

6. International Conference On Recent Trends In Applied Physics and Material Science (RAM-2013), Department of Physics, College of Engineering and Technology, Bikaner, India 1-2 February 2013.

Table of contents

List of figures

List of abbreviations/symbols

λ —— Penetration depth

ΔT_c —— Transition width

BG —— Bragg glass

BSCCO —— $Bi_2Sr_2CaCu_2O_8$

c_{11} —— Compression modulus

c_{44} —— Tilt modulus

c_{66} —— Shear modulus

C_L —— Lindemann number

d —— Unit cell distance along the [100] axis

DME —— Diamagnetic Meissner effect

FC —— Field cooled

FCW —— Field cooled warm-up

FLL —— Flux line lattice

G_i —— Ginzburg number

GL —— Ginzburg-Landau

h_{ac} —— ac amplitude

H_c —— Critical field

H_{c1} —— Lower critical field

H_{c2} —— Upper critical field

H_{PE}^{on} —— Onset of peak effect

H_{PE}^{p} —— Peak of peak effect

H_{SMP}^{on} —— Onset of second magnetization peak

H_{SMP}^{p} —— Peak of second magnetization peak

J_c —— Critical current density

k_B —— Boltzman constant

M_{eq} —— Equilibrium magnetization

M_{FCC} —— Field-cooled cool-down magnetization

M-H —— Magnetization vs. magnetic field

M-t —— Magnetization vs. time

M-T —— Magnetization vs. temperature

NNN —— Number of nearest neighbours

PE —— Peak effect

PME —— Paramagnetic Meissner effect

PMFC —— Positive magnetization on field cooling

PPMS —— Physical property measurement System

S —— Entropy

SANS —— Small angle neutron scattering

SMP —— Second magnetization peak

SQUID —— Superconducting Quantum Interference Device

STM —— Scanning tunneling microscopy

T_c —— Transition Temperature

T_{c3} —— Onset temperature point of surface superconductivity

T_{irr} —— Irreversibility temperature point

T_m —— Melting temperature

V_c —— Correlation volume

VG —— Vortex glass

VL —— Vortex lattice

VSM —— Vibrating sample magnetometer

χ' —— In-phase ac susceptibility

YBCO —— $YBa_2Cu_3O_{7-\delta}$

ZFC —— Zero field cooled

ε —— Anisotropy constant

κ —— Ginzburg-Landau parameter

ξ —— Coherence length

ϕ_0 —— Magnetic Flux quantum

$\Psi(r)$ —— Superconductig order parameter

Chapter 1

Introduction

1.1 Superconductivity

One of the important milestone in the history of physics is the discovery of superconductivity by a Dutch scientist H. K. Onnes [49] in 1911. He discovered that the dc electrical resistivity of mercury abruptly disappeared below a critical temperature (T_c) $\approx$ 4.2 K. The outlining property of a superconductor which distinguishes it from a perfect conductor is perfect diamagnetism due to magnetic flux expulsion and the phenomenon is known as Meissner effect [50]. It was later found that one can destroy the superconductivity by applying an external magnetic field higher than a critical field (H_c). Later F. London and H. London [51] proposed the phenomenological theory by combining the two superconducting basic properties: zero resistivity and Meissner effect. They considered the superconductivity as a quantum phenomenon and established the electromagnetic property of superconductors. They also found that the applied magnetic field falls off exponentially to the interior of a superconductor within a length scale λ, where λ is known as the London penetration depth. Another important formalism – the phenomenological description of superconductivity came from Ginzburg and Landau in 1950 [52]. Their formalism describes the superconducting state by an order parameter $\Psi(r)$, where $\Psi(r) = |\Psi(r)|\exp[i\phi(r)]$. Here $\Psi(r)$ denotes the wave function of the superconducting electrons and $\phi(r)$ is the phase field of the order parame-

ter. Normalized Ψ gives the density of the superconducting electrons ($|\Psi|^2 = n_s$) and in the normal state n_s=0. Ginzburg and Landau also introduced the next fundamental length scale, ξ known as coherence length for describing the superconducting state. A microscopic theory for explaining superconductivity was given by Bardeen, Cooper and Schrieffer in 1957 known as the BCS theory [53]. The BCS theory revealed that the superconducting state contains bound electron pairs (Cooper pairs) which are responsible for the superconductivity. The BCS theory also predicted the presence of an energy gap between the normal and superconducting states. The discovery of high T_c superconductivity in Ba-La-Cu-O systems by Bednorz and Müller [1] in 1986 created a revolution in the history of superconductivity. After the discovery of high T_c superconductors, vortex phase diagram of conventional low T_c type – II superconductors have been revisited several times to search for similarities/differences with that of the high T_c superconductors.

1.2 Type – I and Type – II superconductors

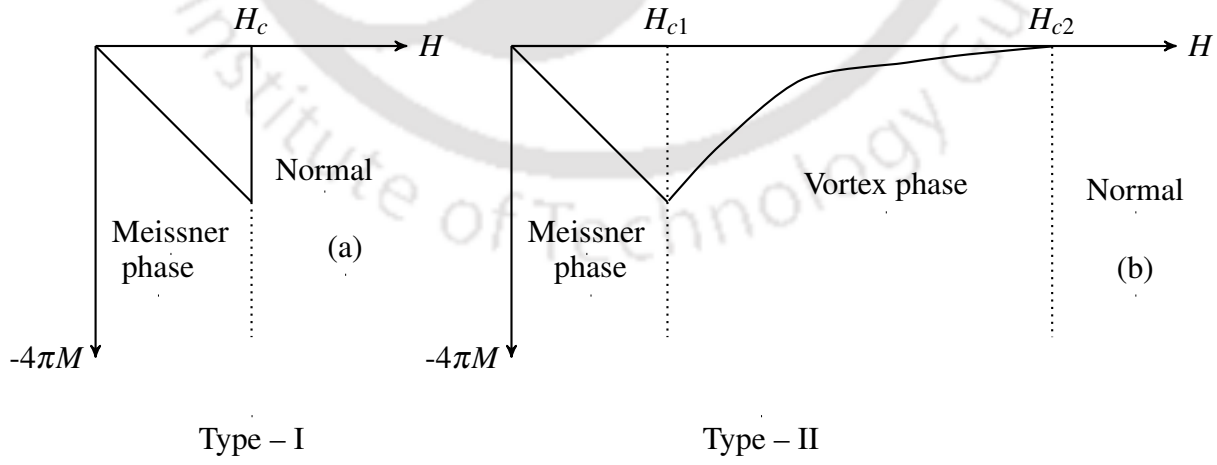

Figure 1.1: *Magnetization (M) vs. applied magnetic field (H) variation of (a) type – I and (b) type – II superconductors.*

Depending on the amount of the applied magnetic field (H), superconducting materials exist in normal or superconducting state. One can observe a perfect diamagnetism in a material if the material has a magnetization (M) identical in magnitude and reverse in direction to the applied magnetic field. It is known that $B = \mu_0(H+M)$, and expulsion of B from the bulk of the superconductor requires an energy $\frac{1}{2}\mu_0 H^2$ per unit volume.

The superconducting condensation energy is the energy difference between the free energies per unit volume of the material in the normal (F_n) and superconducting (F_s) states. Hence, as long as this magnetic energy is less than the condensation energy, it remain superconducting. Superconductivity is destroyed and the normal state is arrived, with complete magnetic flux penetration, by the introduction of a critical magnetic field $H_c(T)$ where $\frac{1}{2}\mu_0 H_c^2(T) = F_n(T) - F_s(T)$.

The magnetic response of superconductors are shown in Fig. 1.1 as magnetization (M) vs. magnetic field (H). Type – I superconductor show complete shielding of magnetic fields up to a critical field H_c and above H_c the material reaches the normal state. However, type – II superconductors show incomplete shielding, i.e., the magnetic flux start to penetrate above a certain field $H_{c1}(T)$ creating normal cores surrounded by superconducting currents. If the applied magnetic field is greater than $H_{c2}(T)$ – the upper critical field, then the type – II superconductor becomes a normal conductor.

One can define the magnetic field response of a superconductor with the help of a parameter, κ, known as the Ginzburg-Landau (GL) parameter where $\kappa = \lambda(T)/\xi(T)$. Also, it is possible to categorize the superconductors depending on the value of κ. It is observed that for type – I superconductors $\kappa < \frac{1}{\sqrt{2}}$ and for type – II superconductor $\kappa > \frac{1}{\sqrt{2}}$. κ is usually considered to be constant for most materials, and is weakly dependent on temperature. The value of κ is very small for conventional superconductors [47, 54]. Between H_{c1} and H_{c2}, the magnetic flux penetrates in quantized units and the quanta of a magnetic flux is known as a vortex.

1.3 Abrikosov vortices

Alexei Alexeyevich Abrikosov, a Russian theoretical physicist obtained a periodic solution of the phenomenological theory of Ginzburg and Landu [52] for explaining the incomplete shielding of the type – II superconductors under the mean field description. Abrikosov derived the spatially periodic solution of the linearized GL equations when a magnetic field (say along z-direction) is applied to a superconductor [55] as:

$$\psi_L(x,y) = \sum_m C_m \psi_m = \sum_m C_m e^{imqy} e^{[-(x-x_m)^2/2\xi^2]}, \tag{1.1}$$

which is periodic in y by construction and, also, periodic in x, if $C_{m+v} = C_m$ (periodic). The value of v = 1 corresponds to a square lattice periodicity and v = 2 corresponds to a triangular lattice periodicity. The above solution describes the mixed state (incomplete shielding state) or the Abrikosov phase of a type – II superconductor. The superconducting order parameter vanishes periodically at x_m and remains suppressed within a further distance of ξ in the mixed phase. In the mixed phase, the applied magnetic field penetrates the superconductor and decays a length scale of λ. So each term in the above solution represents a vortex (flux line) with the central normal region called as the core. Due to the gradient in magnetic field, the vortex core is threaded by circulating supercurrents ranging up to λ. The fourth Maxwell's equation, $\nabla \times B = \mu_0 J$, leads to the presence of circulating supercurrents J around the core ξ. Each vortex of the superconducting specimen carries one quantum of magnetic flux, $\phi_0 = \frac{hc}{2e} = 2.07 \times 10^{-7}$ G-cm^2. The magnetic field around a vortex is given by the equation:

$$h(r) = (\phi_0/2\pi\lambda^2) K_0(r/\lambda), \tag{1.2}$$

where $K_0(r/\lambda)$ is a zeroth order Hankel function, which decays exponentially at large r and varies logarithmically for $\xi << r << \lambda$. Equation 3.3 is derived for the case of a large κ superconductor where one can approximate the vortex core as completely normal.

The vortices repel each other due to the supercurrents flowing around them. The interaction energy between two vortices separated by a distance r is given by the equation:

$$F = \frac{\phi_0^2}{8\pi^2\lambda^2} K_0(r/\lambda), \tag{1.3}$$

It is observed that for large distances the inter-vortex interaction falls exponentially and for small distances it varies logarithmically.

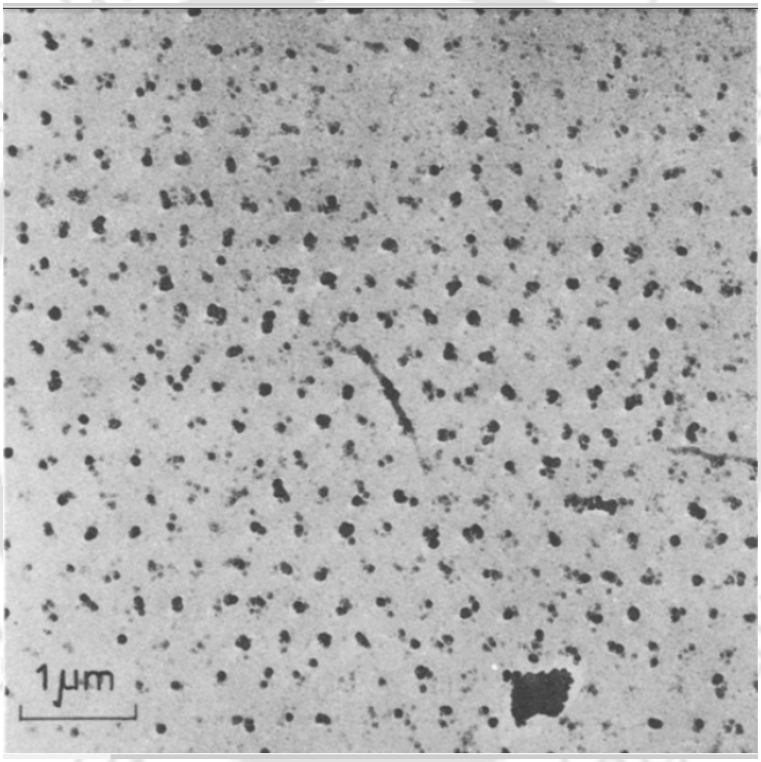

Figure 1.2: *First experimental visualization of triangular Abrikosov's vortex lattice on the surface of a lead alloy rod by Bitter decoration technique [Courtesy [46]].*

In between H_{c1} and H_{c2}, the Abrikosov's solution (1.1) shows that the vortices are organized in the form of a lattice called the flux line lattice (FLL) or Abrikosov's vortex lattice, which is entrenched in the atomic lattice. The triangular lattice corresponds to the minimum energy configuration and each vortex in the minimum energy configuration is surrounded

by six other vortices (hexagonal lattice). The nearest-neighbor distance for the triangular vortex lattice:

$$a_\Delta = (4/3)^{1/4}(\phi_0/B)^{1/2} = 1.075(\phi_0/H)^{1/2}, \tag{1.4}$$

From the above equation it is clear that one can tune a_Δ simply by changing the applied magnetic field H. The first direct observation of Abrikosov lattice in superconductors were obtained by Essmann and Trauble in 1967 using the Bitter decoration method in Pb-4at%In and Nb specimens [46].

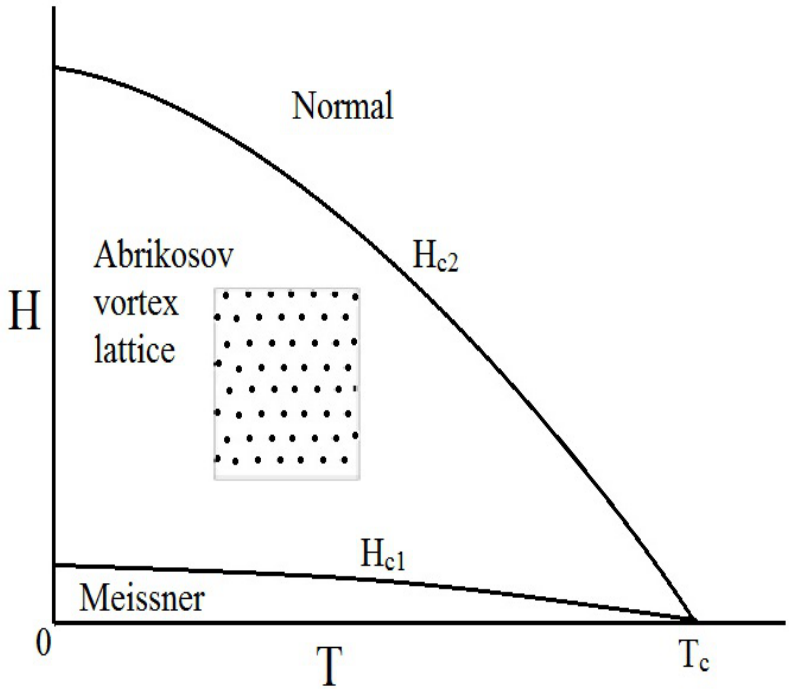

Figure 1.3: *The mean field (H–T) phase diagram of a typical type – II superconductor.*

Fig. 1.3 shows a schematic representation of mean field phase diagram of a type – II superconductor consisting of a normal, a mixed and a Meissner phase. In the mixed phase of a clean superconductor, the Abrikosov's vortex lattice have seamless translational invariance, $\nabla \times \vec{B} = 0$ and therefore, it does not withstand any current density. Let us consider

the effect of an external current $\vec{J}$ on a FLL configuration, with $\vec{J}$ being applied perpendicular to the magnetic field $\vec{B}$. Due to the Lorentz force, $\vec{F_L} = \vec{J} \times \vec{B}$, the flux lines start to move in a direction perpendicular to the applied current, which leads to a finite dissipation, and the zero resistance property of the superconductor is jeopardized. To stop the movement of the vortices, presence of an opposing force is desirable. Pinning centers usually act as the source of this force. Let $\vec{F_p}$ be the force arising from the pinning centers. As long as $\vec{F_L}$ does not exceed $\vec{F_p}$, vortices will not move from their positions. At a critical value of the current density, $\vec{J_c}$ known as the critical current density, $\vec{F_L} = \vec{J_c} \times \vec{B} = \vec{F_p}$. So, $\vec{J_c}$ is a measure of pinning or disorder present in a type – II superconductor.

1.4 Elastic properties of the vortex lattice

Interaction between the vortices impart elasticity to the vortex lattice. The notion of elasticity of the magnetic flux lines was put forward by Maxwell who explained the forces on systems in relation to line tension and compressibility of the field. Silcox and Rollins [56, 57] were the first to describe the elastic constants by considering the interaction between the neighboring vortices and later Labusch [58] calculated whole elastic constants by considering the appropriate derivatives of the free energy of the vortex assembly. In the usual notation, stresses, σ_i are linked with the strains, ε_j, by $\sigma_i = c_{ij}\varepsilon_j$. Here, i accepts values from 1 to 6 which refers to the suffixes xx, yy, zz, yz, xz and xy, respectively, and $\varepsilon_{xx} = \partial u_x/\partial x$ and $\varepsilon_{xy} = \partial u_x/\partial y + \partial u_y/\partial x$ where u is the displacement of the lines. The z axis is taken to be parallel to the flux lines and the hexagonal lattice in the xy plane is isotropic. In the z direction, the length of the vortex line is infinite, hence, the line tension is independent of length and so these forces cannot dependent on ε_3. Consequently, all the elements in the 3^{rd} column and, by symmetry, these in the 3^{rd} row of the c_{ij} tensor are zeros. Thus the Hooke's law takes the form

$$\begin{pmatrix} \sigma_{xx} \\ \sigma_{yy} \\ \sigma_{yz} \\ \sigma_{xz} \\ \sigma_{xy} \end{pmatrix} = \begin{pmatrix} c_{11} & c_{12} & 0 & 0 & 0 \\ c_{12} & c_{11} & 0 & 0 & 0 \\ 0 & 0 & c_{44} & 0 & 0 \\ 0 & 0 & 0 & c_{44} & 0 \\ 0 & 0 & 0 & 0 & c_{66} \end{pmatrix} \begin{pmatrix} \varepsilon_{xx} \\ \varepsilon_{yy} \\ \varepsilon_{yz} \\ \varepsilon_{xz} \\ \varepsilon_{xy} \end{pmatrix}$$

with the condition that $2c_{66} = c_{11} - c_{12}$. The 3 elastic moduli: compression modulus (c_{11}), tilt modulus (c_{44}) and shear modulus (c_{66}) are only needed (see Fig. 1.4) for a comprehensive understanding of the elastic nature of the vortex lattice [59, 60].

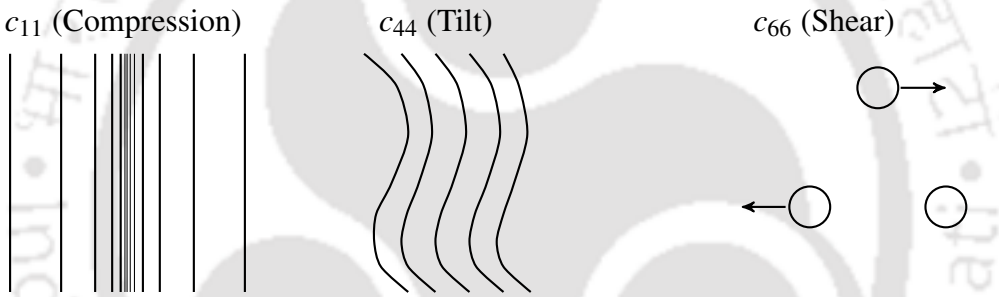

Figure 1.4: *Three different deformations of the hexagonal vortex lattice leading to three different elastic moduli, viz., c_{11} for compressed deformations, c_{44} for tilt deformations and c_{66} for the shear deformation.*

The elastic moduli of the triangular vortex lattice for uniform distortions as follows:

$$c_{11} - c_{66} = (B^2\mu_0)(\partial H/\partial B), \tag{1.5}$$

$$c_{44} = BH/\mu_0, \tag{1.6}$$

$$c_{66} = (B\phi_0/16\pi\lambda^2\mu_0)(1-\frac{1}{2\kappa^2})(1-b)^2(1-0.58b+0.29b^2), \tag{1.7}$$

where $b = B/B_{c2}$. The above equations are valid in the long wavelength limit (vortices are loosely packed) of the lattice deformations. In the short wavelength limit (vortices are closely packed), the non-local effects must be taken into consideration. The wavelength (k) dependent elastic constants, $c_{11}(k)$ and $c_{44}(k)$ get modified as [59]

$$c_{11}(k) \approx c_{44}(k) \approx (B^2/\mu_0)(1+ \mid k \mid^2 \lambda^2)^{-1}. \tag{1.8}$$

Abrikosov's mean field picture predicts a rigid and perfectly hexagonal vortex lattice throughout the mixed phase space. But, the above equations show that the elastic constants are dependent on the precise location of wave vector in the phase space. Thus, in a phase diagram the rigidity of the vortex lattice is also different in different regions.

1.5 Beyond the mean field description

Generally, all superconducting specimen inherently has a certain amount of quenched random disorder (point defects) in the form of vacancies, interstitial impurity atoms, etc. A vortex line is energetically favorable to stay in the potential well of the point defects (pinning of the vortex lines) and hence deviates from its equilibrium position, leading to a modification in the mean field description of the vortex state. In addition to the point defects, thermal disorder, also makes modifications in the mean field phase diagram.

1.5.1 Thermal Fluctuations

Thermal fluctuations can make considerable modifications on the vortex lattice structures by changing its elastic properties. The quenched random disorder is static but the thermal disorder is dynamic. Thermal fluctuations can create changes in the mean field (H-T) phase diagram of a superconductor. The vortices can displace from its position because of thermally activated jumps. Sometimes even at $J < J_c$, theses jumps overcomes the pinning

potential barrier and make a flux creep phenomenon and this affects the dissipation-free current flow criteria for the superconductors. The fundamental parameter which governs the strength of the thermal fluctuation is known as the Ginzburg number G_i which is defined by the equation:

$$G_i = \frac{1}{2}\left(\frac{k_B T_c}{H_c^2(0)\varepsilon\xi^3(0)}\right)^2 \tag{1.9}$$

where k_B represents the Boltzmann constant, ε is the anisotropy parameter, and H_c is the thermodynamical critical point. Qualitatively, G_i suggests the ratio of the thermal energy $k_B T_c$, with respect to condensation energy $H_c^2(0)\varepsilon\xi^3(0)$ at temperature $T = 0$ within a coherence volume. Due to large T_c and small coherence length ξ, thermal fluctuations are usually strong in high T_c superconductors ($G_i \sim 10^{-2}$). But in conventional low T_c type – II superconductors the thermal fluctuations are quite small ($G_i \sim 10^{-8}$) and negligible.

It is observed that close to the normal to superconducting transition boundary $\mid \Psi \mid$ is subjected to high thermal fluctuations. These large thermal fluctuations may lead to the melting transition [61] via the transformation of a vortex solid into a vortex liquid. The phenomenological Lindemann criterion was proven successful for explaining the melting transition of first order nature [62, 63] of the flux line lattice. The Lindemann criterion states that a crystal lattice melts in a situation when the thermally driven displacement u_T of an atom becomes significant fraction of a_0, where a_0 is the lattice spacing. The conventional form of Lindemann criterion of the melting of flux line lattice is formulated by the equation:

$$\left\langle u^2(T_m)\right\rangle_T \simeq c_L^2 a_0^2 \tag{1.10}$$

where $\langle ... \rangle_T$ denotes the thermal average and the proportionality constant c_L is the Lindemann number, which usually varies from 0.1 to 0.2 [64, 65]. With the help of elastic description one can also calculate the melting of flux line lattice. An easy calculation of the vortex solid gives [66],

$$T_m/c = c_L^2 a_0^2 \tag{1.11}$$

From eqn. 1.11, one can notice that an increase in the applied magnetic field (or decrease in the lattice spacing, a_0) makes T_m to go down, where T_m is the melting temperature. Researchers have already reported the significance of the Ginzburg number and have connected the thermal fluctuations of the width of the critical regime to that of the melting line via the equation [61, 62, 64, 65]

$$H_m(T) \approx 5.6 \frac{c_L^4}{G_i} H_{c2}(0) \left(1 - \frac{T}{T_c}\right)^2 \tag{1.12}$$

It is worth to mention that the $H_m(T)$ line will be well separated from the H_{c2} line if the superconductors have large G_i. Hence, in high T_c superconductors the melting phenomenon would easily be distinct from the superconducting-normal transition.

1.5.2 Quenched random disorder

Quenched random disorders in the vortex matter leads to the existence of a finite J_c in the superconducting system. When the vortex system is subjected to an applied current density ($\vec{J}$), the vortices start moving under the influence of Lorentz force with a velocity $\vec{v}$,

$$\vec{F_L} = \frac{1}{c} \vec{J} \times \vec{B}, \tag{1.13}$$

Within a perfectly homogenous system, $\vec{F_L}$ is only counteracted by frictional force,

$$\vec{F_\eta} = -\eta \vec{v} \tag{1.14}$$

where η is the coefficient of viscosity. Due to the vortex motion, there is a power dissipation in the system because of the appearance of an electric field $\vec{E} = \frac{1}{c}\vec{B} \times \vec{v}$, and consequently a power $\vec{P} = \frac{1}{c^2 \eta}(\vec{J} \times \vec{B})^2$. So, the superconducting property – the dissipation less current flow will be lost. To overcome this problem, it is desirable to have an opposing force which

prevents this motion. Pinning centers are the sources of this force and known as pinning force $\vec{F_{pin}}$. Therefore,

$$\vec{F_L} = -\frac{1}{c}\vec{J_c} \times \vec{B} = \vec{F}_{pin} \tag{1.15}$$

Here J_c is the critical value of current density below which the flux lines are immobilized and there is dissipation free current flow. The quenched random disorder has important consequences in the vortex phase diagram because of the destruction of the triangular vortex lattice. Superconductors which which are useful in practical applications require high critical current density, J_c.

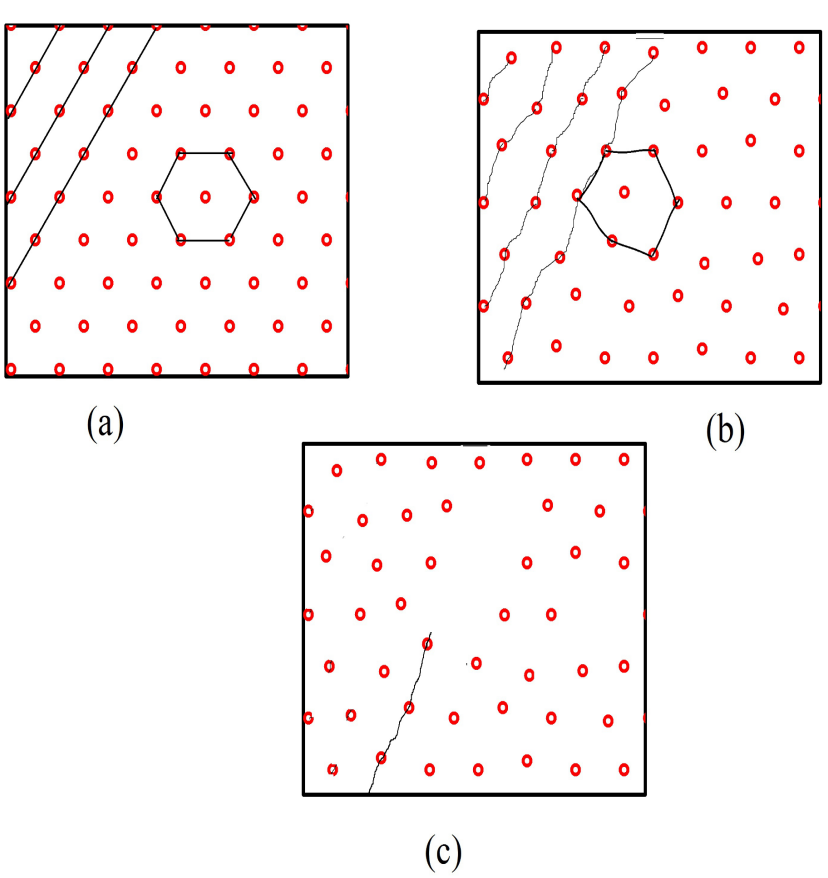

Figure 1.5: *(a) An Abrikosov vortex lattice have hexagonal lattice with perfect lattice spacing. (b) The Bragg glass (BG) which have distorted hexagonal lattice. The straight lines in the panel (a) have changed to distorted lines in the panel (b). (c) The vortex glass (VG) is distinguished by the presence of dislocations.*

As mentioned earlier, the disorder can destroy the translational order of the vortex lattice and create dislocations. Such a disordered vortex lattice with dislocations in a superconducting specimen is called the *vortex glass* (VG). Giamarchi and Le Doussal [26, 27, 67] have proved that the consequence of disorder on the flux line lattice is less vicious than expected which was also revealed by the neutron diffraction experiments [68]. When the nonlinear effects of the disordered system was taken into account, it was observed that far from loosing the translational order in an exponential fashion, the vortex system contains a quasi-long range order. Hence, the dislocations do not get originated if the disorder is moderate, and the algebraic divergent Bragg peaks in the neutron diffraction exist in these systems. This kind of vortex systems have several metastable states with divergent barriers. Even though it is an ordered solid, but having a glassy nature if one look at the dynamic properties. It is significantly different from that of the VG phase and has been named as *Bragg glass* (BG) phase. The BG phase does not have any defects such as dislocations and maintains quasi-long range order. Fig. 1.5 shows the different vortex lattice phases - Abrikosov lattice, Bragg glass and vortex glass in panels (a), (b) and (c), respectively.

Collective pinning theory

The pinning sites compete with one another for effective pinning of the flux line by forcing to twist and turn the flux line. Lubusch [58] calculated the pinning force by statistical averaging of an infinite set of pinning force densities and argued that below a threshold value of the pinning force, the contribution of pins will be zero in the vortex systems. In the limit of weak pinning and assuming the pin distribution as random, a model based on the collective pinning was derived by Larkin and Ovchinnikov (L.O) [18, 19, 69]. The main feature of L.O collective pinning arising from weak pins is the break down of the long-range order of the vortex lattice. However, a short range order of the vortex lattice still survives within a microscopic volume, V_c, within the sample, known as the correlation volume. This correla-

tion volume has a longitudinal correlation length, L_c, along the magnetic field direction and transverse correlation length, R_c, over which the vortices maintain a six-fold symmetry (i.e., $V_c \approx R_c^2 L_c$). Fig. 1.6 represents a schematic diagram of the correlation lengths within the collective pinning theory.

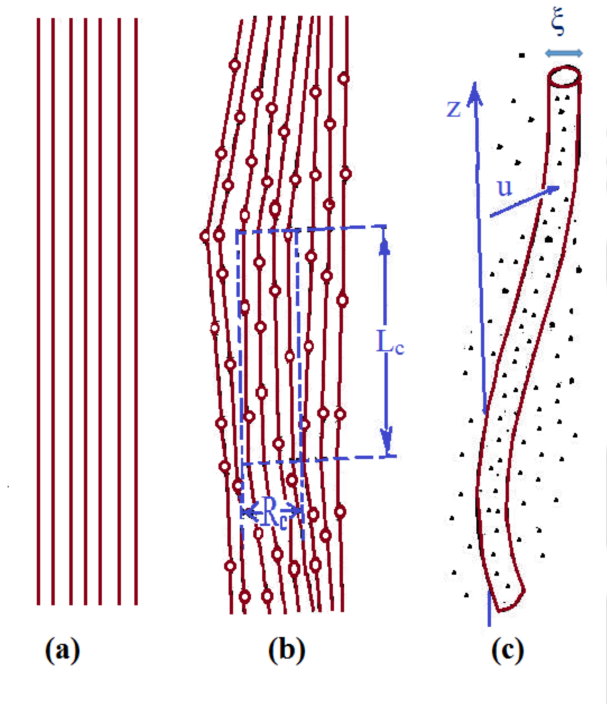

Figure 1.6: *(a) A configuration of straight rigid vortex lines in an ideal superconductor. (b) Correlation volume $R_c^2 L_c$ over which the order is preserved. (c) A vortex line in the presence of pinning centers (black dots) deviates a distance u from its ideal straight line behavior [Courtesy [47]].*

Typically the pins present inside the superconducting sample are weak and cannot effectively pin a vortex, and a large number of them are necessary for pinning action. The effective pinning at any point of the FLL arises due to the spatially random quenched pins and is directly related to the fluctuation in the density of pins n_p at that point. The random pinning forces would add up like in a random walk problem, giving a net total force, which increases as $\sqrt{V_c}$ or $\sqrt{N}$, where $N = n_p V_c$ is the total number of pinning centers in the Larkin volume, V_c. The Lorentz force opposes the pinning force, which scales as JV_c. Thus, the

critical depinning current density J_c, at which Lorentz force equals the maximum pinning force is given by,

$$J_c B = \sqrt{\frac{n_p \langle f_p^2 \rangle}{V_c}} \tag{1.16}$$

where f_p is the root mean square force for a single pin on a given flux line. Equation 1.16 is the most important outcome of the L.O theory which connects J_c with the correlation volume V_c. So, any changes in vortex lattice caused by the sudden change in the correlation volume, would attest as a modulation in J_c.

One can estimate the length scales L_c and R_c in terms of the shear (c_{66}) and tilt (c_{44}) moduli by minimizing the free energy which has contributions from the pinning energy and elastic energy [47]. The increase in elastic energy δE_{els} per unit volume due to shear (s_s) and tilt (s_t) fractional distortions (strains) are given by,

$$\delta E_{els} \sim \frac{1}{2}\left[c_{66} s_s^2 + c_{44} s_t^2\right] \tag{1.17}$$

Here, s_s accommodated over a length scale R_c is $\frac{\xi}{R_c}$, and the increase in a line strength for s_t over a length scale L_c is given by $\frac{\xi}{L_c}$. Therefore, δE_{els} becomes,

$$\delta E_{els} = \frac{1}{2}\left[c_{66}\left(\frac{\xi}{R_c}\right)^2 + c_{44}\left(\frac{\xi}{L_c}\right)^2\right] \tag{1.18}$$

The corresponding change in pinning energy δE_{pin} over a length scale [47] is $\frac{\xi f_p n_p^{1/2}}{V_c^{1/2}}$. So, the net energy change δF is,

$$\delta F = \frac{1}{2}\left[c_{66}\left(\frac{\xi}{R_c}\right)^2 + c_{44}\left(\frac{\xi}{L_c}\right)^2\right] - \frac{\xi f_p n_p^{1/2}}{V_c^{1/2}} \tag{1.19}$$

Minimizing the equation with respect to R_c and L_c by recalling $V_c = R_c^2 L_c$, one obtains

$$L_c = \frac{2c_{44}c_{66}\xi^2}{n_p f_p^2}, \quad R_c = \frac{2^{1/2}c_{44}^{1/2}c_{66}^{3/2}\xi^2}{n_p f_p^2}, \quad V_c = \frac{4c_{44}^2 c_{66}^4 \xi^6}{n_p^3 f_p^6} \tag{1.20}$$

Equation 1.20 ascertain the physical explanation that the vortex lattice will be more distorted if there are more and/or stronger pinning sites. Also, the correlation volume is elongated along the field direction since $L_c/R_c = \sqrt{2}(c_{44}/c_{66})^{1/2} >> 1$.

1.6 Bean's critical state model

Isothermal magnetization measurements of a type – II superconductor shows hysteresis. In 1964, C. P. Bean [20] established a relation between hysteretic behavior and J_c. According to Bean's model, the current flowing at any point of the sample can have value J_c or zero.

The pins present inside the superconducting specimen prevents flux distribution to reach its equilibrium value and this makes an irreversibility in the magnetization hysteresis loop. When the applied magnetic field is greater than H_{c1}, the flux lines penetrate into the superconductor to have some gradient in the density of the flux lines. Also, in a static situation, the gradient in the density of the flux lines does not change with time and this satisfies the condition $F_L = -F_p$ everywhere in the superconductor. Such a state is called as critical state. In this state, the superconductor reacts to variations in the applied magnetic field via the shielding currents which is equal to J_c. As the flux lines start to enter the superconductor, they arrange themselves such that the driving force emerging due to the flux density gradient is same as the maximum value of the pinning force. Therefore, the magnetic field profile inside the superconductor can be estimated by the Maxwell equation, $\overrightarrow{\nabla} \times \overrightarrow{B} = \mu_0 J_c$ with appropriate boundary conditions.

For a superconductor crystal of width $2d$ in the x direction and the applied magnetic field H parallel to the superconducting slab (taken as the z direction) then the Maxwell equation

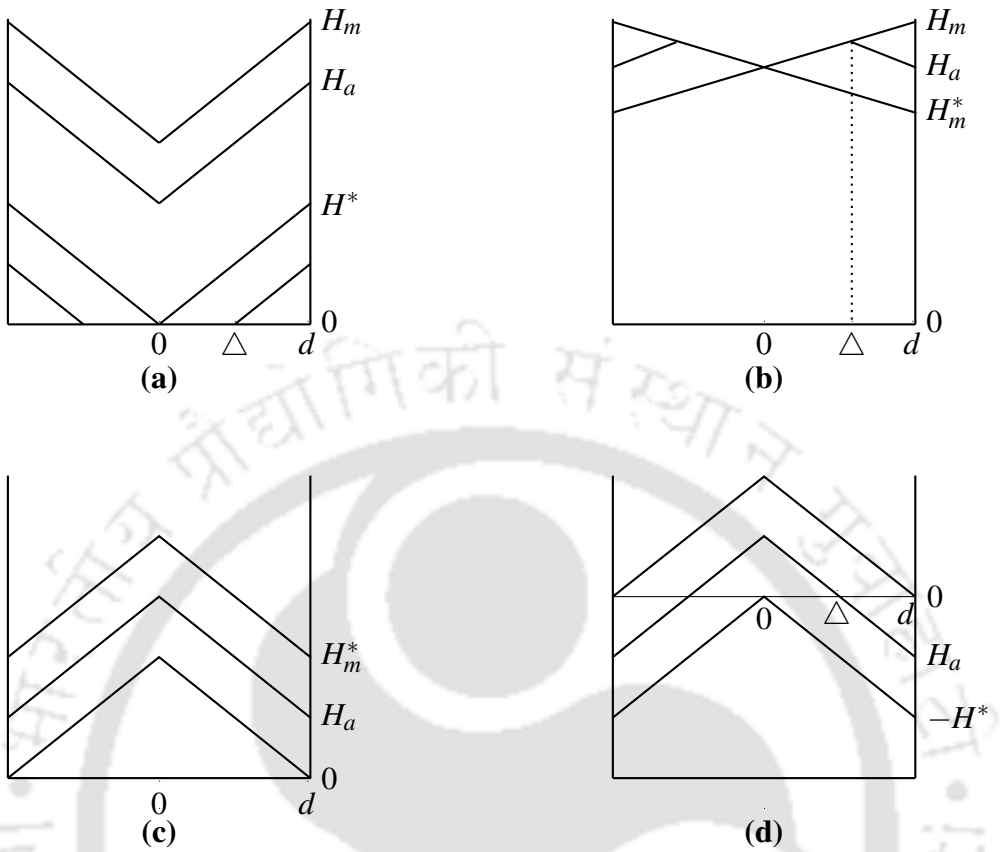

Figure 1.7: *A graphical representation of the magnetic field penetration profiles at various stages of the applied field (H_a) predicted by the critical state model. (a) $0 \leq H_a \leq H_m$ (b) (b) $H_m \geq H_a \geq H_m^*$ (c) $H_m^* \geq H_a \geq 0$ and (d) $0 \geq H_a \geq -H^*$ [Courtesy [48]].*

becomes $\frac{dB}{dx} = \pm\mu_0 J_c$, where the negative and positive signs correspond to the decreasing and increasing field, respectively. Fietz and Webb [70] established a relation between J_c and the magnetization hysteresis with the help of the following convenient relation,

$$J_c(H) = \frac{M_\downarrow(H) - M_\uparrow(H)}{kR} \tag{1.21}$$

where $M_\downarrow$ corresponds to the magnetization in the field decreasing leg of the hysteresis and $M_\uparrow$ are the magnetization corresponds to the field increasing leg of the hysteresis. Also k is a constant which depends on the sample geometry and $2R$ is the dimension of the sample perpendicular to the applied magnetic field direction. Fietz and Webb also showed that the

equilibrium magnetization (M_{eq}) of the superconductor is given by the average magnetization value

$$M_{eq} = \frac{M_{\downarrow}(H) + M_{\uparrow}(H)}{2} \tag{1.22}$$

The field penetration profile and the current distributions caused by this field profiles for different stages of magnetic field evolutions are represented in Fig. 1.7 [48]. The current flows through a layer $\triangle$ is given by $H_a = \triangle/J_c$, where H_a denotes the applied magnetic field. The limiting field at which the current flows through the total volume of the sample is defined as H^*.

1.7 Two anomalies – peak effect and second magnetization peak

The two well documented anomalous features in the J_c of a superconductor are the peak effect (PE) and the second magnetization peak (SMP). The sharp increase in J_c near the H_{c2} boundary of superconductors is identified as peak effect. Fig. 1.8(a) shows the representation of SMP and PE phenomenon in the J_c measurements of a typical low T_c type – II superconductor like $Ca_3Rh_4Sn_{13}$. The PE phenomenon, signals the collapse of the rigidity of the flux line lattice near H_{c2}, leading to a softer flux line lattice binding itself more strongly to the pinning centers and hence leading to the enhancement of the critical current [21]. This could be understood mathematically by considering the shear modulus and pinning force density. The shear modulus c_{66} varies ($cf.$ Fig. 1.8(b)) as $\propto (H - H_{c2})^2$ while the pinning force (F_{pin}) varies as $\propto (H - H_{c2})$. Near H_{c2}, F_{pin} wins over the elastic energy and as a result, a softer lattice can form more readily to the underlying pinning potential, which results in an increase in J_c. Recent experiments [2, 71] provide enough evidences to consider PE as a mark of order to disorder transformation of the underlined vortex lattice.

Also, it has been verified that the peak effect phenomenon causes a first order transition in the vortex systems [2, 25].

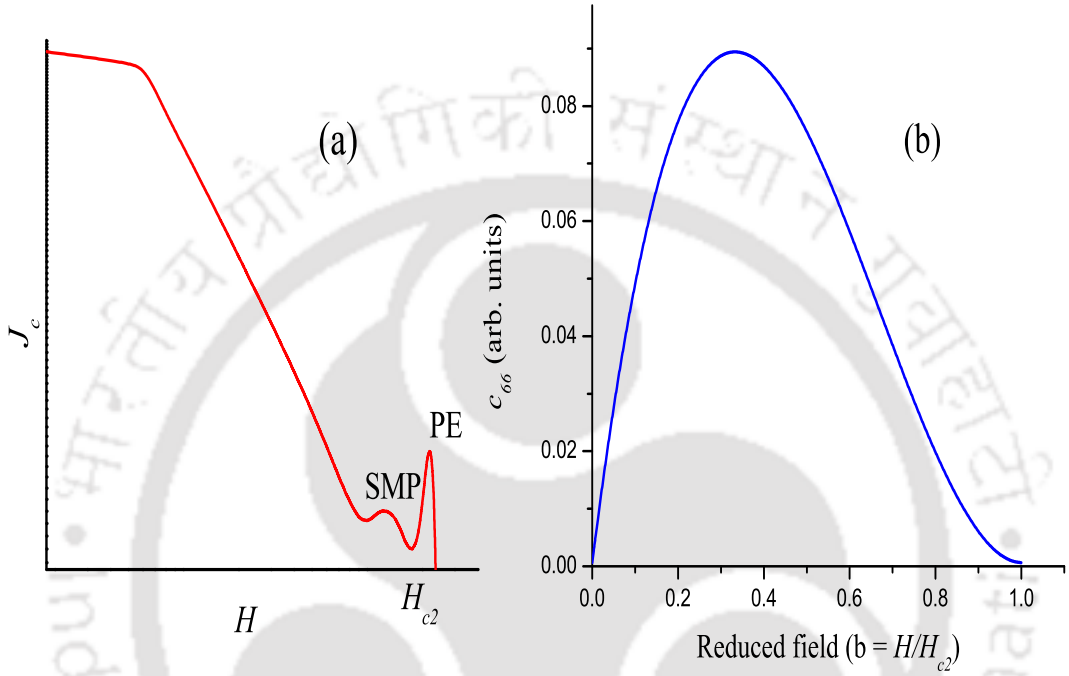

Figure 1.8: *(a) A schematic representation of J_c vs. H measurements where the second magnetization peak (SMP) and the peak effect (PE) are attested as anomalous peaks in J_c. (b) Variation of shear modulus (c_{66}) as a function of reduced magnetic field, b.*

Most of the high T_c superconductors show the SMP anomaly as an increase in J_c at low fields [16, 72]. Compared to the PE anomaly the observed SMP anomaly in the J_c of a low T_c superconductor is less sharp (*cf.* Fig. 1.8(a)). Recent observation of SMP in low T_c superconductors [7, 9, 11] validate the idea that the said behavior is generic to weakly pinned superconductors and not the intrinsic property of only high T_c superconductors. The SMP is now widely accepted as a fingerprint of a transition from a BG phase, i.e., a vortex state without topological dislocations to a multi-domain VG phase, a state with dislocations [26, 73]. The phase diagram of low T_c superconductors usually show temperature indepen-

dent SMP [11] whereas the phase diagram of some of the high T_c superconductors show temperature dependant SMP [16, 74].

1.8 Modified phase diagram of a type – II superconductor

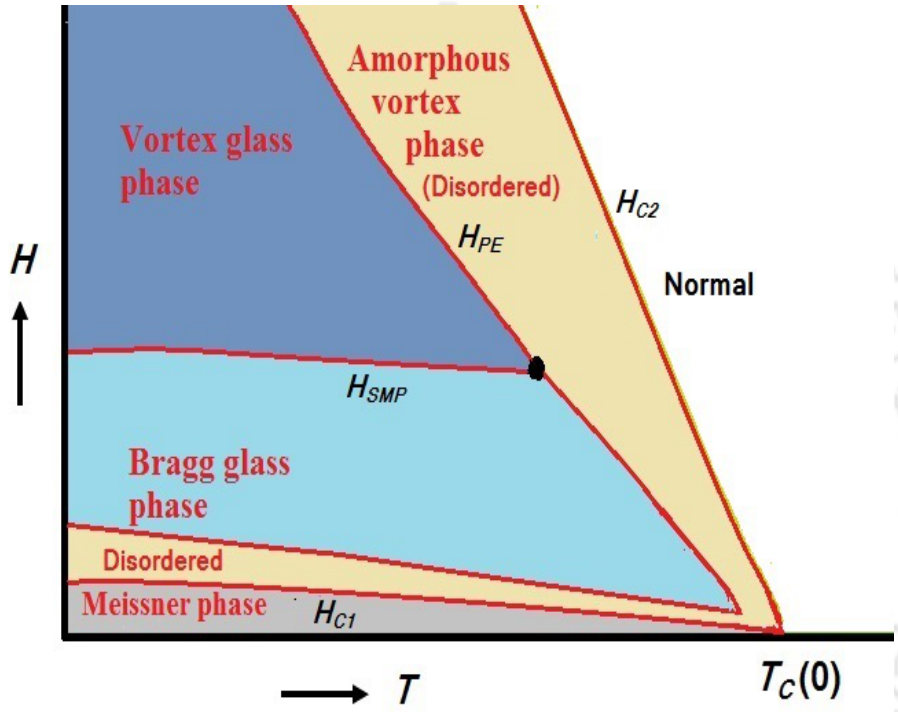

Figure 1.9: *Modified vortex phase diagram of a type – II superconductor beyond the mean field description. After BG phase, VG phase commence from the boundary line, H_{SMP}. The amorphous vortex phase in the phase diagram is due to the PE anomaly and it starts from the H_{PE} boundary onwards.*

The effect of pinning and different types of fluctuations on the vortex system largely modify the mean field phase diagram of a type – II superconductor. Fig. 1.9 shows the (*H*-*T*) phase diagram of a type – II superconductor which contains SMP and PE anomalies. After the Meissner phase, there may exist a re-entrant disordered phase of first order nature due to the changes in the elastic constants. After this re-entrant disordered phase, the ordered Bragg glass phase attest its presence in the phase diagram. The BG phase is anticipated

in a large portion of the (*H,T*) phase diagram of any realistic superconducting sample. In type – II superconductors, the SMP anomaly indicates the formation of the disordered VG phase just after the BG phase. In most of the superconductors, the boundary of the BG and VG phases are shared with the amorphous vortex phase which arises at the commencement of the PE anomaly [32, 75, 76]. The superconductor becomes normal in the H_{c2} phase boundary.

1.9 Surface superconductivity and paramagnetic Meissner effect

An infinite superconductor sample becomes normal when the applied magnetic field H is larger than $H_{c2} = \kappa\sqrt{2}H_c$ where H_c is the thermodynamic critical field. Contrariwise, when the field H is reduced, superconducting regions appear spontaneously at $H = H_{c2}$. This conclusion was obtained for an infinite sample, i.e., by neglecting the surface effects [77]. In some of the superconducting materials, the superconducting properties exist above the bulk critical field H_{c2} up to another critical field H_{c3} due to the nucleation of the superconductivity on the surface of the material. Saint-James and de Gennes [78] first established a theoretical explanation for the large amount of experimental data on the persistent nature of this superconductivity at high fields, which was previously misunderstood and thought to be occurring due to the inhomogeneous nature of the sample. They proved that superconductivity can nucleate at a metal-insulator interface in parallel field H_{c3} higher by a factor of 1.695 than H_{c2}. There is a superconducting sheath of thickness $\sim \xi(T)$ (while $\psi \to 0$ in the sample interior) forming for field values between H_{c2} and H_{c3} [47]. Surface superconductivity was reported in several low T_c superconductors like Nb, In+Sn, Pb+Bi etc [77].

A superconducting specimen, kept in an external magnetic field, H and cooled down through T_c expels the magnetic flux and this phenomenon is known as diamagnetic Meiss-

ner effect (DME). But surprisingly, some of the superconducting samples show a paramagnetic modulation below T_c, which corresponds to the paramagnetic Meissner effect (PME) or Wohlleben effect. PME was first reported in high T_c superconducting ceramic samples and this prompted the birth of a number of theories, relating this phenomena to unconventional superconductivity [79–81]. Some studies predicted that the existence of spontaneous Josephson currents, created at π-junctions across some grain boundaries in the superconducting specimen make the PME. Such an explanation hold for high T_c superconductors; however, the later discovery of PME signals in the low T_c superconductors like Nb [3, 39, 82] and twinned single crystals of $YBa_2Cu_3O_{7-\delta}$ [41] indicated that reasons other than the π-junctions and unconventional superconductivity can also be the source of PME. A probable origin of the PME is flux compression caused by an inhomogeneous superconducting transition [83, 84]. The trapped vortices which may lead to the PME anomaly is expected as a result of the surface inhomogeneities or inhomogeneous cooling of the superconducting specimen.

1.10 Metastability of vortices in the magnetization measurements

Metastable states are common in physical systems of many interacting particles. It is very difficult to construct an equilibrium phase diagram of a metastable system because metastability usually mislead the exact local minima. Vortices in type – II superconductors provide a finest example of metastable systems. Some of the phenomena manifesting the vortex state metastability in type – II superconductors are the history dependence in critical current density, history dependent dynamic response, long term memory, hysteretic transport characteristics, and negative dynamic creep [85, 86]. Theoretical calculations of Giamarchi and Le-Doussal [26] have revealed the existence of Bragg glass phase of the vortex system with

many metastable states. Usually, metastability exists till the spinodal line, where a spinodal line determines the limit of the fluctuations in a (H-T) phase diagram of thermodynamic equilibrium. The observation of supercooling/superheating of the vortex system from the magnetization data indicates the underlying metastability of the superconducting systems [2, 86, 87].

The metastable vortex states of a superconductor could be very fragile with the presence of very weak pinning. Any effort to make contact with the metastable system to the outside world disturbs the original vortex system such that it is altered into a different vortex state, by losing the primal information relating to metastability [88]. Therefore, it is possible to change the metastable vortex state to the ground state by applying small perturbations to the system. Magnetization studies in one of the 2H-$NbSe_2$ single crystal show the possibility to convert a metastable FC state to an ordered ZFC state by controllably applying an oscillating magnetic field. Further studies proved that the metastable FC states can be revert back by applying a heat pulse in the ZFC state [89]. Ling et al. [2] directly demonstrated the metastable supercooled/superheated vortex matter by the introduction of a weak perturbation and after observing the evolution of the SANS patterns in Nb single crystal in the ZFC and FC magnetization studies. In their experiment, they observed that above the peak of the PE, the ordered ZFC state becomes disordered when a small perturbation was applied in the form an ac magnetic field. This imbibe the fact that above the peak of the PE, the ordered vortex lattice from the ZFC mode is a metastable superheated state. Hence, the ground state of the vortex matter belongs to a disordered state. Also, after applying the ac field below the peak of the PE, the metastable disordered FC states become an ordered ground state. This suggest the fact that the disordered FC state below the peak of the PE is a supercooled disordered vortex state and applying a small perturbation drive the state into an ordered ground state of the vortex lattice [2].

It is observed in 2H-$NbSe_2$ single crystal that the disordered vortex lattice can be easily supercooled below PE by field cooling, where it rests in a metastable state if the thermal fluctuations are minimal [90]. In 2H-$NbSe_2$, a significantly larger critical current density is observed due the presence of these more strongly pinned supercooled disordered phase. Vortices can be found in various metastable states near to the order-disorder transitions. Each metastable configuration can attest different value of critical current density which is determined from the specific magnetic history [91]. Minor magnetization loop measurements in a single crystal of V_3Si reveal the J_c history dependence of magnetic fields of small value to maxima of the PE [91]. This history effects indicates the supercooling and superheating of the vortex matter when the field is cycled across the transitions. Different metastable configurations of the vortex matter generated due to different magnetization histories can be pushed to stable configuration by using repeated magnetic field cycling procedure [92].

Most of the magnetization studies show that the inevitable pinning centers present in the superconducting samples lead to the existence of metastability. Increasing the pinning increases the metastability effects in the vortex matter. The ac susceptibility studies in 2H-$NbSe_2$ single crystals having different pinning strengths show the metastable SMP regions [6]. The metastability of the SMP is further confirmed by the field scan rate dependence studies where different scan rates make different metastable J_c curves which include the SMP anomaly [33].

Recent SANS experiments by Rastovski *et. al.*[34], in a single crystal of MgB_2 resulted in well ordered vortex lattice with metastability. This point out the fact that vortex pinning is not the main reason for the metastability in vortex lattice configuration. They have shown that the vortex density of the observed metastable states increase with increase of H. But, a vortex lattice pinned with defects must have a constant vortex density, irrespective of the changes in the magnetic field. They put forward the idea that the metastability arise "due to the jamming of counter rotated vortex lattice domains which prevents a rotation

to the ground state orientation." Most of the cases, metastability effects attest its signature upto the superconducting – normal transition boundary. Theoretical model by Zharkov [42] predicts that various metastable states with positive and negative signs of magnetization can be possible in the PME region. The internal transitions between vortex states of different vorticities (m-states) is also predicted with this model.

1.11 Perspective

A number of phenomena exhibited by the vortex matter pose challenges to researchers in their precise comprehension. Nowadays, SMP and PE gained enough momentum in vortex matter research due to its anomalous behavior in different superconducting samples. The temperature independent nature of the SMP line has been reported several times both in high T_c superconductors as well as in low T_c cubic superconductors [11, 14, 29]. The pinning strength variation in high T_c superconductor, BSCCO makes temperature dependent SMP line and a notion of 'inverse melting' over a limited range of (H,T) values [16, 30]. However, the observation of temperature dependent SMP line in low T_c superconductors is still lacking. Our first attempt is to address this issue with the help of newly prepared $Ca_3Rh_4Sn_{13}$ single crystals which show both SMP and PE anomalies in their magnetization data. These crystals have the Ginzburg number, 10^{-5} which is very less in comparison with the high T_c superconductors. The pinning strength of $Ca_3Rh_4Sn_{13}$ single crystal, $j_c/j_o = 10^{-4}$ (where j_c and j_o are the depinning and depairing current densities, respectively) shows an intermediate value between high T_c superconductors like BSCCO (10^{-1}) and low T_c superconductors like $NbSe_2$ (10^{-6}). We have also made attempts to understand the spectral fluctuations of noise in magnetization data across the SMP and PE anomalous region.

The metastable nature of the vortex matter creates interesting effects in the vortex phase diagram [2, 85, 89, 93]. The effect of metastability in the critical current density of the materials has been reported in the transport measurements [35, 36, 86]. Different vortex

lattice structures, which may be metastable, leave an imprint as two depinning currents in transport measurements [35]. Recent small angle neutron scattering (SANS) measurements have reported the occurrence of a pinning independent metastable state with a slightly different vortex lattice structure from that of the original structure [34]. Hence, it is interesting to check whether the metastability effects in the critical current density is a generic characteristics of the vortex lattice. So, in this thesis we employ sweep field mode and stable field mode magnetization measurements to explore the possibilities of finding two critical current densities.

Numerous reports about paramagnetic Meissner effect (PME) (a positive magnetization signal in the superconducting region) in both bulk and nano superconductors while field cooling the sample have raised considerable interest [3, 37–41]. In this thesis we search such positive magnetization regions and its characteristics below the transition temperature of the $Ca_3Rh_4Sn_{13}$ single crystal.

Chapter 2

Techniques and Methods

2.1 Sample preparation and characterization

In this thesis we have explored different vortex phases in details in single crystals of cubic $Ca_3Rh_4Sn_{13}$ with the help of magnetization measurements. The $Ca_3Rh_4Sn_{13}$ single crystals were grown by flux growth method [43, 44]. This simple method, which involves dissolving Calcium and Rhodium metals in an excess amount of tin proves to be successful in producing large clean single crystals of $Ca_3Rh_4Sn_{13}$. All component materials were obtained from Aldrich Ltd. of high purity. The starting materials were finely powdered and well mixed using an agate pestle and mortar. The powder mix was then place into a silica tube, which was then evacuated and sealed. The silica tube was held upright in a furnace and the melt was soaked at 1050 ^{o}C for 2 hours. Afterwards the melt was slowly cooled by 6 ^{o}C/hr down to 575 ^{o}C and after we removed the silica tube from the furnace and cool rapidly to the room temperature. This rapid cooling helps to get clean crystal surfaces (If we employ slow cooling for solidification, then the crystal surfaces may spoil due to precipitates [43]). For removing the excess flux from the crystal, the solid melt was immersed in concentrated hydrochloric acid. The crystals were removed from the acid as soon as they broke away from the excess flux to prevent destruction to the crystal surfaces.

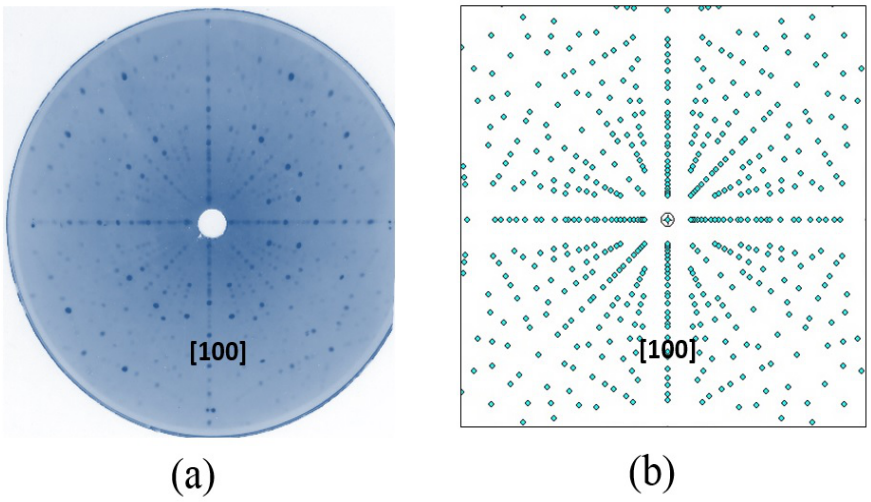

Figure 2.1: *X-ray Laue diffraction pattern of the single crystal of $Ca_3Rh_4Sn_{13}$ obtained with the incident X-ray beam parallel to the crystallographic [100] axis. (b) Simulated Laue diffraction pattern of the $Ca_3Rh_4Sn_{13}$ crystal in the crystallographic [100] axis .*

Single crystals were inspected by means of X-ray back scattering in standard Laue geometry. The crystal is mounted on the goniometer (which can be rotated along all three axes) such that X-ray beam falls on the plane that one want to expose. Radiation from anode was used as an incident beam and beam reflected from the sample was recorded on a photographic film [94]. The Laue diffraction pattern from the crystal is observed on a photographic film as a regular array of spots. This Laue spots provide information about the orientation of the single crystal. The difference between this method and the powder diffraction method is that the angle is kept constant here and the wavelength is effectively varied due to the polychromatic nature of the source. The pattern obtained on the film helps to orient the crystal according to the plane required. A typical Laue pattern obtained from the $Ca_3Rh_4Sn_{13}$ single crystal used in the magnetization measurements can be seen in Fig. 2.1(a). Fig. 2.1(b) shows the corresponding simulated Laue diffraction pattern with X-ray beam parallel to the crystallographic [100] axis. Published values for the lattice parameters [43] were used to generate the pattern with the help of the open source software package OrientExpress. Measurement of the lattice parameters, using the positions of the strongest

reflections on the film, are in good agreement with published values [43]. After proper orientation with the help of Laue diffraction, samples with desired shape and dimensions were cut by means of spark-erosion technique. More details of the studied single crystals are included in Appendix A.

2.2 DC magnetization measurements

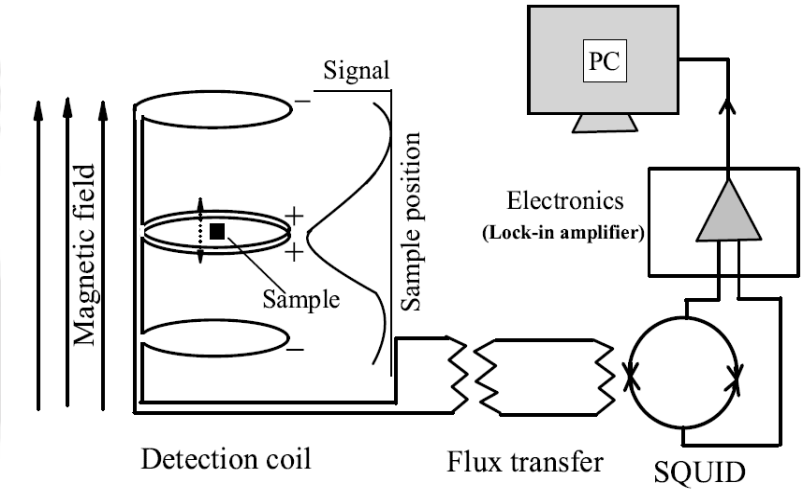

Figure 2.2: *Schematic of the SQUID-VSM detection system.*

The dc magnetization measurements give information about the critical current density, $J_c(H)$. For the portion of the irreversible magnetization hysteresis loop, the width of the hysteresis loop gives an estimate of J_c ($\propto \triangle M$) [20, 70]. For the experimental observation of the magnetization of the superconductor, one can use the vibrating sample magnetometer (VSM) or superconducting quantum interference device - vibrating sample magnetometer (SQUID-VSM).

The vibrating sample magnetometer invented in 1955 by Simon Foner at Lincoln Laboratory MIT, measures the rate of change of magnetic flux by the mechanical vibration of a magnetized sample, which produces an emf in a detection coil system. The sample is

vibrated in a homogenous magnetic field with some fixed frequency and amplitude. The time-dependant induced voltage in the VSM coils is given by the equation:

$$V_{coil} = \frac{d\phi}{dt} = \frac{d\phi}{dz}\frac{dz}{dt} \tag{2.1}$$

where ϕ represents the magnetic flux enclosed by the coil, z represents the vertical position of the sample with respect to the coil and t is the time. The voltage of the sinusoidal oscillating sample is given by

$$V_{coil} = 2\pi f C m A sin(2\pi f t) \tag{2.2}$$

where C is the coupling constant, m represents the magnetic moment of the sample, A and f are the amplitude and frequency of the oscillation respectively. So the magnetization of the sample is calculated by measurement of the coefficient of the sinusoidal voltage responses from the coil.

The SQUID-VSM is a combination of the conventional high speed VSM and the high sensitive SQUID. Magnetic flux in SQUID-VSM is detected by SQUID sensors. SQUID-VSM is one of the most sensitive and effective instrument to determine the magnetic moment/field in less time compared to the usual SQUID magnetometer. Signal created by sample vibration is frequency modulated to separate the sample signal from the instrumental artifacts. Fig. 2.2 illustrates the simplified block diagram of the SQUID-VSM detection hardware. The current in the detection coil is a function of the sample position. In magnetic property measurement system (MPMS) SQUID-VSM, the superconducting detection coils are configured as a second order gradiometer, with counterwound outer loops which makes the set of coils non-responsive to uniform magnetic fields and linear magnetic gradients. The sensor in the MPMS SQUID-VSM is a Josephson junction - which is a device consisting of superconducting -insulating-superconducting tri-layer junction. The MPMS SQUID-VSM

detects the change in currents or frequency to deduce the magnetic moment of the sample. The MPMS SQUID-VSM is capable of providing magnetic fields in the range ±70 kOe with field ramp possible as high as 700 Oe/s and sample temperature ranging from 1.7 K to 400 K. Sensitivity is 1×10^{-8} emu at earths field and 5×10^{-8} emu at 70 kOe.

2.3 AC susceptibility measurements

The ac susceptibility measurements probe the screening response due to the shielding current of the superconductor. The ac magnetization measurements are done with an applied dc field (H) and an ac field $h_{ac} = h_0 cos(\omega t)$ of frequency ω and amplitude h_0. The expressions for the in-phase part of the ac susceptibility (χ') and the out of phase part of the ac susceptibility (χ'') deducted from the nonlinear response of the critical state model are as follows [95].

$$\chi' \sim 1 + \frac{\alpha h_{ac}}{J_c}, \quad \text{for} \quad h_{ac} < H^* \tag{2.3}$$

$$\chi'' \sim \frac{\alpha' h_{ac}}{J_c}, \quad \text{for} \quad h_{ac} < H^* \tag{2.4}$$

$$\chi' \sim -\beta \frac{J_c}{h_{ac}}, \quad \text{for} \quad h_{ac} > H^* \tag{2.5}$$

$$\chi'' \sim \beta' \frac{J_c}{h_{ac}} - \gamma \frac{J_c^2}{h_{ac}^2}, \quad \text{for} \quad h_{ac} > H^* \tag{2.6}$$

where α, α', β, β' and γ are geometry dependant factors and H^* represents the field at which the induced screening currents flow through the whole sample. With the help of equations 2.3 and 2.5, one can relates the in-phase part of the ac susceptibility (χ') to the critical current density, J_c. So, changes in (χ') can be interpreted as changes in J_c, which

in turn will be related to determine the changes in correlation volume (V_c). So, the ac susceptibility measurements may also provide the information about the underlying vortex lattice. For the ac susceptibility measurements, we have used the AC susceptibility option of the MPMS SQUID VSM (Quantum Design Inc. USA). This AC susceptibility option have AC frequency range 0.1 Hz to 1 kHz and AC amplitude range 0.1 Oe to 10 Oe with an AC moment sensitivity $\leq 5\times10^{-8}$ emu.

Chapter 3

Vortex phase diagram of $Ca_3Rh_4Sn_{13}$ single crystal

3.1 Introduction

The competition between the elastic energy, the pinning energy and the thermal energy dictates the various characteristics of the existence/coexistence of different possible phases in the vortex matter. As the second magnetization peak (SMP) which is signaling the dominance of pinning over elastic energy lies deep inside the mixed phase, thermal fluctuations expected to play a small role in determining the phase transition imprinted by this anomaly. Evidences mounted over the years [11, 14, 29] that the SMP line in the vortex phase diagram is temperature independent both in high T_c superconductors, like $Bi_2Sr_2CaCu_2O_8$ (BSCCO), $YBa_2Cu_3O_{7-\delta}$ (YBCO) etc., as well as in low T_c cubic superconductors, like $Ca_3Rh_4Sn_{13}$, etc; a small positive slope in the thermal variation of the SMP line is accepted as self-explanatory [16, 22].

As the temperature enhances even deep inside the mixed phase, it could decrease the effective pinning energy, leading to a slight shift of the onset field of SMP towards a higher value. In high T_c, BSCCO, where intrinsic pinning strength varies with oxygen concen-

tration (hole doping/vacancies), the usual temperature independent onset field of SMP was reported to increase/decrease with enhancement in temperature over a limited range of (*H,T*) values in few crystals [16]. The overlap of SMP line having positive slope ($dH^{on}_{SMP}/dT > 0$) with the thermal melting line at higher (*H,T*) values led to the proposition of concept of 'inverse melting' concurrent with usual melting, wherein BG phase transformed to vortex liquid/vortex glass state on increasing/decreasing the temperature in a portion of the (*H-T*) phase space [30]. The elucidation of the notion of 'inverse melting' was also claimed in few crystals of YBCO [74, 96], wherein a SMP phase boundary with positive slope eventually merged with the PE line, making the collapse of elasticity of the vortex solid. An entropic change across FLL melting transition in BSCCO was measured conclusively and the first order nature of amorphization of vortex matter across PE lines had received support from the existence of superheated/supercooled metastable states in a crystal of Nb, an example of low T_c superconductors [2, 30]. However, conclusive evidence for the matter of BG/VG transition across onset field of SMP anomaly has remained elusive.

In the background of the above stated facts, it is not irrational to anticipate the exemplification of the generic nature of the notion of inverse melting in a specific portion of the (*H-T*) phase space in those samples of conventional superconductors which imbibe positive slope of SMP phase boundary. Keeping this in view, we explored the details of vortex phase diagram in different single crystals of cubic $Ca_3Rh_4Sn_{13}$. In this chapter we present the magnetization (dc as well as ac) studies in one of these crystals, which has slightly higher pinning than that in the earlier studied crystal by Sarkar *et. al* [11]. The new results indeed validate the characteristics of inverse melting in an isotopic low T_c superconductor, analogous to that reported in the anisotropic high T_c superconductor YBCO [74] for $H||c$, thereby establishing the generic credential of this notion for the vortex matter. The ac susceptibility measurements demonstrate the spinodal line in this crystal, which endorses the first order nature of phase transition across SMP in this low T_c superconductor. We have also made at-

tempts to understand the spectral fluctuations in noise in magnetization data of $Ca_3Rh_4Sn_{13}$ single crystal across the SMP and PE anomalous region. The observation of $1/f$ noise deep inside the mixed phase of this superconductor is also discussed in this chapter.

3.2 Experimental

The $Ca_3Rh_4Sn_{13}$ single crystal ($2.8 \times 1.6 \times 1$ mm^3, 32.22 mg) was prepared using flux growth technique. The dc magnetization measurements were carried out using a commercial SQUID-vibrating sample magnetometer (Quantum Design (QD) Inc., USA, model S-VSM) and the ac susceptibility measurements were carried out using a SQUID magnetometer (Q.D. Inc., USA, Model MPMS). The ac measurements were performed with a frequency of 211 Hz. The applied dc field (coaxial with the ac field) was kept parallel to the [100] axis of the cubic crystal. The dc magnetization measurements revealed the superconducting transition temperature (T_c) as 8.37 K ($\triangle T_c/T_c \approx 0.05$, where $\triangle T_c$ is the transition width).

3.3 Observation of SMP and PE in $Ca_3Rh_4Sn_{13}$ single crystal via dc magnetization measurements

Inset of Fig. 3.1 shows the five quadrant *M-H* loop of $Ca_3Rh_4Sn_{13}$ at 2 K where the two bubbles in the *M-H* curves identified as SMP and PE. Main panel of Fig. 3.1 shows the right half portion of the *M-H* at 2 K, which unambiguously demonstrates the occurrence of the SMP and PE. The two effects fingerprint as two maxima, the lower field one being the SMP and the upper field one being the PE. The sharpness of the two peaks point out the rapid increase in the J_c at SMP and PE. The onset fields of SMP and PE anomalies stand marked as H^{on}_{SMP} and H^{on}_{PE} and the peak positions of SMP and PE are identified as H^{p}_{SMP} and H^{p}_{PE},

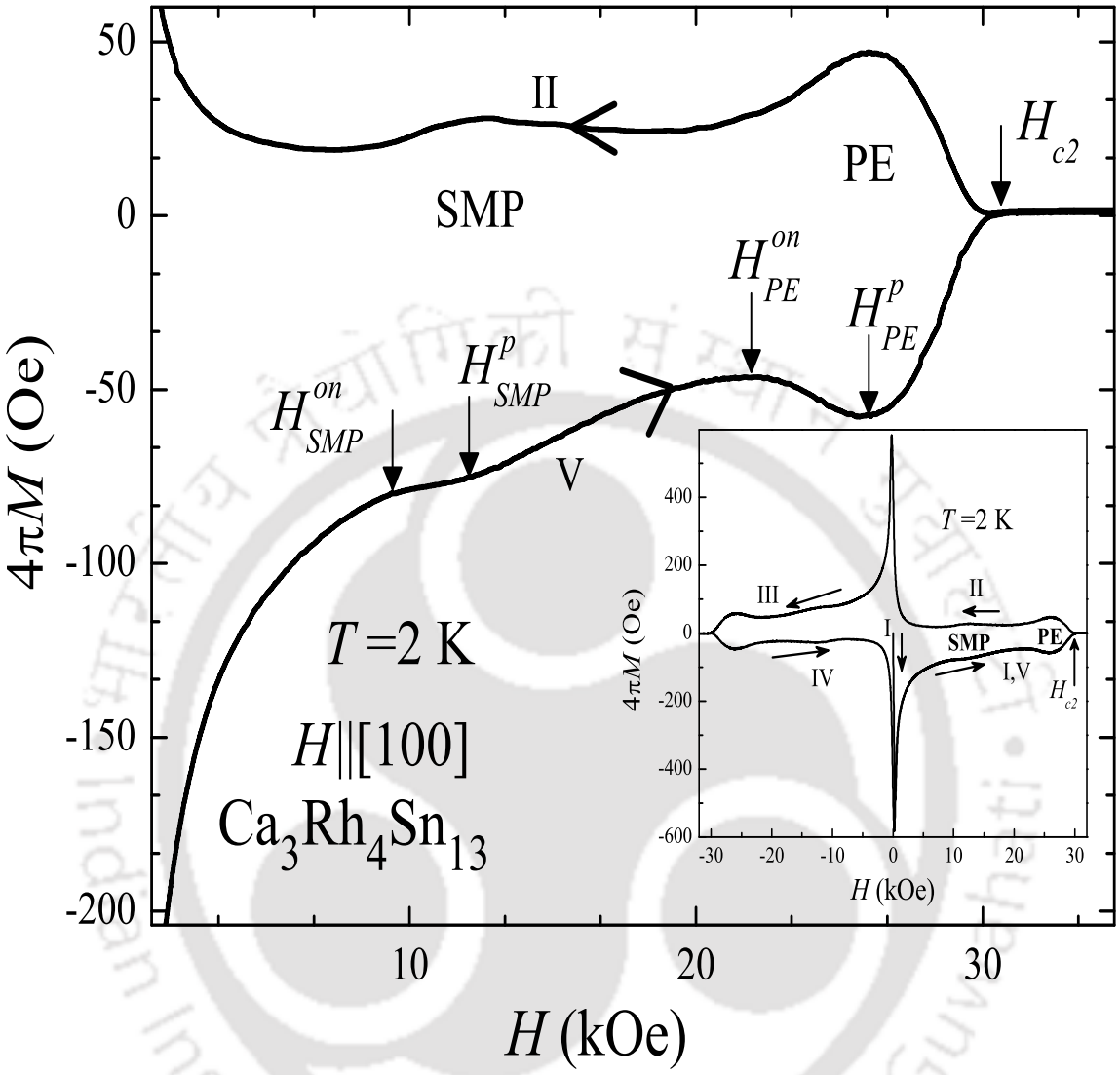

Figure 3.1: *Main panel shows the right half portion of the M-H loop without the virgin (I) curve in a $Ca_3Rh_4Sn_{13}$ single crystal. The sharp modulation near H_{c2} is identified as PE and the modulation in the lower field side is identified as SMP. Complete five quadrant M-H loop at 2 K is shown in the inset.*

respectively. Above H^p_{PE}, the magnetization falls rapidly as the applied field ramps across the upper critical field, H_{c2}.

On examining the *M-H* data from 2 K to 6.5 K (Fig. 3.2) we noticed that the SMP and PE varies with temperature. From Fig. 3.2, the distinction between the SMP and PE can be clearly observed only below the temperature, 4.5 K (Fig. 3.2 (c)). At 5 K, the SMP anomaly

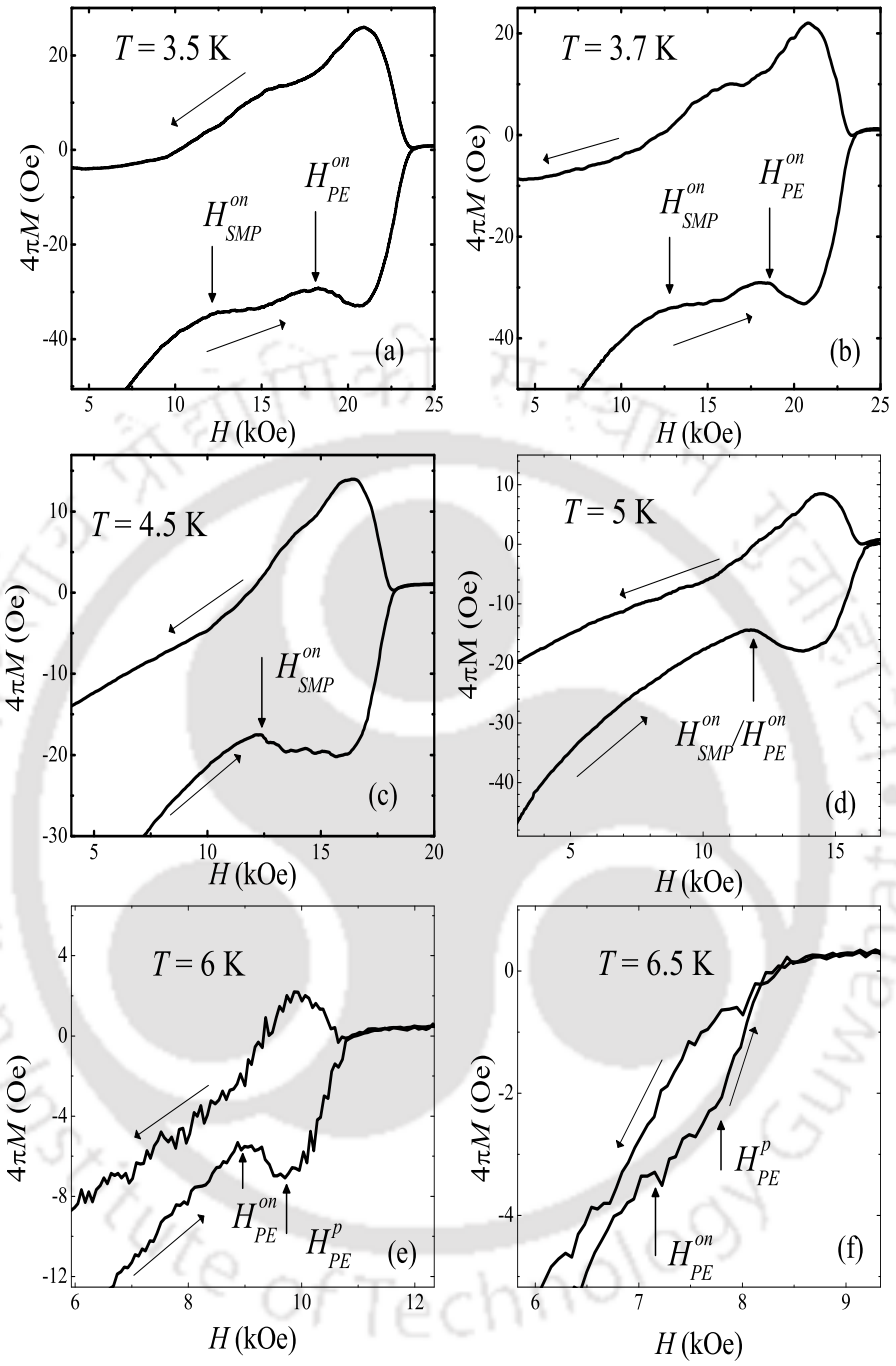

Figure 3.2: *Portions of the M-H loops at constant temperatures (a) 3.5 K, (b) 3.7 K, (c) 4.5 K , (d) 5 K, (e) 6 K and (f) 6.5 K which focus on the temperature dependance of the two anomalies – SMP and PE. Note that at 4.5 K the anomalies SMP and PE start to merge. At 5 K it is impossible to distinguish the onset of SMP and PE.*

juxtaposes with the PE and one can mark only the onset position of the coalesced SMP and PE anomaly (Fig. 3.2 (d)). Above 5 K , only PE anomaly is observed (*cf.* Fig.s 3.2 (e) and (f)). The asymmetric nature of the SMP and PE peaks are clearly observed from the forward and reverse legs of the *M-H* curves.

3.3.1 Observation of SMP and PE from J_c

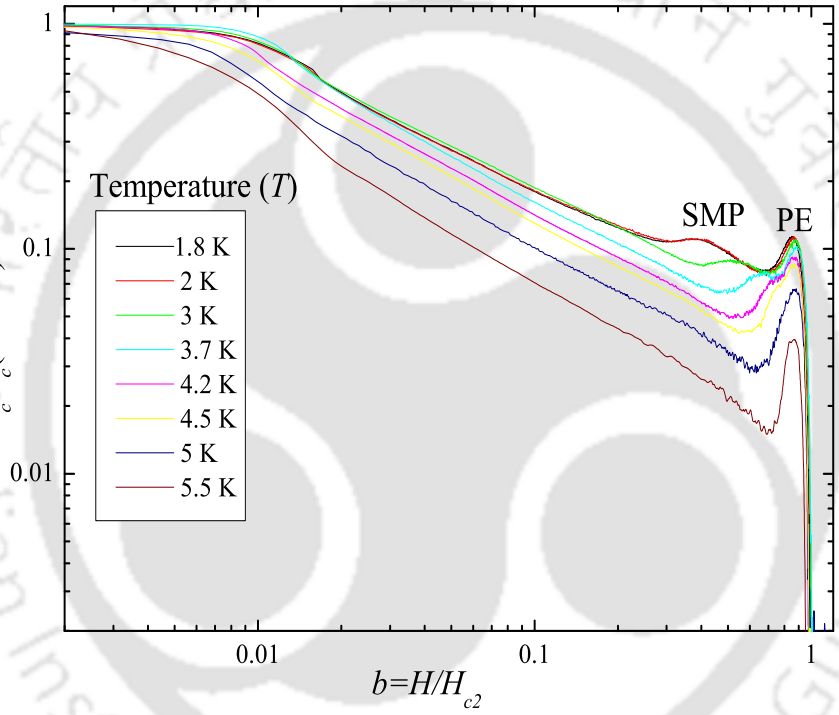

Figure 3.3: *Log-log plots of normalized J_c/J_c(10 Oe) vs. b for $Ca_3Rh_4Sn_{13}$ at different temperatures from 1.8 K to 5.5 K, where $b=H/H_{c2}$ is the reduced magnetic field.*

Fig. 3.3 shows the J_c/J_c(10 Oe) vs. reduced magnetic field b, for temperatures ranging from 1.8 K to 5.5 K. Upto 4.5 K, two modulations correspond to the SMP and PE are observed in J_c. After 4.5 K only one modulation which corresponds to the PE anomaly is observed in J_c. Fig. 3.3 shows the monotonic decrease of PE anomaly with increase of temperature. However, with increase of temperature, the onset field points of SMP anomaly increases upto 3.7 K and after 3.7 K it decreases. For getting a clear idea of the observed non-

monotonic variation of the SMP anomaly, we have plotted the variation of J_c as a function of field in and around 3.7 K (Fig .3.4).

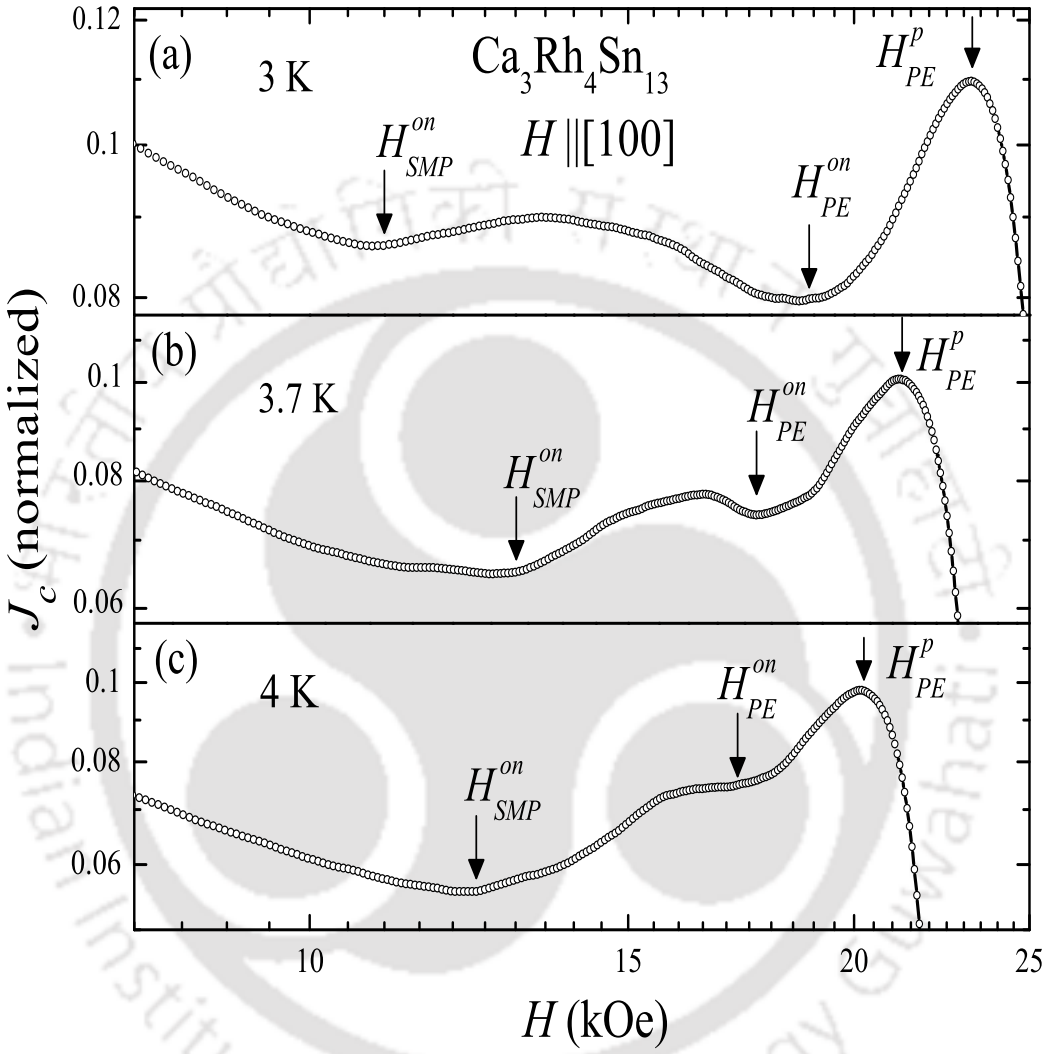

Figure 3.4: Log-log plot of normalized J_c [$\propto \triangle M(H)/\triangle M(50\ \text{Oe})$] vs. H at (a) 3 K, (b) 3.7 K and (c) 4 K. The onset positions of the SMP and PE stand marked by arrows.

Fig.s 3.4(a) to 3.4(c) portray the log-log plot of J_c(normalized) [$\propto \triangle M(H)/\triangle M(50\ \text{Oe})$] as a function of applied field at 3 K, 3.7 K and 4 K, respectively. It reveal that the onset field of the SMP, H^{on}_{SMP}, increases from 10.9 kOe to 13.0 kOe as the temperature enhances from 3 K to 3.7 K (*cf.* 3.4(a) and 3.4(b)). Further with the increase of temperature from 3.7 K to 4 K, the value of H^{on}_{SMP} decreases from 13.0 kOe to 12.3 kOe, (*cf.* 3.4(b) and 3.4(c))

thus exemplifying the non-monotonicity in the temperature variation of SMP. The peak field of SMP also follows the characteristic behavior of H^{on}_{SMP}. However both the onset (H^{on}_{PE}) and peak (H^{p}_{PE}) fields of the PE monotonically decrease with the increase of temperature (*cf.* 3.4(a) to 3.4(c)), as anticipated.

3.3.2 Identification of different vortex phases from J_c

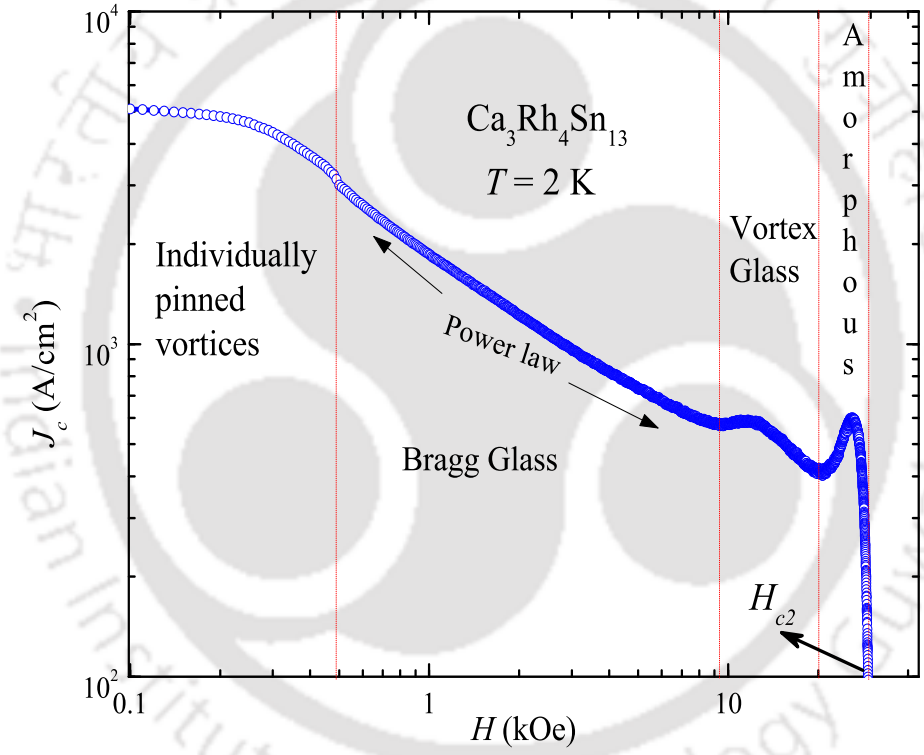

Figure 3.5: *Log-log plot of the critical current density, J_c vs. H at 2 K in $Ca_3Rh_4Sn_{13}$ single crystal. The J_c curve has been divided into four vortex regions with the help of dotted (red) lines.*

As described in section 1.5.2, the equation of Larkin-Ovchinnikov [19, 69] relates the correlation volume, V_c of the vortex domain to the critical current density, J_c. So, changes in J_c indicate the changes in the associated vortex phase. Fig. 3.5 shows the calculated log-log plot of J_c vs. H at 2 K of the $Ca_3Rh_4Sn_{13}$ single crystal. Based on the behavior, we have

divided the J_c curve into four different regions and designated as individually pinned vortex regime, Bragg glass regime (power law regime), vortex glass region and amorphous region.

The first region shows almost a flat variation of J_c with increasing magnetic field, H. This kind of behavior is expected for individually pinned vortices in the weak limit where the intervortex spacing a_0 is greater than or equal to the penetration depth, λ where λ predicts the range of interaction between the vortices. The Bragg glass region, which is identified with the power law is a collectively pinned region. In this region, vortices behave as an elastic medium and quasi-long range transitional order survives. A cross over from an individually pinned to a collectively pinned regime is to be predicted at a threshold field H_t, above which J_c follows the power law behavior. An order of magnitude estimate for H_t can be made in terms of the ratio of depinning (J_c) by depairing (J_0) current densities and H_{c2} using the relation $H_t \sim 5[J_c/J_0]H_{c2}$ [18, 19, 97]. For $Ca_3Rh_4Sn_{13}$ single crystal, we get $H_t \sim 10^{-2}$ Tesla, where $J_c/J_0 \sim 10^{-4}$ and $H_{c2} \sim 3.8$ Tesla. The quasi long range transitional order of the vortex lattice vanishes at the onset of the SMP anomaly. As mentioned earlier, SMP region contains vortex lattices with dislocations and this region is identified as vortex glass region. The amount of disorder is maximum at the peak of the SMP and after the peak, the disorder of the vortex lattice heals upto the onset of the PE. In the PE region, amorphization of the vortices starts and once again J_c increases.

3.4 Observation of SMP and PE in $Ca_3Rh_4Sn_{13}$ single crystal via ac susceptibility measurements

Within the Bean's critical state model prescription J_c has been shown to relate to the in-phase ac susceptibility [95] χ', as $\chi' \sim$ -1+$\alpha h_{ac}/J_c$, where α is a geometry dependent factor and h_{ac} is the ac amplitude.

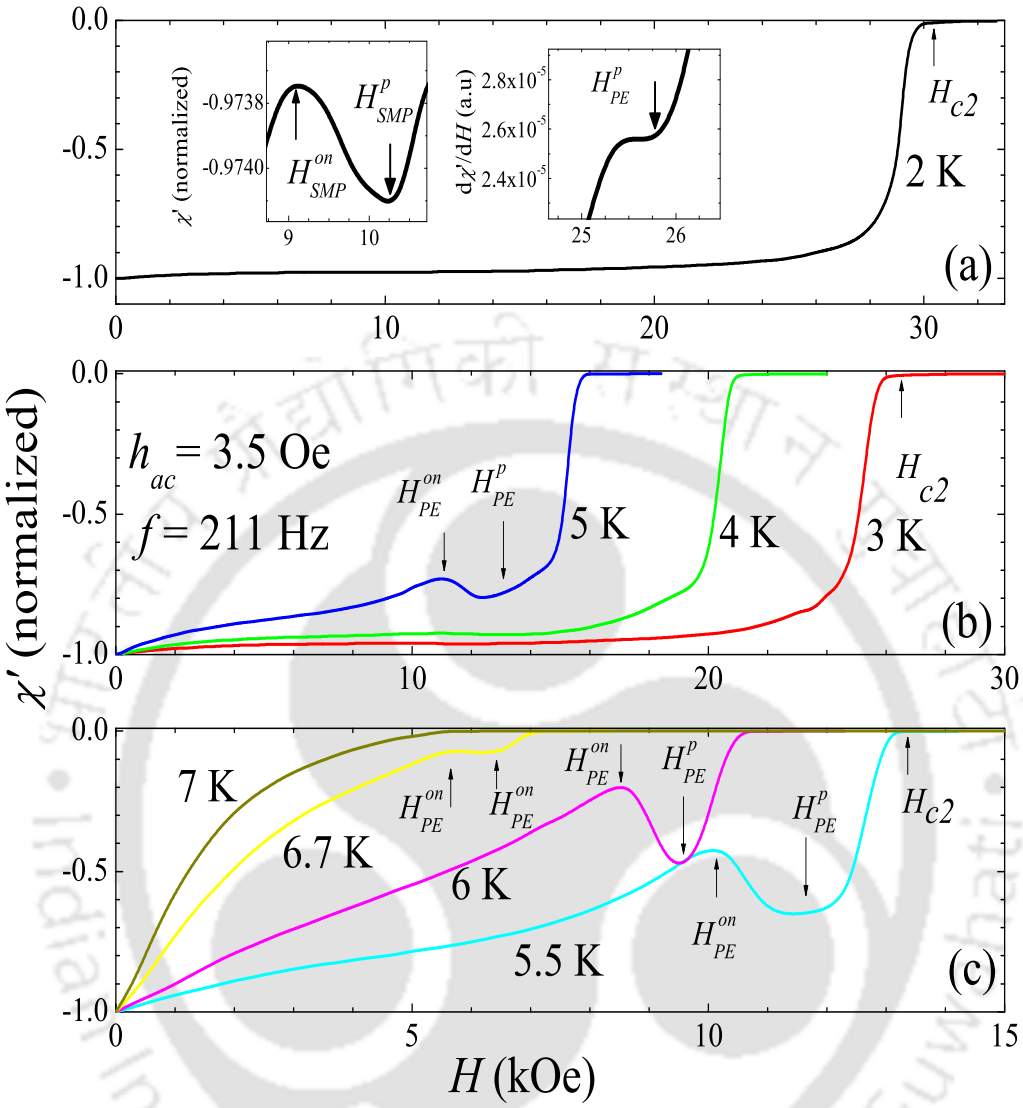

Figure 3.6: *Field dependence of the normalized (Normalised with -χ' value at 0 Oe) isothermal in-phase ac susceptibility data in a single crystal of $Ca_3Rh_4Sn_{13}$ measured with temperatures ranging from 2 K to 7 K with h_{ac} = 4 Oe and frequency, f = 211 Hz. (a) χ' vs. H at 2 K where the first inset shows the enlarged portion of the SMP region where the H^{on}_{SMP} and H^{p}_{SMP} are marked with arrows. The second inset shows the PE region via a derivative plot and the H^{p}_{PE} is marked with an arrow. (b) χ' vs. H plots at temperatures 3 K, 4 K and 5 K. (c) χ' vs. H at temperatures 5.5 K, 6 K, 6.7 K and 7 K. All the curves are meeting at the upper critical field, H_{c2} at zero χ' value (For example, H_{c2} of 2 K curve is marked in (a)).*

Therefore we considered it fruitful to perform isothermal ac susceptibility measurements to corroborate the unusual result of non-monotonicity in the thermal evolution of the SMP.

Interestingly, we have observed the signatures of SMP in addition to the PE anomaly in the same field scan. This is the first report of observation of SMP via ac susceptibility measurements in a low T_c superconductor. Fig. 3.6 shows normalized (Normalised with a -χ' value at 0 Oe) in-phase ac susceptibility vs. field with different temperatures. The main curve of Fig. 3.6(a) shows the χ' vs. H at 2 K and the first inset shows the expanded SMP regime where the H^{on}_{SMP} and H^{p}_{SMP} are marked with arrows and the second inset shows the H^{p}_{PE} via the derivative plot. Fig. 3.6(b) shows χ' vs. H at temperatures 3 K, 4 K and 5 K. After 4 K, the attestation of the PE region is well noticeable. Hence, at 5 K we have marked H^{on}_{PE} and H^{p}_{PE} with arrows. We observed the signature of SMP only upto 5 K and after that the SMP anomaly probably merged with the PE region as in the dc magnetization measurements. Fig. 3.6(c) shows χ' vs. H at temperatures 5.5 K, 6 K, 6.7 K and 7 K. Here we can see that the PE attestation upto T = 6.7 K and above 6.7 K the PE collapses completely.

Fig. 3.7 present a collation of the isofield in-phase ac susceptibility data recorded with h_{ac} = 4 Oe and frequency, f = 211 Hz with different constant fields from 1 kOe to 21 kOe. The 1 kOe and 5 kOe χ' vs. T curves ramp in a featureless manner but the superconducting transition is broader. Above 5 kOe, the peak effect starts to attest its presence by making a peak in the χ' vs. T curve. From 8 kOe onwards, one can observe the PE across the temperature region. The onset and peak positions, T^{on}_{PE} and T^{p}_{PE} of the PE anomaly are marked with arrows in Fig.3.7. However, we were unable to notice any signature of SMP phenomena from the isofeild ac susceptibility measurements. In the mixed state, the oscillating ac field can push the Bragg glass state to an equilibrium disordered vortex glass state upto the onset of PE. Hence, one can observe only an amorphous phase transition (*i.e.*, PE transition) in the χ' vs. T curve. The PE is very sharp in the intermediate field range, hence above 5 kOe we could clearly see the peak effect anomaly. From 13.5 kOe onwards, the number of

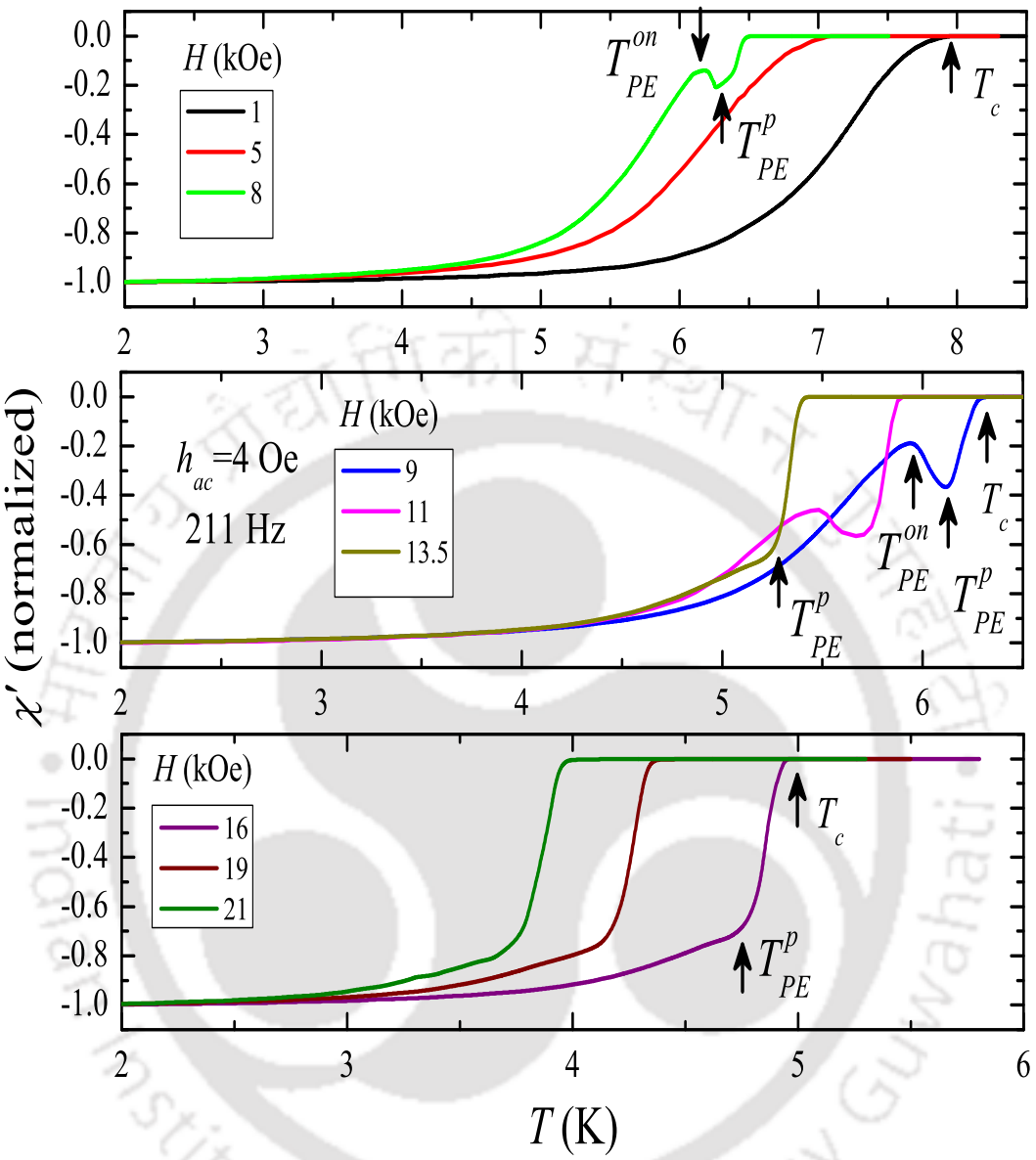

Figure 3.7: *Temperature dependence of the normalized (Normalized with -χ' value at 1.8 K) values of the in-phase ac susceptibility in $Ca_3Rh_4Sn_{13}$ measured with an applied frequency 211 Hz and an amplitude, h_{ac} = 4 Oe. (a) χ' vs. T data plots at 1 kOe, 5 kOe and 8 kOe and the transition temperature T_c of 1 kOe curve is marked in the figure. At 8 kOe, the onset and peak positions of the PE anomaly are marked with arrows as T_{PE}^{on} and T_{PE}^{p}. (b) χ' vs. T data plots at field values 9 kOe, 11 kOe and 13.5 kOe. (c) χ' vs. T at 16 kOe, 19 kOe and 21 kOe.*

vortices forming inside the crystal is more. Hence, the driving ac field is unable to pick the onset of the PE, however it picks the peak of the PE transition (T_{PE}^{p}).

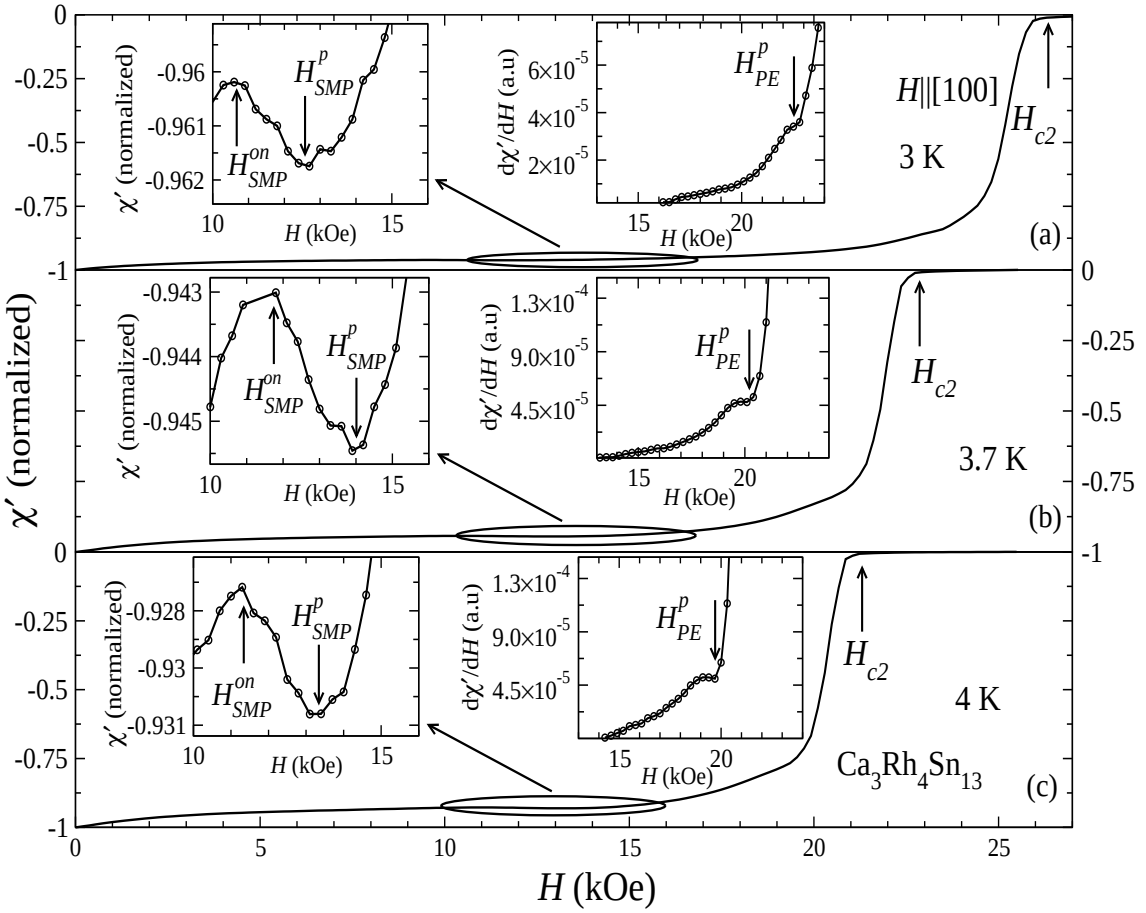

Figure 3.8: *Plots of normalized ac susceptibility ($\chi'(H)/\chi'(0)$) vs. applied magnetic field in a single crystal of $Ca_3Rh_4Sn_{13}$ at (a) 3 K (b) 3.7 K (c) 4 K. The upper critical field H_{c2} is marked with arrows. The circled region is expanded and plotted in the inset of all the panels. H^{on}_{smp} and H^{p}_{smp} are shown in the insets. The other inset is a plot of $d\chi'/dH$ versus H in arbitrary units (a.u). The location of PE peak pointed with an arrow (H^{p}_{PE}).*

The field dependencies of the in–phase ac susceptibility data (normalized to the saturated value of χ' in zero applied field) at various temperatures (3 K, 3.7 K and 4 K) are displayed in Fig.s 3.8 (a)–(c). The left insets show enlarged views of the circled portions which demonstrate the ubiquitous SMP in the isothermal ac susceptibility measurements. The onset and peak positions of the SMP anomaly are marked in each inset. As mentioned earlier, PE phenomenon was determined by using a derivative plot, $d\chi'(H)/dH$ vs. H (see the right inset in each panel of Fig. 3.8). The ac susceptibility data confirm the non-monotonicity of H^{on}_{smp} and H^{p}_{smp} as the temperature increases from 3 to 4 K. However, we noted that the values of

H^{on}_{smp} and H^{p}_{smp} in the ac susceptibility measurements were lower than those obtained from dc magnetization measurements. We believe that the presence of the ac driving force in the ac susceptibility measurements has resulted in inducing the BG/VG transition at a lower threshold value. The well ordered BG state extending up to a higher limit during the dc magnetization measurements is the metastable superheated state which transforms to a relatively less ordered VG like phase on shaking of the vortices in the BG phase. One can thus obtain the spinodal limit ($H_{spinodal}$) [98] of the order–disorder (BG to VG) transition from the ac susceptibility measurements. The onset and peak fields of the PE as determined from the χ' data overlap with those obtained from the dc magnetization data and they decrease with increase of temperature, as expected.

3.5 Step change in equilibrium magnetization across SMP and PE

As inferred from the previous figures, the SMP and PE are manifested by anomalous increases of J_c which in turn relate to rapid reductions in the spatial correlation volume across these regime. If these reductions are a result of a phase transition then one expects to observe a step change in the equilibrium magnetization (M_{eq}) which is a signature of the thermodynamic first order phase transition. As noticed, the measured magnetization is irreversible in this domain. This is because the measured magnetization is a combination of the equilibrium magnetization and the magnetization caused by the circulating shielding currents of magnitude J_c. Within a conventional critical state model [20, 70], the value of M_{eq} is calculated from the equation $M_{eq} = (M_{\downarrow}(H) + M_{\uparrow}(H))/2$, where $M_{\uparrow}(H)$ and $M_{\downarrow}(H)$ are the magnetization values along the forward and the reverse hysteresis legs, respectively.

The main panel of Fig. 3.9(a) shows a portion of the four quadrant *M-H* loop of $Ca_3Rh_4Sn_{13}$ at 3.5 K. The dotted curve represents the equilibrium magnetization line, M_{eq}.

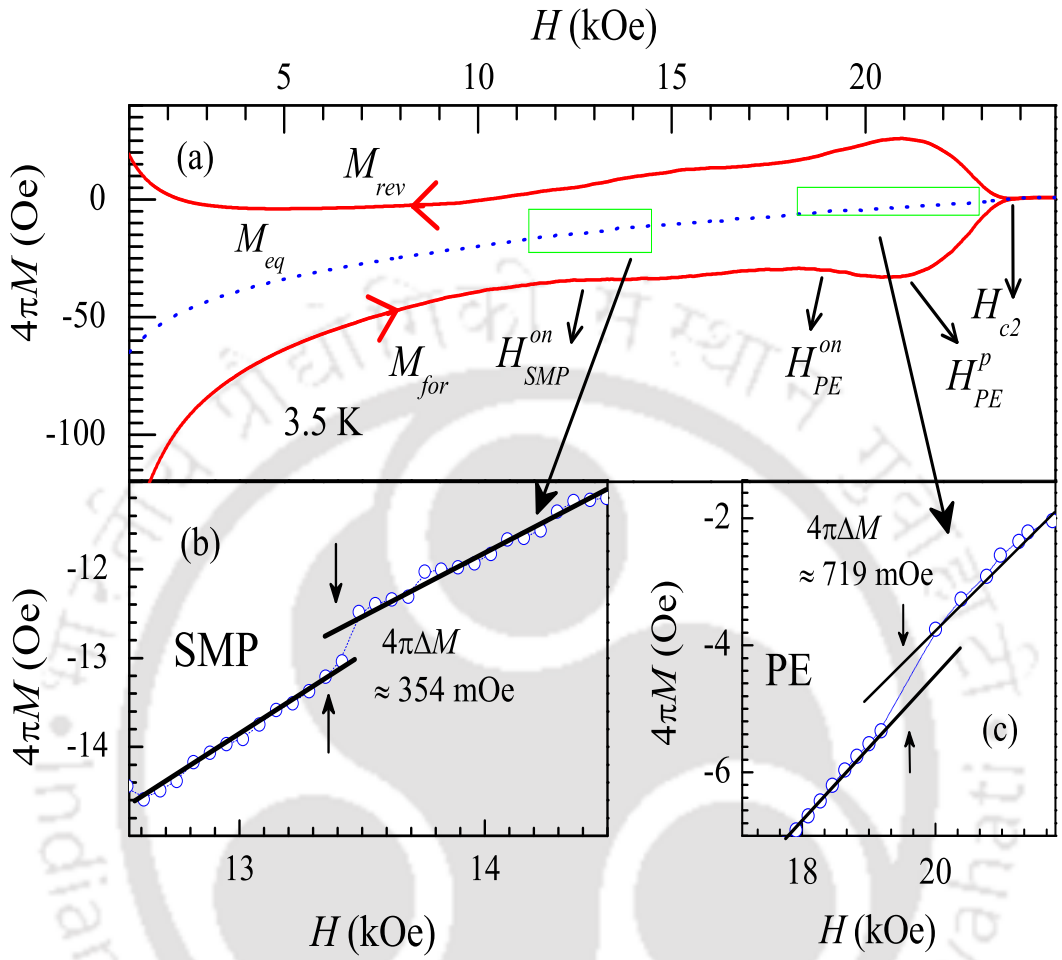

Figure 3.9: *The panel (a) shows a portion of the M-H loop of $Ca_3Rh_4Sn_{13}$ at 3.5 K. Panels (b) and (c) show the enlarged view of the step changes in the SMP and PE regions, respectively. The solid lines are guide to the eyes.*

Interestingly, we observed two step changes in the same M_{eq} line which are highlighted inside the rectangular boxes. The enlarged view of the step changes is shown in Fig. 3.9(b) and (c). In Fig. 3.9(b) the line with circles represents the M_{eq} line and the solid lines are just guide to the eye. The change in M_{eq} which occurs at an applied field of 13.3 kOe is of magnitude $4\pi\Delta M \sim 354$ mOe. We noticed that this change in the M_{eq} juxtaposes with the onset of the SMP anomaly. In Fig. 3.9(c), we extrapolated the M_{eq} lines before and after the PE anomaly (solid lines) and obtained a step change in M_{eq} of magnitude $4\pi\Delta M \sim 719$

mOe. Here the jump in M_{eq} appears at a field value $\approx$ 19.7 kOe which is in between the H_{PE}^{on} and H_{PE}^{p}. The values of the observed steps in the M_{eq} lines of the present crystal are consistent with the results of $Bi_2Sr_2CaCu_2O_8$ and $YBa_2Cu_3O_7$ crystals [30, 99].

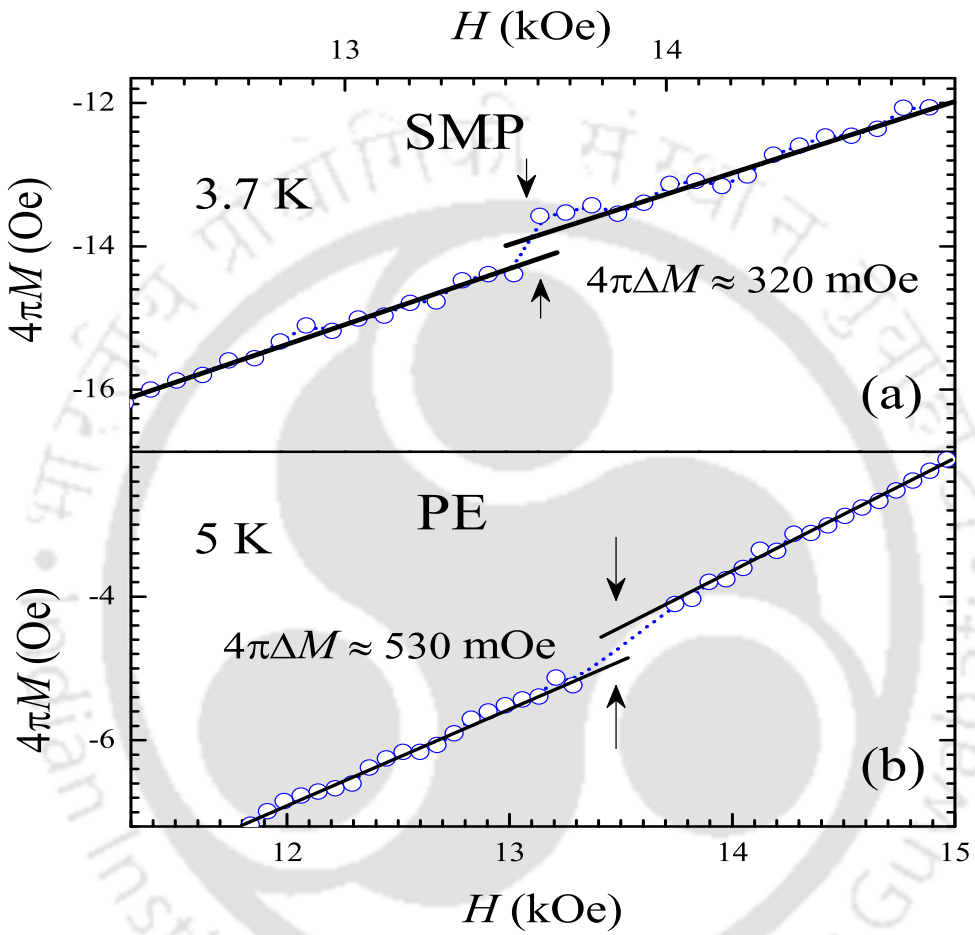

Figure 3.10: *Panel (a) shows the step change in the M_{eq} line of $Ca_3Rh_4Sn_{13}$ at 3.7 K in the SMP region. The solid lines are just guide to the eyes. Panel (b) shows the discontinuous step change in the M_{eq} line which is obtained by extrapolating the M_{eq} line before and after the PE anomaly (solid lines) at 5 K.*

Now at a constant field of 13.5 kOe, we try to observe jumps in M_{eq} across the onset of SMP and across the PE phase boundaries. Fig. 3.10(a) shows the step change in the M_{eq} line at 3.7 K, which aligns with the onset of SMP phase boundary. Fig. 3.10(b) depicts the step change in the M_{eq} line at 5 K which lies in the PE region. The values of the $4\pi\Delta M$ in

the SMP and PE regions are 320 mOe and 530 mOe, respectively. We observed a maximum of 75 mOe noise in the measured value of step changes from the M_{eq} data.

It is worth mentioning that the sharp step change in the equilibrium magnetization across the SMP regime occurs in juxtaposition with the onset of the SMP. The step change in the M_{eq} across the PE regime is derived from the difference in M_{eq} before and after the PE anomaly. The entire PE regime is a region of coexistence of ordered–disordered phases, implying the first order nature of the phase transition [31]. Here, one observes two jumps in the equilibrium magnetization at two different temperature (or field) domains for a particular field (or temperature).

We have collected all the $4\pi\Delta M$ values from the SMP and PE region and calculated the change in entropy (ΔS) per vortex per unit cell distance along the [100] axis of the cubic crystal with the help of Clausius–Clapeyron equation

$$\Delta S = -\frac{\phi_0 d}{H_{on}} \frac{\Delta B}{4\pi} \frac{dH_{on}}{dT} \tag{3.1}$$

where ϕ_0 is the flux quantum, d is the unit cell distance along the [100] axis, ΔB is the measured step change in magnetization and H_{on} is the onset field point of the anomaly.

Fig. 3.11 shows the step change ΔB (or $4\pi\Delta M$) and the calculated ΔS versus temperature across the SMP region. The values of ΔS compares well with the data reported in the high T_c superconductor BSSCO [30]. Below 3.7 K the ΔS is negative which signifies that the entropy is higher in the ordered lattice than in the disordered state. This is not surprising because even though the entropy is higher in the ordered state the extra entropy might be absorbed by the additional degrees of freedom.

Fig. 3.12 shows the calculated ΔB and the associated change in entropy across the PE region. Here, one observes a monotonic decrease in ΔB and ΔS with increase of temperature, a feature not unusual in the theoretical framework where ΔS is predicted to decrease monotonically with temperature according to the equation $\Delta S(T) \approx (0.1d/\varepsilon)\sqrt{H_{PE}^{on}(T)/\phi_0}$,

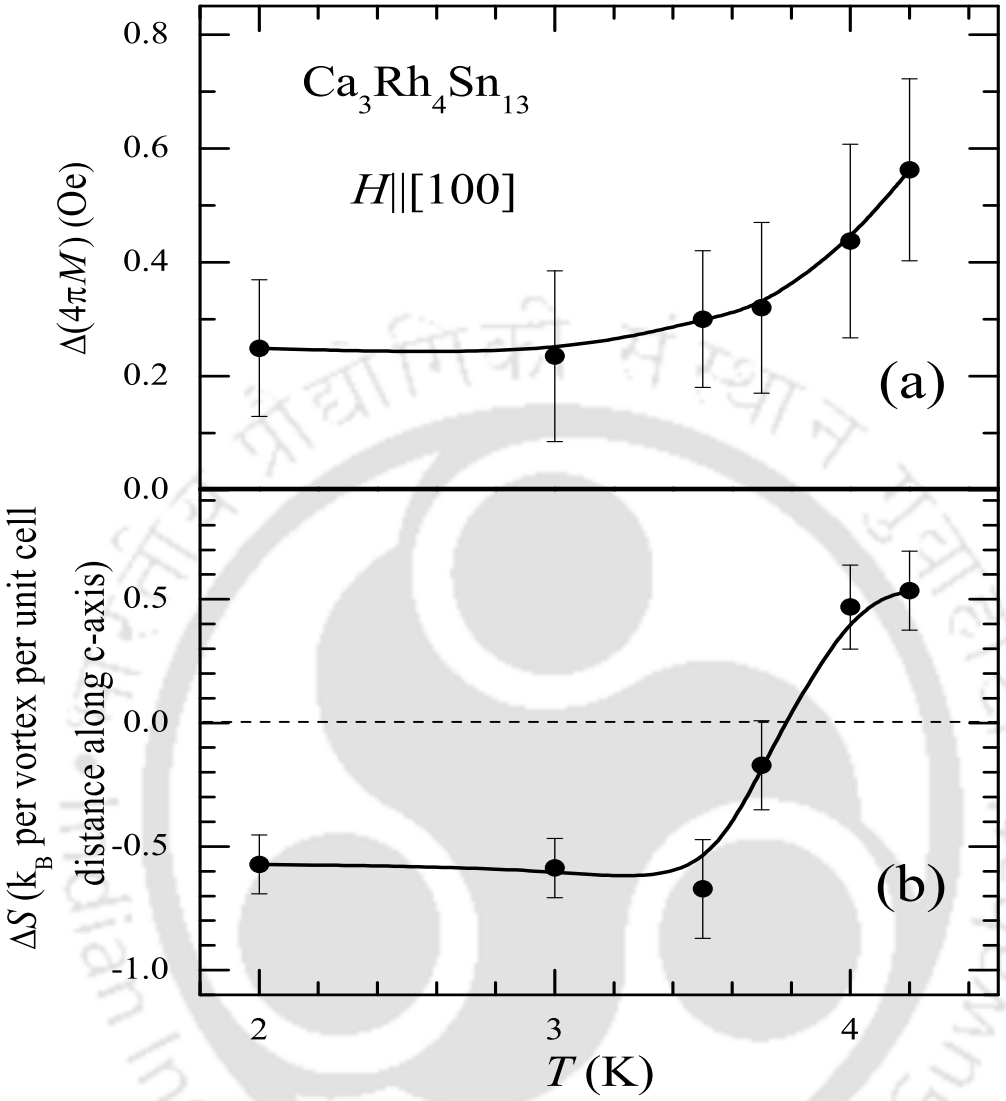

Figure 3.11: *(a) The measured height of the discontinuous step ΔB and (b) the entropy difference ΔS per vortex per unit cell distance along the c-axis in the SMP regime.*

where $\varepsilon = 1$ is the anisotropy parameter [100]. Although the variation of ΔS with T is seen to be compatible with theoretical predictions, the observed value of ΔS ($\approx 2.5\times10^{-3}$ k_B at 4.5 K) is three orders of magnitude larger than the theoretically estimated one. Thus our observations are in contrast with the diverging behavior noticed in BSSCO [100].

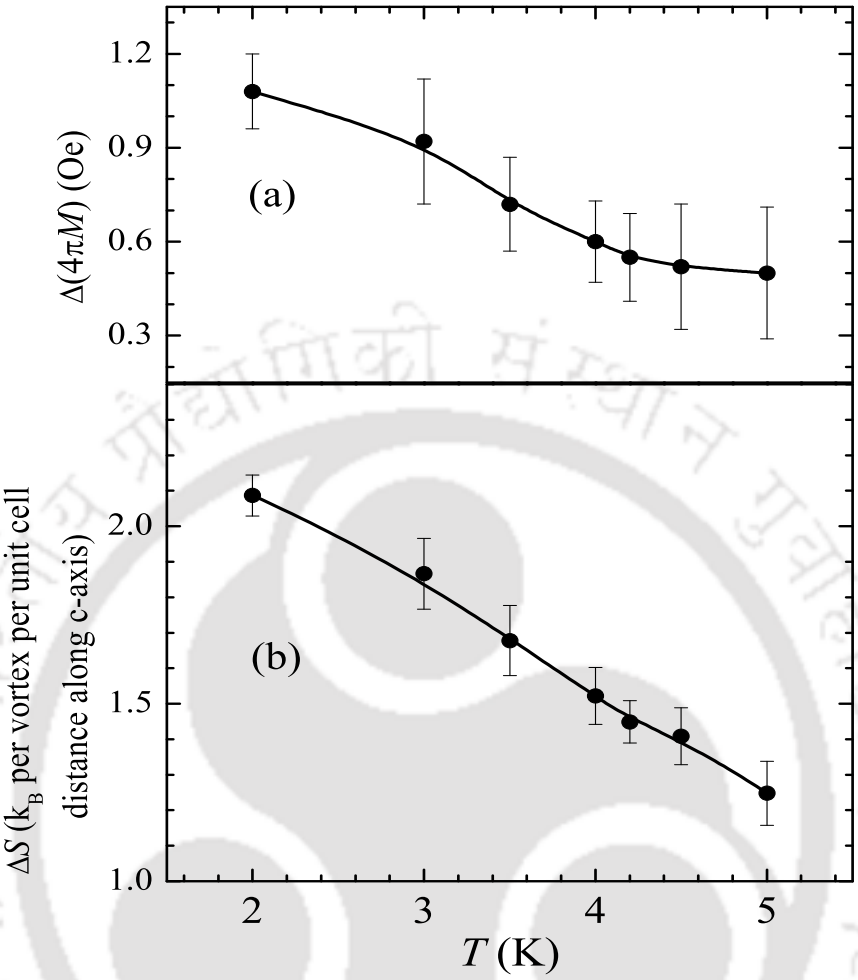

Figure 3.12: *(a) The measured height of the discontinuous step ΔB and (b) the entropy difference ΔS per vortex per unit cell distance along the c-axis in the PE regime.*

3.6 Vortex phase diagram of $Ca_3Rh_4Sn_{13}$ single crystal

Finally, the vortex phase diagram in the present single crystal of $Ca_3Rh_4Sn_{13}$ is illustrated in Fig. 3.13. The onsets and the peak positions of the two anomalies (SMP and PE) and the upper critical field (H_{c2}) are denoted with separate symbols and lines. H^{on}_{PE} and H^{p}_{PE} decrease monotonically with increase in temperature and follow the temperature dependence of H_{c2}. The BG to VG (order–disorder) transition line marked by the onset of the SMP, H^{on}_{SMP}, shows an upward trend until the reduced temperature, $t(t = T/T_c(0))$, attains a value

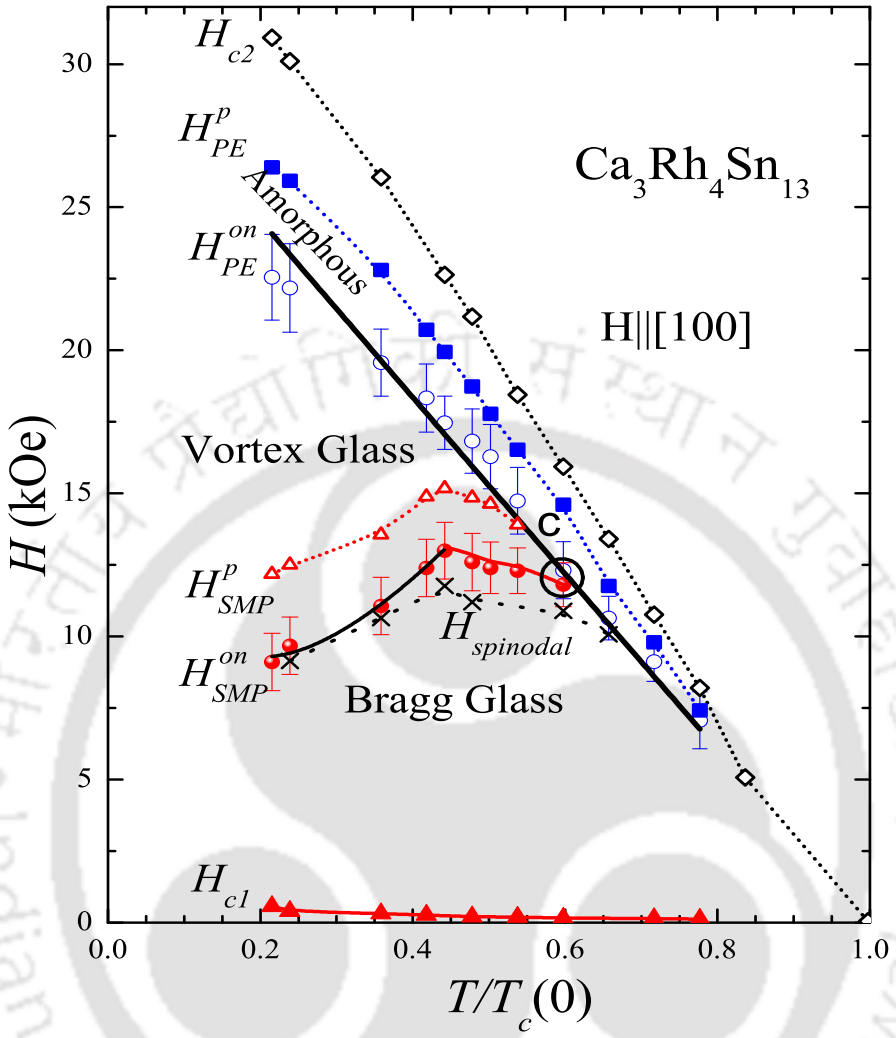

Figure 3.13: *Plot of the vortex phase diagram in the given single crystal of $Ca_3Rh_4Sn_{13}$. The thick continuous lines are fits to the theoretical expressions given in the text. The dotted lines are drawn just to guide the eye. The encircled region C shows where the onset of the SMP merges into that of the PE.*

of 0.44. Above $t \approx 0.44$, H^{on}_{SMP} reverses its nature and decreases with increase in temperature until it merges with H^{on}_{PE}. Thereafter the distinction between the two anomalous variations gets blurred, and one witnesses only one composite event marking the order–disorder transition. The field–temperature region where the two anomalous variations of J_c cease to exist distinctly gives rise to an impression that a multicritical point may be buried underneath (see the encircled region C in Fig. 3.13).

Kierfeld and Vinokur [63] suggested that the temperature dependence of the disordering transition, i.e., the onset of the second magnetization peak, can be described by the relation $H^{on}_{SMP} = H_0(1-t_d)^{5/9}t_d^{-10/3}exp(2Ct_d^{\alpha}/3)$, where H_0 is a constant, $t_d = T/T_{dip}$, C is a numerical factor ~ 25, the exponent $\alpha \approx 3/8$ and T_{dip} is the depinning temperature (the temperature where the magnetic hysteresis loop vanishes). The thin black line in Fig. 3.13 indicates that the onset of the SMP data (i.e. H^{on}_{SMP}) can be fitted fairly well to the above relation until $t \approx 0.44$. It should be mentioned that even though the equation is suggested for high T_c superconductors it fits very well in our case too. For the case of the PE line the expression $H^{on}_{PE} = H(0)(1-(T/T_c)^n)$ has been used [14]. The thick solid line shows the fit to our data with the values n = 1 and H(0) = 37 kOe.

It is interesting to note in the phase diagram of Fig. 3.13 that the ordered BG phase is sandwiched between an amorphous phase on the high temperature side and the less ordered multi-domain VG on the low temperature side, thereby conforming to the notion of (disorder induced) inverse melting. (Normally, rising the temperature makes melting of a solid. Converse of melting phenomena is the inverses melting where heating of a liquid transforms the liquid to solid!.) It is worth mentioning that the loss of elastic energy of the VG phase is balanced by the gain in the pinning energy of the BG phase in this region. We have also drawn the locus of the spinodal limit ($H_{spinodal}$) of the BG to VG transition and it follows a similar non-monotonic trend to H^{on}_{SMP}, just emphasizing the nature of inverse melting in the phase diagram.

Further, we also observe a 'vortex slush' region between H^{on}_{SMP} and H^{p}_{SMP} in the temperature range $t \sim 0.44$–0.60. Here the weakly pinned BG phase first goes into a dislocation induced VG phase and then via a PE phenomenon it goes into an amorphous regime. Such evidence of the vortex slush regime has been previously reported in YBCO [23]. Another significant finding in our work is the notion of a multicritical point C where the H^{on}_{PE} line merges with the H^{on}_{SMP}. The composite line also disappears at $t \approx 0.78$ which may possibly

end at another critical point. The appearances of such multicritical points with the same physical basis has also been pointed out in high T_c superconductors [14, 16].

The phase diagram of the FLL which shows the order–disorder phases and the transformation between them should be too dissimilar between isotropic low T_c superconductors and anisotropic high T_c superconductors. This may be because the anisotropy effects cause different phase boundaries lying close or even coincident with each other making them indistinguishable. For highly anisotropic superconductors like BSSCO the other direction is dominant with Josephson vortices and hence the physics becomes entirely different. The crystal of $Ca_3Rh_4Sn_{13}$ studied in this thesis had $J_c/J_0 \approx 10^{-4}$ (where J_c is the depinning and J_0 is the depairing current density) which is intermediate between ultra-clean low T_c superconductors, like 2H-$NbSe_2$, and high T_c superconductors. Hence this crystal provided an ideal platform for simultaneously observing both the phenomenon of the SMP, generally seen only in high T_c materials, and the PE, observed mostly in ultra-clean low T_c materials. The Ginzburg number ($G_i \approx 10^{-5}$) is much lower than for high T_c superconductors indicating that the effect of thermal fluctuations is minimal except close to the H_{c2} phase boundaries, implying that the amorphous region arising due the PE will be narrow. In short, in high T_c superconductors the disordered regions like liquid, amorphous, etc will cover a large area of the phase space compared to the low T_c superconductors. However, parameters like J_c/J_0 and G_i can also be tuned to show similar disordered regions in low T_c superconductors.

3.7 Variation of SMP in another single crystal of $Ca_3Rh_4Sn_{13}$

We have grown another set of $Ca_3Rh_4Sn_{13}$ single crystals and selected one single crystal among them and named it as crystal *X*. We cut the crystal-*X* in the [100] direction and performed the magnetization measurements. Crystal *X* shows SMP and PE in its isothermal magnetization loops. The magnetic (*H*-*T*) phase diagram of crystal *X* is shown in Fig. 3.16.

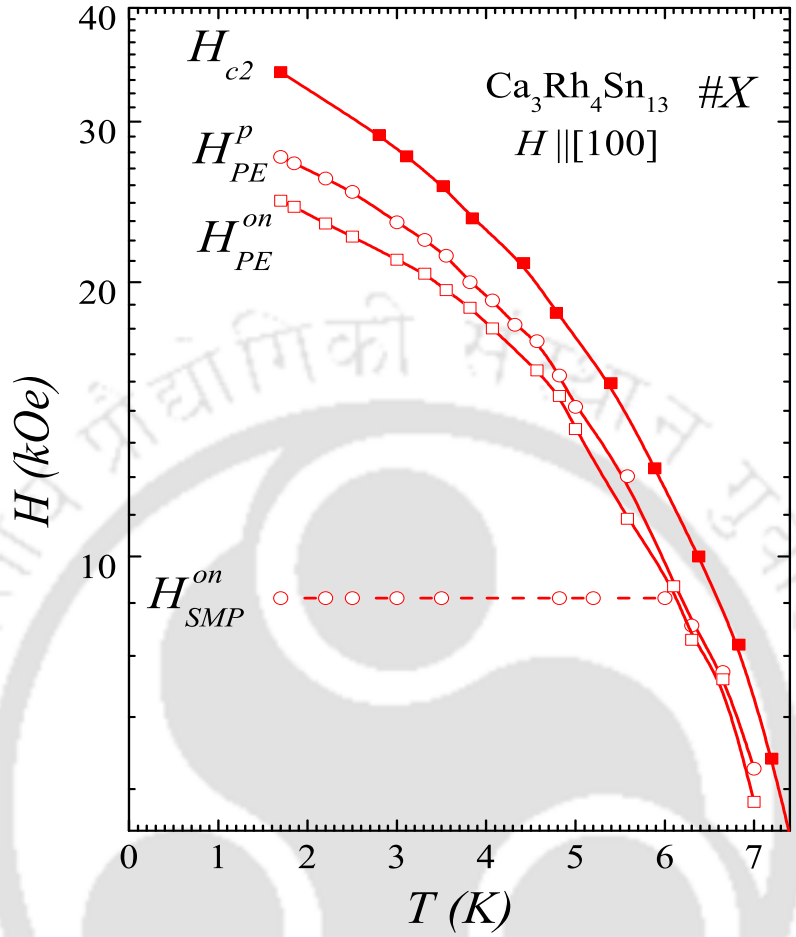

Figure 3.14: *Plot of the vortex phase diagram of another single crystal of* $Ca_3Rh_4Sn_{13}$ *(crystal-X).*

Here the H_{c2}, H^{on}_{PE} and H^{p}_{PE} lines are showing the same behavior as the previously studied crystal (*cf.* Fig. 3.13). However, the order-disorder line- H^{on}_{SMP} appears as flat with increase in temperature which is dissimilar with the previously studied crystal. This kind of flat SMP line has already been reported in literature [11].

To find the reason for this difference, we have calculated J_c of the crystal X along with the previously studied crystal (say crystal-Y) at 1.7 K and plotted in Fig. 3.15. Here crystal Y shows higher J_c than crystal X. Hence, one can conclude that the value of J_c affects the behavior of SMP line in $Ca_3Rh_4Sn_{13}$ single crystals. Similar behavior of second mag-

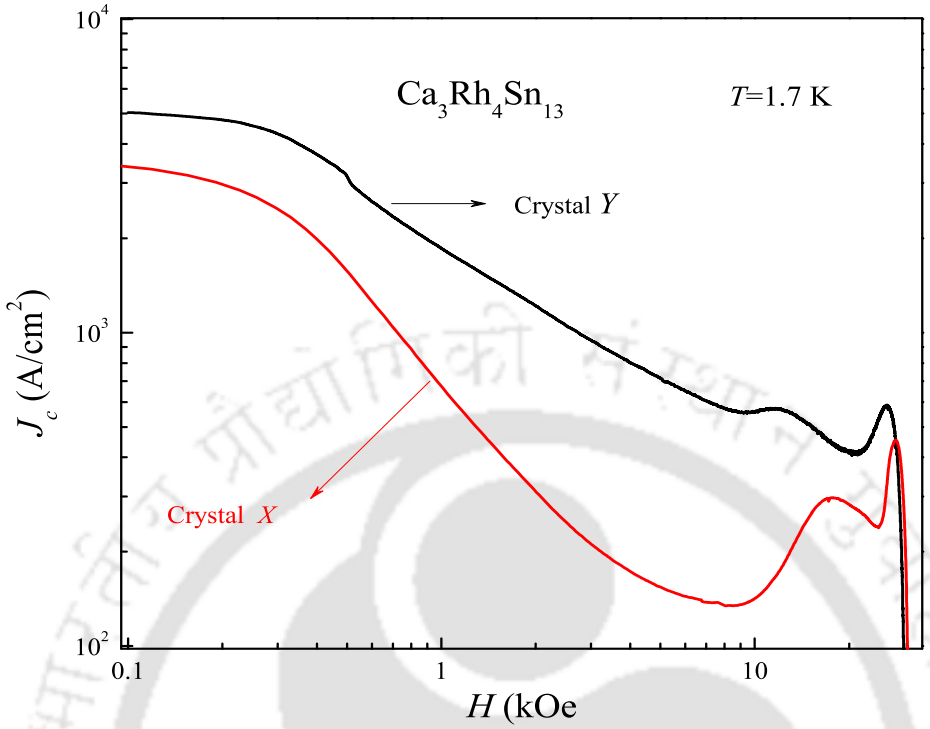

Figure 3.15: *J_c plots of the crystal X and Y at 1.7 K.*

netization lines has been reported in high T_c superconductor, BSSCO [16]. In BSSCO, an optimally-doped single crystal makes a flat second magnetization line whereas an over-doped single crystal shifts the second magnetization line upwards which is in concurrence with our measurements.

3.8 Magnetization noise analysis across SMP and PE

The origin of SMP and PE phenomena are different, but they can be treated as a disordering phenomenon of the vortex lattice. Dynamic variations of the relative fraction of the disorder gives rise to metastability effects both across the SMP and PE regions [12, 26, 31–33, 45]. Hence, such complex and possibly nonlinear system may produce spontaneous reorganizations in its phase. Such reorganizations have characteristic frequencies which have been already observed in the transport measurements of the 2H-$NbSe_2$ single crystals [101]. Low

frequency noise measurements also provide the information of such reorganizations [90]. Hence such intrinsic reorganization would also leave an imprint in the power spectrum of noise in the magnetization data. We believe that the present $Ca_3Rh_4Sn_{13}$ single crystal is an ideal platform to investigate such low frequency reorganizations.

3.8.1 Magnetization vs. time (*M–t*) measurements

Once again we have shown the phase diagram of $Ca_3Rh_4Sn_{13}$ single crystal in Fig. 3.16. From the (*H-T*) phase diagram, we choose a temperature, T = 3 K where both the SMP and PE anomalies are observed in the isothermal magnetization curves. As mentioned earlier, the origin of SMP and PE are different, but both finally results in the disordering of the vortex lattice. Hence to understand the effect of these two phenomena only we need to keep the thermal fluctuations constant throughout this measurement. Therefore, we perform the magnetization vs. time (*M–t*) measurements in the selected field points marked with circles at 3 K in the (*H-T*) phase diagram (*cf.* Fig. 3.16).

We used the following procedure for measuring the *M–t* in the selected field points, by zero field cooled (ZFC) method. First, the applied field was swept at a constant rate 10 Oe/s and at the selected value of the field, it was held constant until the magnetic field in the magnet was stabilized. Then the magnetization of the sample was recorded as a function of time. We have also performed the *M–t* measurements in the following method. We cooled the sample to 3 K by applying a field of 50 kOe. Then we decreased the field to the required value (marked by points in Fig. 3.16) at a rate of 10 Oe/min and then recorded the *M–t* data. The results are found to be similar in both modes of acquiring the *M–t* data. Hence we present only the data of the previous method.

The measured *M–t* curves of the selected field strengths at 3 K are shown in the panels (i)–(vi) of Fig. 3.17. It is observed that the fluctuation in the *M–t* curve is very small at 5 kOe (Fig. 3.17 (i)), as it belongs to the ordered BG phase. As the applied magnetic field

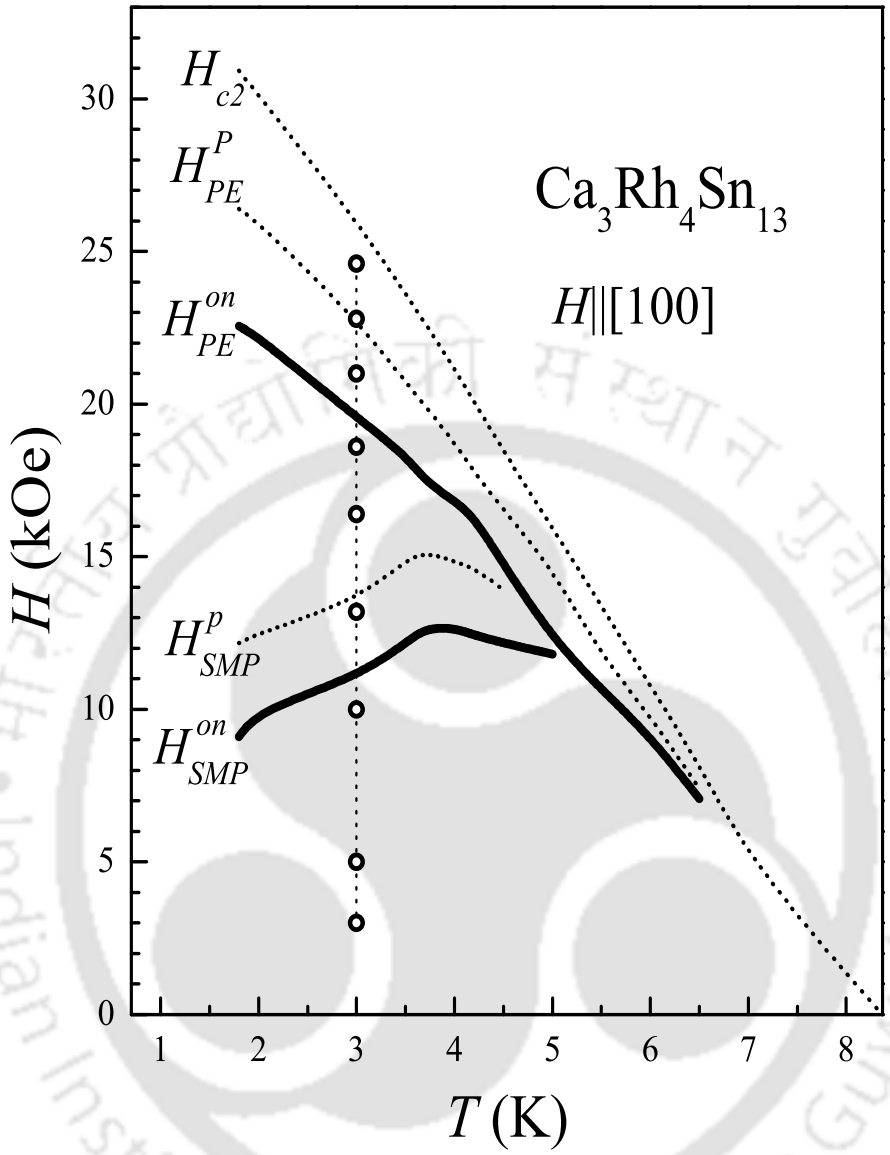

Figure 3.16: *The magnetic field (H) vs. temperature (T) phase diagram of a single crystal of $Ca_3Rh_4Sn_{13}$ (same as Fig. 3.13). The line at 3 K contains small circles, which mark the positions in (H-T) where the magnetization vs. time measurements has been carried out.*

increases these fluctuations also increases. Fig. 3.17 (ii) shows the *M–t* at 10 kOe which is very near to the onset of the SMP anomaly. The fluctuations for 13.2 kOe depicted in panel (iii) is close to the maximum of SMP and panel (vi) depicts the fluctuation for the maximum of PE (22.8 kOe). The *M–t* at 18.6 kOe is very near to the onset of the PE anomaly (Fig. 3.17 (iv)). We observed a small decay in magnetization value in the SMP region but there

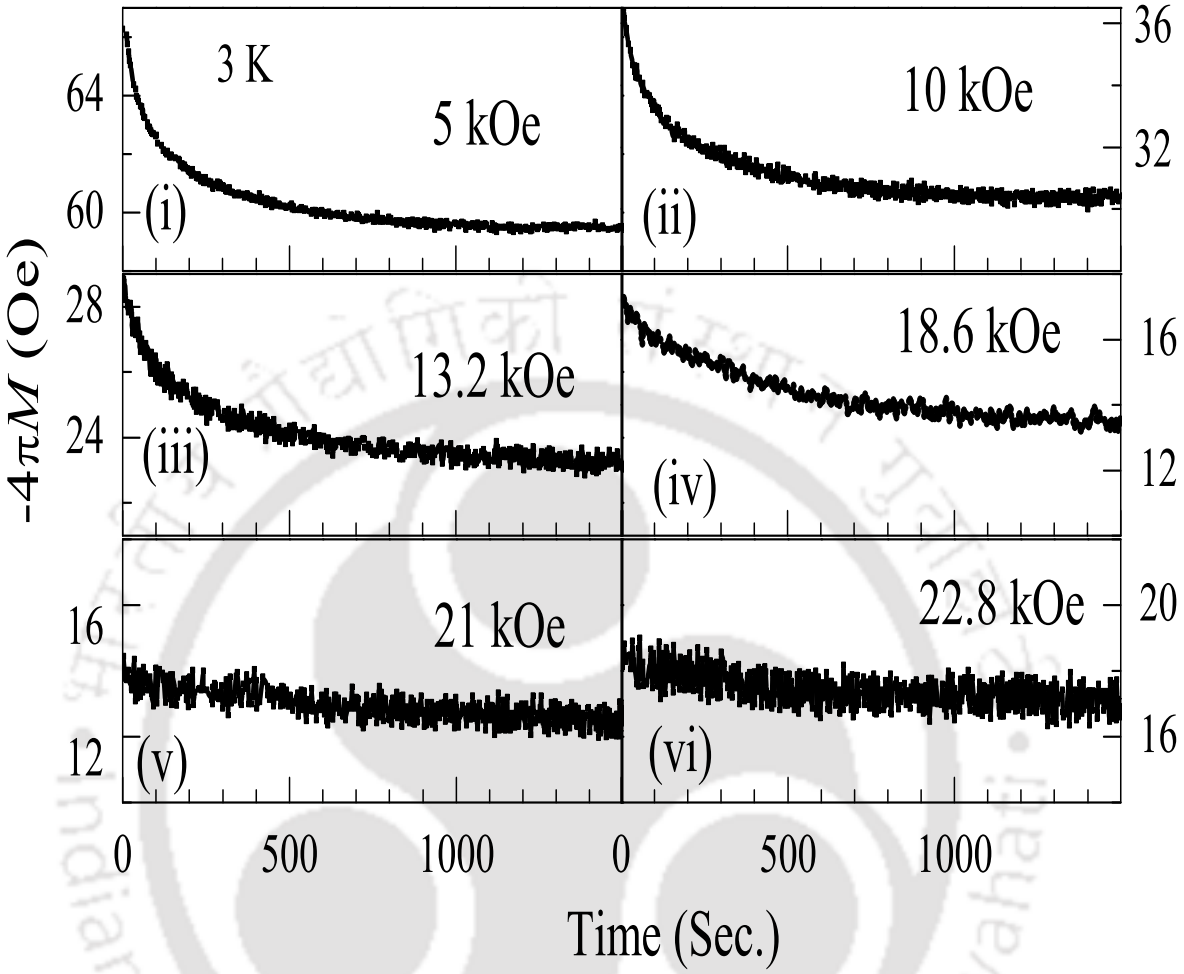

Figure 3.17: *The magnetization vs. time M–t plots at different magnetic fields at 3 K. The chosen magnetic fields are marked as open circles in Fig. 3.16.*

is no considerable decay in magnetization values in the PE region. However, the fluctuation in magnetization data in the PE region is much larger than the SMP region.

For getting a quantitative idea of fluctuations associated with the magnetization data, we calculated the root mean square (R.M.S) magnetization fluctuations (or amplitude of the

magnetization noise) of the *M–t* data.

$$R.M.S\ \ magnetization\ \ fluctuation = \sqrt{\frac{1}{T}\sum_{t_j=1}^{T}(M_i(t_j) - \overline{M_i})^2} \tag{3.2}$$

where T is the time over which one wants to average and $\overline{M_i}$ is the i^{th} time averaged magnetization value.

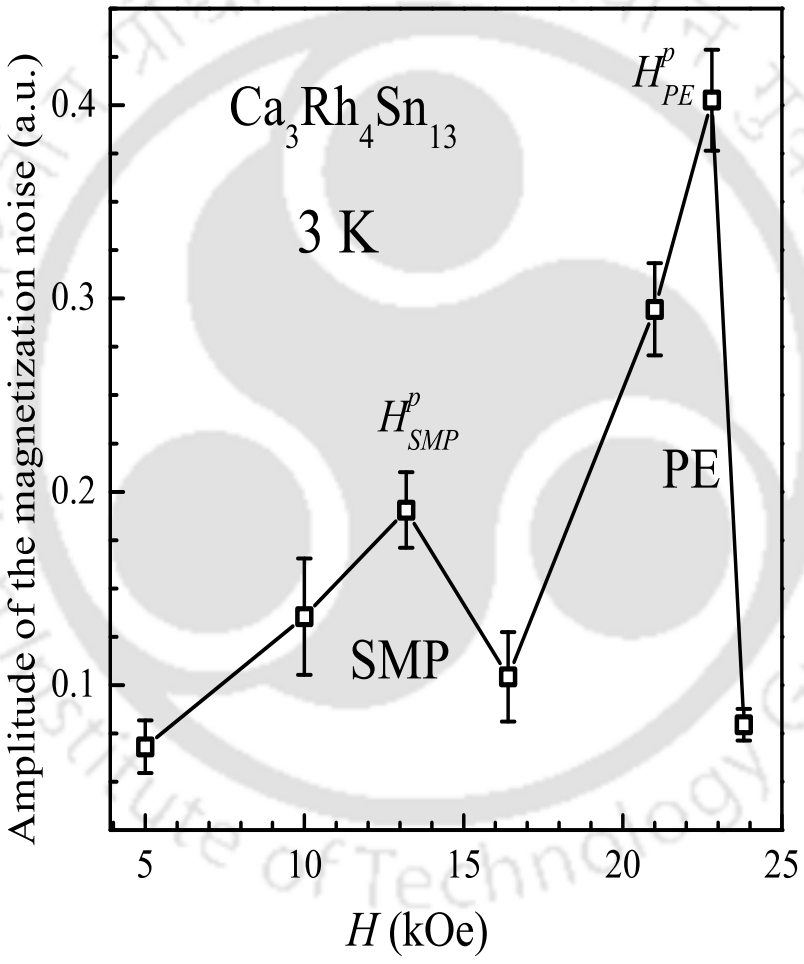

Figure 3.18: *Plot of the amplitude of the magnetization noise in arbitrary units (a.u) vs. applied magnetic field (H) at 3 K of $Ca_3Rh_4Sn_{13}$ single crystal.*

Fig. 3.18 depicts the variation of amplitude of the magnetization noise vs. applied magnetic field at 3 K. The amplitude of the noise shows two peaks, one at 13.2 kOe and

other at 22.8 kOe, which coincide with the H^p_{SMP} and H^p_{PE}, respectively. After the maximum of the SMP the fluctuations in magnetization decreases. This may be due to the partially disordered vortex phase nearly heals up by the arrival of the PE region [33]. The PE region, which is interpreted as the coexistence of ordered and disordered phases, also has a very high amplitude of the magnetic fluctuations as anticipated. After H^p_{PE}, the magnetic fluctuations decrease because the amorphization of the vortex lattice is complete.

3.8.2 1/*f* noise and low frequency resonances

We expect that the reorganizations of the glassy phases may attest characteristic frequencies in the power spectra. Fig. 3.19 shows the power spectrum (*S(f)*) vs. 1/*f* plots of selected applied magnetic fields at 3 K. These power spectra are the prototypes of the different vortex phases of the $Ca_3Rh_4Sn_{13}$ single crystal. Fig. 3.19(a) is the *S(f)* vs. 1/*f* plot at a field of 3 kOe, which lies deep inside the ordered Bragg glass phase. We get a $1/f^{\alpha}$ noise spectrum with an exponent, $\alpha \approx 1.8$. The solid line represents the portion that obeys $1/f^{1.8}$ variation in frequency, with a cutoff frequency at the high frequency side. The $1/f^{1.8}$ variation of the power spectra possibly indicates the self-organized critical nature of this ordered state of the vortex lattice. Inside the mixed phase of a low T_c type-II superconductor, the vortices arrange themselves in an ordered state. The experiment is conducted at low temperatures ($\approx$ 3 K) where the thermal fluctuations are minimal and hence the mutual repulsive interactions between the vortices dominates. As the external magnetic field ramped from zero to the desired field, more and more vortices tries to enter the superconductor and hence a variation of the density of vortices is achieved inside the superconductor.

The Bean's critical state model, a widely accepted simple model, describes a linear density variation of vortices inside the superconductor. This is definitely a self-organized state because the vortices rearrange themselves to form a marginally stable state [102, 103]. Now the surface of the sample acts as a strong pinning site and prevents the vortices to

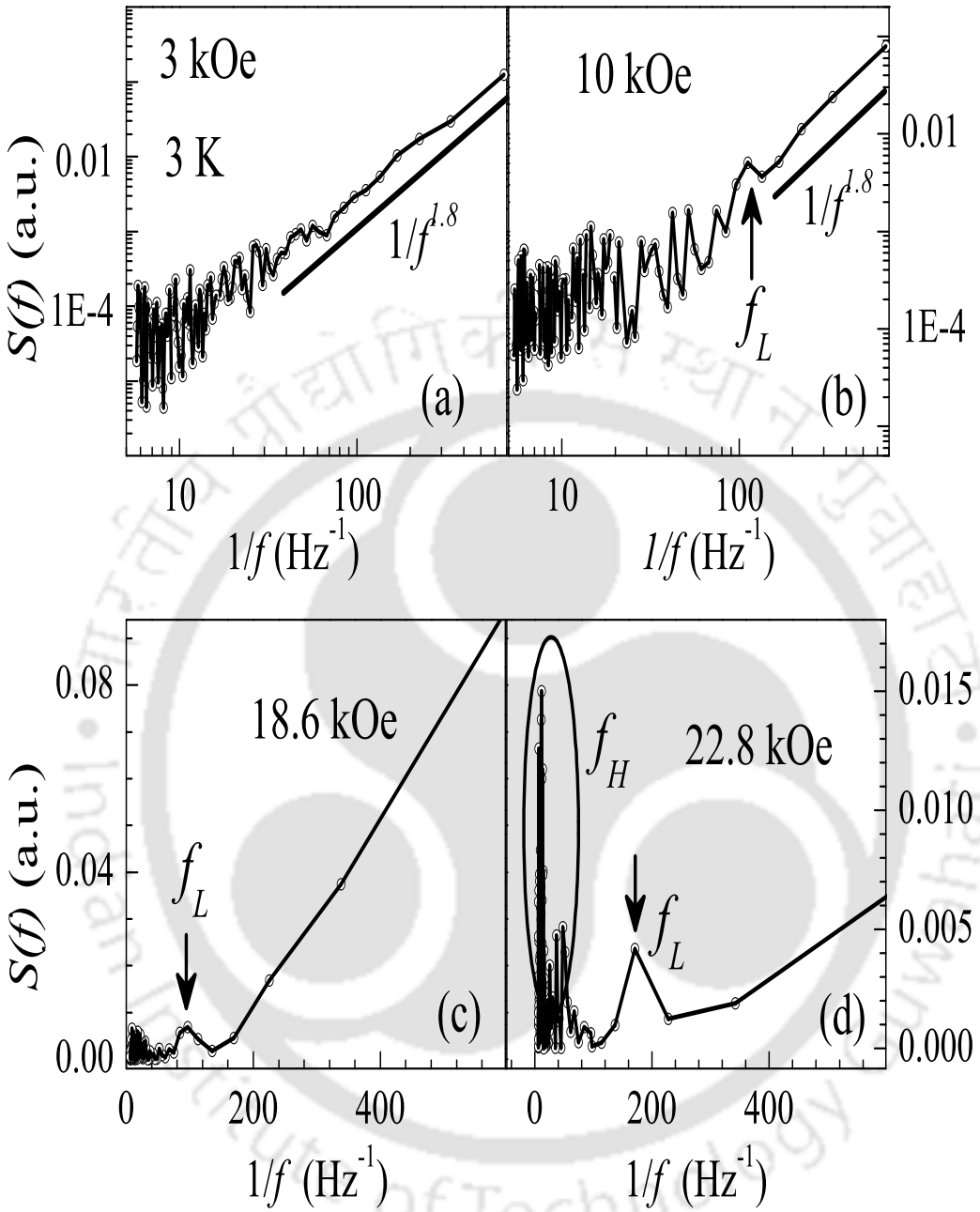

Figure 3.19: *Plots of the power spectrum, S(f) vs. 1/f curves of the magnetization data of different applied magnetic fields (3 kOe, 10 kOe, 18.6 kOe and 22.8 kOe) at T = 3 K. Panels (a) and (b) are in log–log scale whereas (c) and (d) are in linear scale.*

flow very easily inside the superconductor. In order to overcome this extra pinning force, the size of the vortex bundles have to reach a critical state. Hence, the signature of the

critical state is embedded in the formation and the motion of these vortex bundles, which is reflected in the fluctuations of the magnetization. Such fluctuations in the self-organized critical state should have the power-law correlations which is observed at large time scales ($\sim 1/f^{1.8}$) as seen in Fig. 3.19(a) and (b). Then it gradually flattens out at short time scales. This cut-off time indicates the minimum characteristic time to form a discrete bundle in its self-organized critical state. At smaller time scales the noise is generally caused by the motion of the individual vortices moving inside the superconductor.

Fig. 3.19(b) depicts the *S(f)* at 10 kOe which is very close to the onset of the SMP anomaly. We observe $1/f^{1.8}$ nature of variation for a narrower range of frequencies than Fig. 3.19(a). This is natural across SMP the vortex lattice becomes disordered and this leads to the loss of correlation of the vortex lattice. Close to the cut-off frequency one observes a peak in the spectral frequency curve which is marked as f_L ($\sim$0.01 Hz) in the Fig. 3.19(b). We observe that for all fields higher than 10 kOe, there is no significant variation in its magnitude of f_L. The power spectrum near to the onset of the PE anomaly is demonstrated in Fig. 3.19(c). Across the PE region, we find that the power spectrum shows a significant deviation from the $1/f^{1.8}$ nature (*cf.* Fig. 3.19(c) and (d)). However, another set of resonance frequencies emerges whose values are higher than the f_L (*cf.* the elliptical region in Fig. 3.19(d)). This set of frequencies (f_H) have a value which is approximately 10 times larger than the value of f_L. Below f_L (Fig. 3.19(c) and (d)) the power spectra does not show any frequency dependence. The distinct nature of f_L and f_H across the SMP and PE regions implies that the origin of these two phenomenon are different. But the noteworthy result is that the f_L, which is a feature of the SMP, does not vanish even in the PE regime, where complete amorphization of the vortex lattice is anticipated. Similar results of two sets of low frequencies, in the PE region, have been reported in the transport measurements of a 2H-$NbSe_2$ single crystal [101].

3.9 Observation of 1/*f* noise in driven vortex systems via molecular dynamics (MD) simulation

Consider a 2D cross section of N_v vortices driven over a random pinning background at T=0. By treating the vortices and pinning centers as point particles, we obtain the over-damped equation [104–106] of motion of a vortex i in position $\overrightarrow{r_i}$ as

$$\eta \frac{d\overrightarrow{r_i}}{dt} = -\sum_{j\neq i} \nabla U^v(\overrightarrow{r_i} - \overrightarrow{r_j}) - \sum_k \nabla U^p(\overrightarrow{r_i} - \overrightarrow{R_k}) + \overrightarrow{F_{ext}} \tag{3.3}$$

where, η is the flux flow viscosity. The first term in the right hand side represents the inter-vortex interaction which is given by the potential

$$U^v(r) = \frac{\phi_0^2 l}{2\pi\mu_0\lambda^3}[K_0(\widetilde{r}/\lambda) - qexp(-\widetilde{r}/\xi)] \tag{3.4}$$

where, ϕ_0 is the flux quantum, l is the length of the vortex, μ_0 is the vacuum permeability, λ is the London penetration depth, ξ is the coherence length, $\widetilde{r} = (r^2 + 2\xi^2)^{1/2}$, and K_0 is the zeroth order Bessel function. The first term in eq. 3.4 represents the conventional long-range repulsion and the second term represents the short-range vortex attraction in exponential form, and the parameter q reflects the relative strength of the attraction to repulsion interactions. The second term in eq. 3.3 represents vortex pinning by parabolic potential wells, where $U^p(r) = U_0(\frac{r^2}{r_p^2} - 1)$ for $r < r_p$ or 0 otherwise. The pinning centers are randomly located at positions $\overrightarrow{R_k}$ in the simulation box. The third term of eq. 3.3; $\overrightarrow{F_{ext}} = (1/c)\overrightarrow{J} \times \phi_0\hat{z}$ is the Lorentz force experienced by the vortex due to the external current density, $\overrightarrow{J}$. In simulation, eq. 3.3 is time-integrated using 4-value Gear Predictor-Corrector algorithm [107].

We have normalized all lengths by λ_0=$\lambda(B=0)$, forces by $f_0 = (\phi_0^2 s)/(2\pi\mu_0\lambda^3)$ and time by $\eta\lambda/f_0$. We use the reduced magnetic field $b = B/B_{c2}$, and it is calculated from the

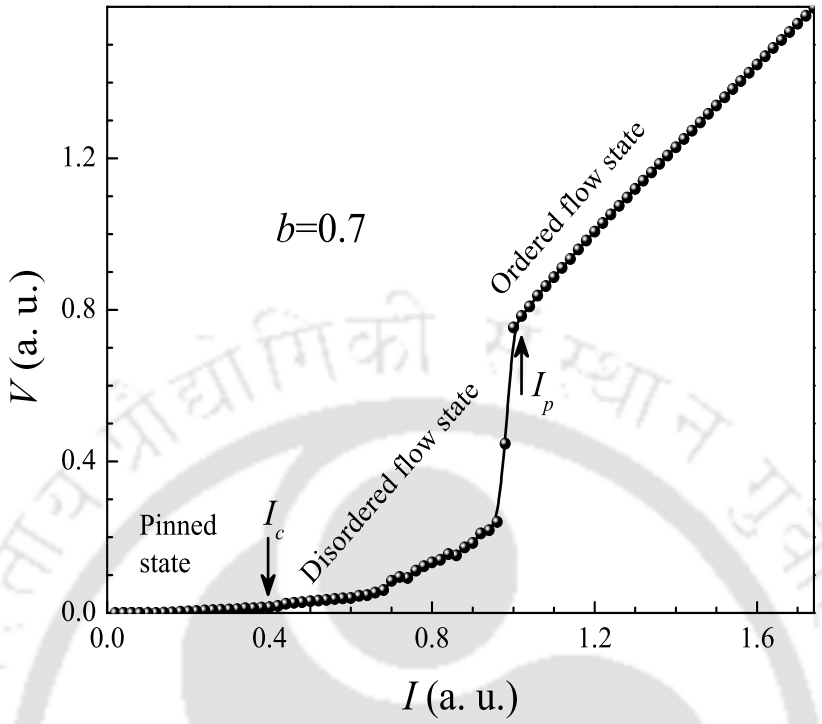

Figure 3.20: *The V(I) characteristics in arbitrary units (a. u.) of the vortex system at b = 0.7 with a pin density (n_p) = 1.82.*

lattice constant of the square lattice $a_0/\lambda_0 = (2\pi/\kappa^2 b)^{1/2}$, where κ is the Ginzburg-Landau parameter. Here, we use $\kappa \approx 13$, which is the typical value for the present $Ca_3Rh_4Sn_{13}$ single crystal. We choose N_v=1089, η=1, q=0.1 and r_p=0.05λ_0. The prefactor U_0 of the pinning potential is randomized by $\Delta \pm$ 0.01 where $\Delta = < U_0 >$. Also, we select our simulation time step, τ as 0.002. We calculated the *V(I)* characteristics, where $I \propto J_y$, and the voltage $V \propto < v_x >$.

Fig. 3.20 shows the conventional voltage vs. current (*V(I)*) curve of reduced field, b = 0.7 calculated from the MD simulation. Here, the simulation initiates with a high current value and ramp down to zero. In Fig. 3.20, three current regimes can be identified. (i) a pinned state ($I < I_c$) where all the vortices are immobile, (ii) a disordered vortex flow state (or plastic flow state) between $I_c < I < I_p$ where some vortices remain immobile and (iii) an ordered vortex flow state for $I > I_p$. Above I_p the driving force becomes dominant over

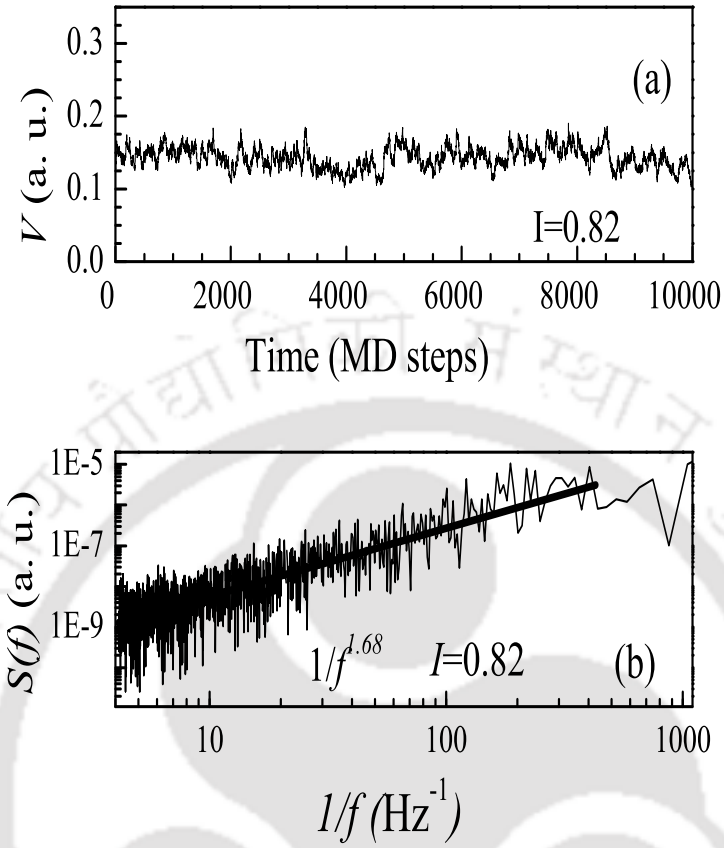

Figure 3.21: *(a) The velocity (a.u) vs. time (MD Steps) characteristics of the vortex system at b = 0.7 with a pin density (n_p) = 1.82. (b) Log-log plot of the power spectrum (S(f)) vs. 1/f at I = 0.82.*

the pinning force so the entire vortex lattice start to move in this state. Interestingly, we observe the signature of 1/*f* noise from the disordered vortex flow region. Fig. 3.21 (a) shows the average velocity of the vortices vs. time step (*V-t*) at a constant current $I = 0.82$ from the disordered flow region at $b = 0.7$. Fig. 3.21 (b) shows the power spectrum (*S(f)*) vs. 1/*f*) of the *V-t* data of $I = 0.82$. We observe a $1/f^{\alpha}$ noise spectrum with an exponent value $\alpha = 1.68$ in the disordered flow region. This implies that the self-organization of the vortices also occurs in the driven vortex system and as a result, one observes a power law correlation in the noise spectrum. Above b=0.5, we have observed the same nature of noise in the disordered flow regions.

3.10 Summary

To summarize, we have examined the loci of various features observed in dc and ac magnetization measurements in a weakly pinned single crystal of $Ca_3Rh_4Sn_{13}$ which displays both SMP and PE anomaly. We observed that an ordered vortex state can be disordered both by enhancement and lowering of temperature. With a small increment of the pinning strength, the temperature independent nature of the SMP line can be changed to one with a positive slope, resulting in the appearance of an inverse melting region in a portion of the phase diagram. The other significant result is the observation of a step change in the equilibrium magnetization across the SMP and PE regions. We observe a spinodal line for the BG/VG transition, which attests its first order nature. We also studied the spectral fluctuations in the magnetization data in various regions of the phase space. It was proved that distinct resonant frequencies are associated with the SMP and PE phenomenon. Deep inside the mixed phase $1/f^{1.8}$ nature of the spectral fluctuations were also observed.

Chapter 4

Two J_c states of $Ca_3Rh_4Sn_{13}$ single crystal

4.1 Introduction

It has been demonstrated now that most of the superconducting materials like YNi_2B_2C, V_3Si , Pb-Tl, Nb, MgB_2 etc., have various vortex lattice (VL) structure in different regions of the phase space. Changes in symmetry and orientation of the VL can arise due to several reasons such as anisotropy of the Fermi surface (FS), anisotropy of the superconducting energy gap, electronic asymmetry, crystal anisotropy effects, jamming of counter rotating VL domains etc. [108–113]. Various VL structures have been recorded by both local measurements like scanning tunneling microscopy (STM) and bulk measurements like small angle neutron scattering (SANS). It has been of great interest to study the dynamics of these vortex lattices when they are perturbed from equilibrium. During such dynamics there are various characteristic time scales which affects the motions of these VLs. The VL structures or orientations of the VL with respect to the direction of motion of vortices affect the characteristic time. Below and above this characteristic time scales certain VL structures/orientations are favored. Normally the current vs. voltage (*V(I)*) measurements are an important tool to

understand the dynamics of these VLs. Evidences of two depinning currents in YNi_2B_2C has been linked to two different types of VL structures [35]. This means that there is a velocity induced reorientation/change of the VL structure. In fact Okuma *et al.* [36], have proved that there is a characteristic time scale ($\sim$10 ns) where the driven VL structure changes from one orientation to another in MgGe thin films. Hence, metastability effects of various VL structures is an important area of investigation in transport measurements. Recently, evidences of well ordered metastable states of VLs has been found in MgB_2 through SANS experiments [34, 113]. These metastable states differ from the ground state only by a certain degree of rotation and these metastable states can be reverted to the ground state by a small change in the applied magnetic field. It is worth to mention that the characteristic time scales for various materials in different metastable states ranges from nano seconds to 100 seconds.

The SANS measurements in a previously studied $Ca_3Rh_4Sn_{13}$ single crystal revealed the co-existence of rhombic and square VL phases [114]. Therefore, chances of the existence of metastable states are very likely in theses crystals and this may lead to different magnetization/J_c at different characteristic time scales. In this chapter we report the observation of two J_c states through the isothermal dc magnetization measurements in $Ca_3Rh_4Sn_{13}$ single crystal.

4.2 Sweep and stable field mode magnetization measurements

In S-VSM one can measure the magnetization vs. magnetic field (M-H) either in sweep field mode or in stable field mode. In sweep field mode the applied magnetic field will change continuously and the magnetization is recorded simultaneously, but in stable field mode first the magnetic field is stabilized to a certain value and then the magnetization of the sample

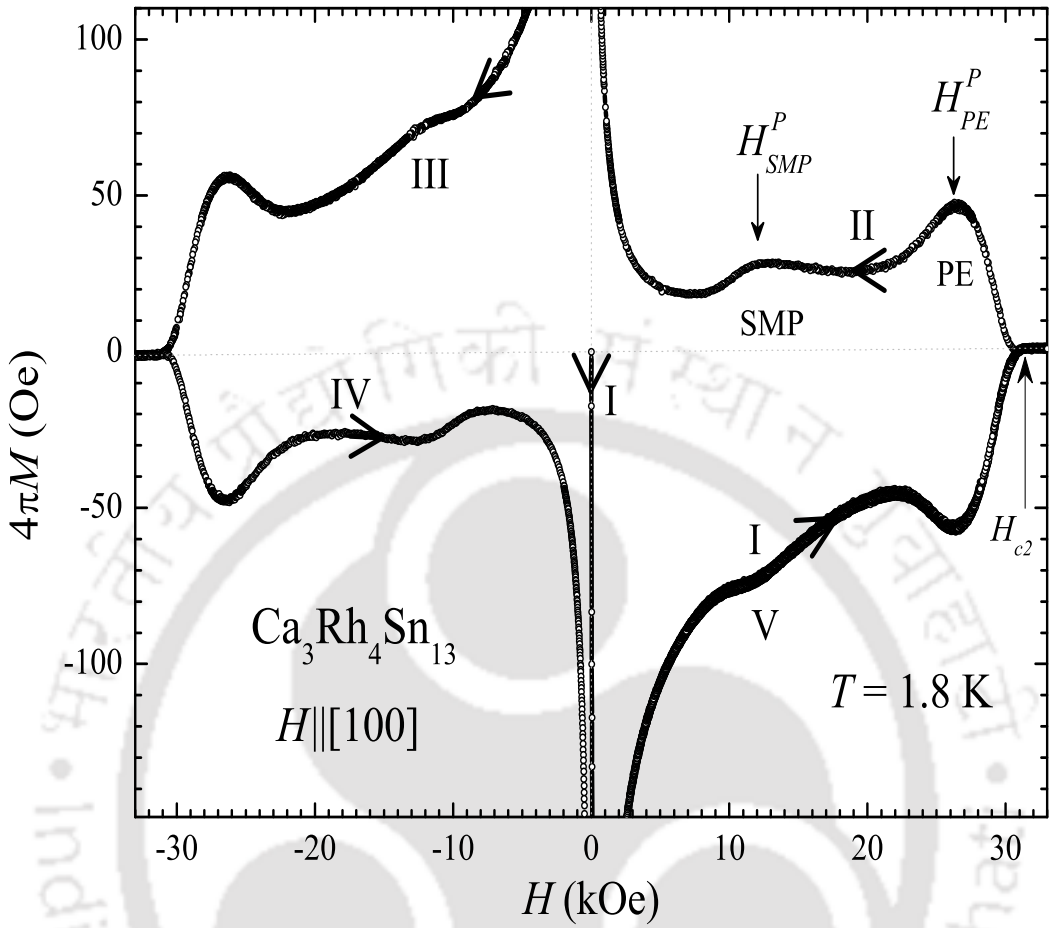

Figure 4.1: *Five quadrant M-H loop of $Ca_3Rh_4Sn_{13}$ single crystal at T = 1.8 K recorded by the sweep field mode technique. The two modulations in the magnetization curves are identified as SMP and PE.*

is recorded after a delay of 1 Sec. In this chapter the measurements are carried out with a magnetic field sweep rate of 10 Oe/Sec. The applied dc magnetic field (coaxial with the ac field) was kept parallel to the [100] axis of the cubic crystal.

Fig.4.1 shows the five quadrant isothermal magnetization hysteresis loop of $Ca_3Rh_4Sn_{13}$ at constant temperature (T=1.8 K), recorded in the sweep field mode method by sweeping the field at a rate of 10 Oe/sec. The first and second modulations in the M-H loops are denoted as second magnetization peak (SMP) and peak effect (PE), respectively. The peak positions (maxima) of the SMP and PE are marked as H^p_{SMP} and H^p_{PE}. The mixed phase

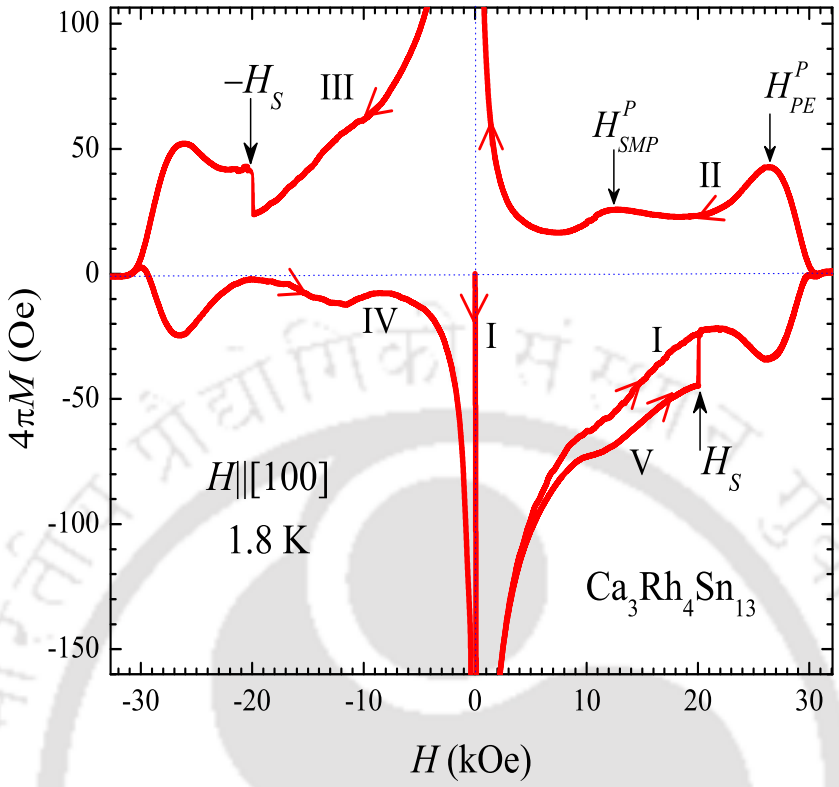

Figure 4.2: *Five quadrant M-H loop of $Ca_3Rh_4Sn_{13}$ single crystal at T = 1.8 K recorded in the stable field mode technique. The sudden magnetization shift observed in the third (III) and fifth (V) quadrants are denoted as -H_S and H_S, respectively.*

ends at the upper critical field, H_{c2}. Here, the virgin (I) and fifth (V) quadrant magnetization curves overlap together from very low magnetic fields and continue like a single curve till H_{c2}. It is evident from the figure that the negative field side magnetization curve (ie. third (III) and fourth (IV) quadrant) are mirror images of the positive field side (i.e. second (II) and fifth (V) quadrant) magnetization curves. Hence, multiplication of the magnetization data with negative one (-1) for the negative field region should produce the magnetization data for the positive field region and vice versa. As per the prescription of Bean's critical state model [20], width of the magnetization hysteresis loop is directly proportional to the critical current density, J_c. Therefore, in sweep field mode, both positive and negative

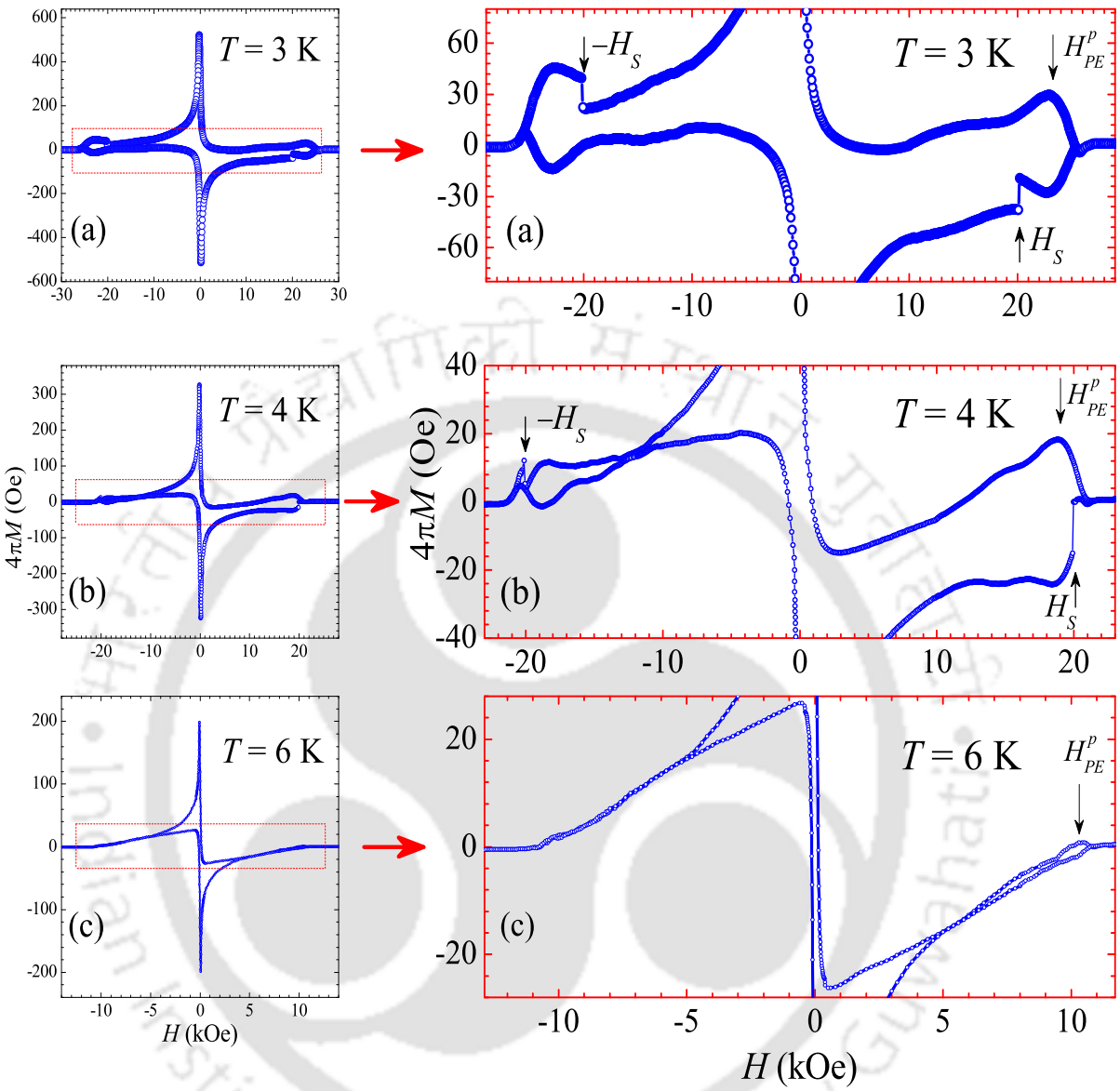

Figure 4.3: *Plots of the stable field mode magnetic hysteresis loops of $Ca_3Rh_4Sn_{13}$ single crystal at constant temperatures (a) T=3 K, (b) T=4 K, and (c) T=6 K. Right hand side M-H loops are the expanded portions of the rectangular region of the left hand side M-H loops.*

quadrants have the same J_c value. Further the values of H^p_{SMP} and H^p_{PE} for the positive and negative quadrants are also exactly identical.

Fig. 4.2 shows the five quadrant *M-H* loop at a constant temperature of 1.8 K recorded by the stable field mode technique. Here, the virgin (I) forward and reverse (II) magnetization curves show the normal behavior. However, in the third (III) quadrant, a sudden anomalous

increase in magnetization at ≈ -20.1 kOe is observed and is denoted as -H_S. The fourth (IV) quadrant also shows the normal behavior, however in the fifth (V) quadrant a sharp decrease in the magnetization occurs at ≈ 20.1 kOe and is marked by H_S in the figure. Note the anomalous change in the magnetization in the third (III) and fifth (V) quadrants occur exactly at the same magnitude of the applied magnetic field. It is interesting to note that the virgin (I) curve and the fifth (V) quadrant do not overlap till H_S, above which the curves are identical. As it is well known that the width of the magnetization hysteresis loop is directly proportional to J_c so it can be interpreted that there is a change in the value of J_c at $\mp H_S$. It is worth mentioning that the onset and peak field points for the SMP and PE anomalies are identical to that of the sweep field mode magnetization data.

To further confirm the anomalous behavior at $\mp H_S$ in Fig. 4.2, we have recorded the dc magnetization hysteresis loops at different temperatures in the stable field mode. Fig. 4.3(a), (b) and (c) show the *M-H* loops at 3 K, 4 k and 6 K without the virgin (I) curve. We found that every magnetization loops upto 4 K have an upward (downward) shift in their third (III) (fifth (V)) quadrant at the same magnitude of H_S. It is worthwhile to mention that above 4 K the superconductor becomes normal at 19 kOe which is below H_S ($\sim$ 20.1 kOe) . Therefore, no shift in magnetization is observed in *M-H* at 6 K (Fig. 4.3(c)). However, at 6 K, the asymmetry of the *M-H* loop still persists or in other words the *M-H* loop of the positive field region is not the mirror image of the negative field region. In the positive field region the PE can be observed distinctly (marked by arrow in the panel (c) for Fig. 4.2), whereas the bubble in the PE region for the negative side *M-H* loop is absent. This asymmetry indicates the existence of two J_c states possibly in different vortex configurations for the same magnitude of H and T.

The magnetization shifts in the third (III) and fifth (V) quadrants in the magnetization curves are quite unusual. As mentioned earlier, in the fifth (V) quadrant magnetization curve of Fig. 4.2, the high J_c state is suddenly reduced to a low J_c state at H_S but in the third (III)

quadrant, the low J_c state is suddenly increased to a high J_c state at -H_S. So, the shift in the magnetization curves make an increase as well as a decrease in the magnetization value and is contrary to the flux jumps reported in literature (Ref.[115]).

4.2.1 Observation of two J_c states

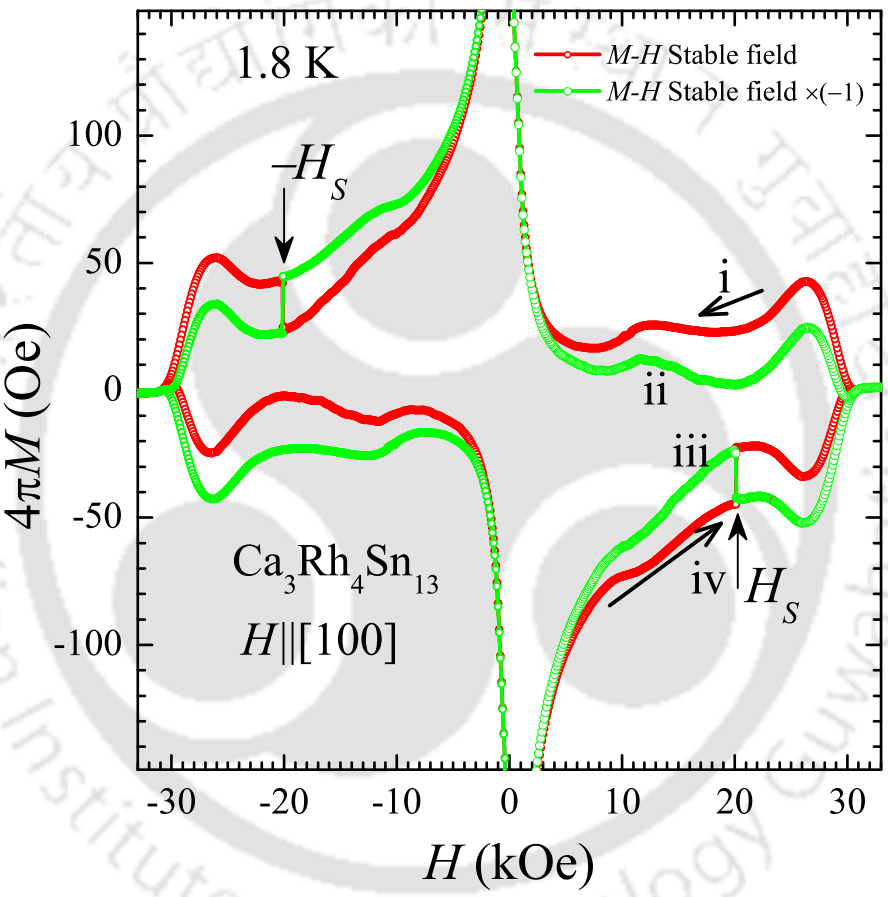

Figure 4.4: *Stable field mode M-H loop at 1.8 K without the virgin curve (red color). We multiplied the same M-H loop with negative one (-1) and the resultant loop is shown in green color.*

Fig. 4.4 shows the stable field mode *M-H* loop at 1.8 K (red curve) without the virgin curve and we inserted the same *M-H* loop multiplied with negative one (-1) which is pictured as a green color *M-H* loop. Interestingly, the *M-H* curves are perfectly joined in the shift points and act as two separate hysteresis loops in the positive and negative field sides. It is a

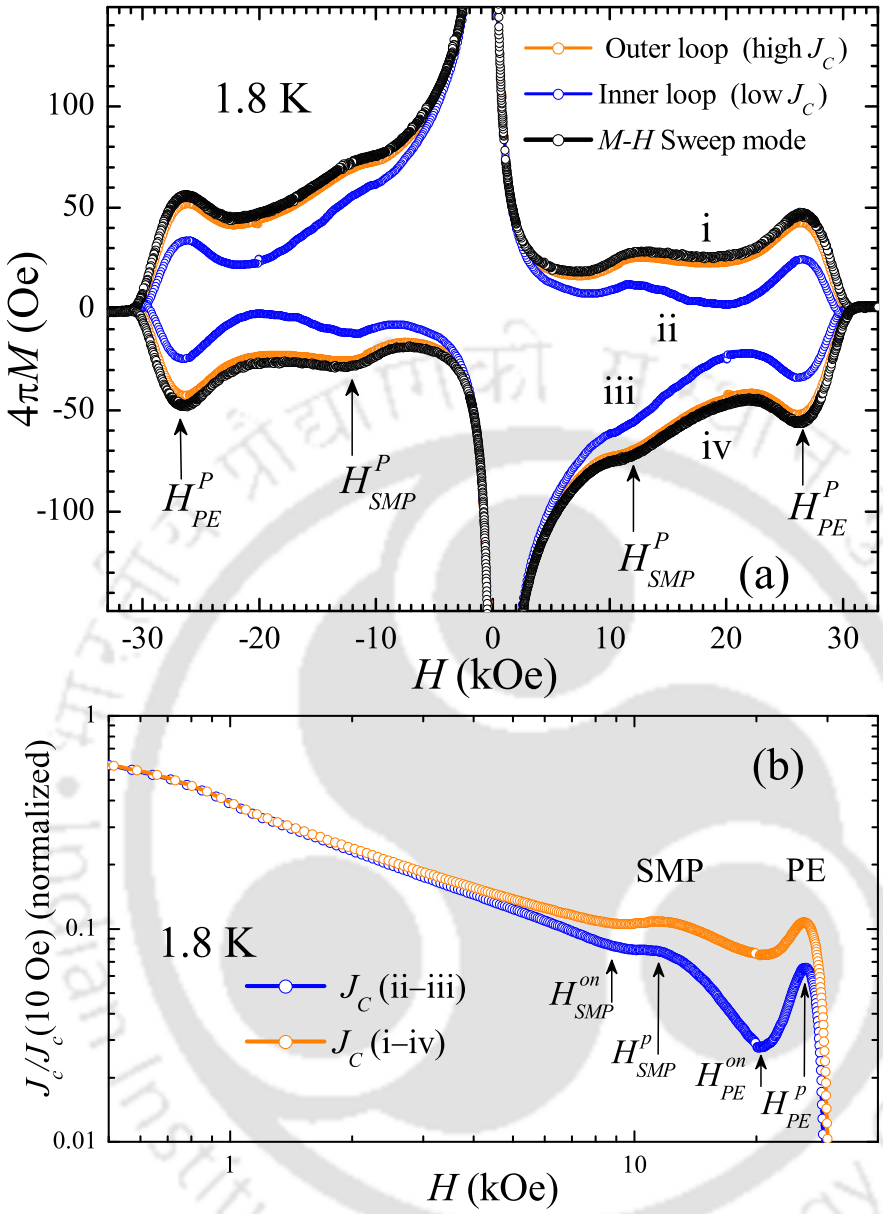

Figure 4.5: *(a) shows the outer curves i and iv as orange color M-H loop and the inner curves ii and iii as blue color M-H loop. The sweep field mode M-H loop is also shown as a Black color M-H loop. (b) shows the log-log plots of the positive field side J_c which is obtained by considering the curves ii, iii (blue color curve) and i, iv (orange color curve).*

clear indication that the plots are related and establishes the notion of two J_c's in the sample. To distinguish easily, we renamed the positive side curves as i, ii, iii and iv as shown in the Fig. 4.4. Now we plot the outermost curves as an orange color loop and the innermost curves as a blue color loop (Fig. 4.5(a)) from both the positive and negative field regions

and find that the system is totally symmetric. It gives an indication that two J_c states do exist independently. We inserted the sweep field mode *M-H loop* (black color loop) in Fig. 4.5(a) and it depicts that the sweep field mode data exactly overlaps with the outermost orange color loop. For focusing on the different J_c states of the material we contemplate the curves i and iv as one *M-H* loop, for the high J_c state, and the curves ii and iii as another *M-H* loop, for the low J_c state.

So this way of construction gives us two different loop widths of *M-H* at 1.8 K and the loops belong to two different J_c states. Fig. 4.5(b) contains the two J_c plots of *M-H* at 1.8 K where the orange color curve is calculated from the *M-H* loop of curves i and iv and the blue curve is calculated from the *M-H* loop of curves ii and iii. In Fig. 4.5(b) the modulations in the J_c are due to the SMP and PE anomalies. The onset and the maximum (marked by arrows in the figure) of these anomalies occur at the same applied field for both the J_c states. It is worth to mention here that the curve for the high J_c coincides with that of the J_c curve of the sweep field mode data.

The field ramping by the stable field method may provide sufficient time to relax and reorganize the vortices. Recent SANS experiments in MgB_2 by Rastovski *et al.* [34, 113], have shown that the metastable vortex lattice domains persist in the presence of substantial vortex motion and demonstrated that the observed metastability is not due to vortex pinning. Instead, they proposed that it is due to the jamming of counterrotated vortex lattice domains which prevents a rotation to the ground state orientation. So, in our case the high J_c state is probably due to the high metastability of the underlined VL structure configurations. Hence, it is clear that the sweep field mode measurements in $Ca_3Rh_4Sn_{13}$ probe only one metastable VL configurations and on the other hand, in stable field mode measurements, the longevity is such that one can probe a metastable high J_c state and a low J_c state, simultaneously. However these are only speculations.

Now the question to be addressed here is to explore the metastability effects of these two J_c states, or in other words whether it is possible to access the J_c states by creating the vortex lattice in a different way than the conventional way of the *M-H* loop. For this purpose we employ two different standard magnetization measurement techniques such as (a) field cooled (FC) minor curves and (b) time relaxed magnetization curves.

4.3 Different ways of obtaining the two J_c states

4.3.1 (a) Field cooled (FC) minor curves

The field cooled (FC) minor curves usually corroborate the history dependance in J_c. Such a procedure was used to trap various metastable states of the vortex lattice which was otherwise impossible to explore in a normal magnetization hysteresis loop. Using this procedure it was shown that a vortex lattices (or J_c) have histories of thermodynamic paths that they have traversed. Here we present results of the thermomagnetic path dependence of J_c by studying the features of the minor hysteresis curves with respect to the envelope hysteresis loop. Fig.4.6(a) shows the forward FC minor (blue) curves plotted in the positive quadrant of the 1.8 K hysteresis loops. The first (i) and forth (iv) quadrant of the *M-H* loop correspond to the high J_c state. The second (ii) and third (iii) curves of the *M-H* loop for the low J_c state. We field cooled the sample at 1.8 K at a field ($< H_S$) and then ramp the field in the forward direction. The forward FC curves first shoot down and afterwards merges with the third (iii) curve of the *M-H* loop. The overshooting of the FC minor curves are well studied in literature [11]. However the FC minor curves saturated for the curve number iii, which corresponds to the low J_c state. Such an event can be explained with the choice of thermodynamic path dependence while creating the vortex lattice. The path was chosen such that the features of the low J_c state have been trapped in the vortex lattice, which resulted in the *M-H* loop taking such a path. Similar procedure of FC minor loops were followed

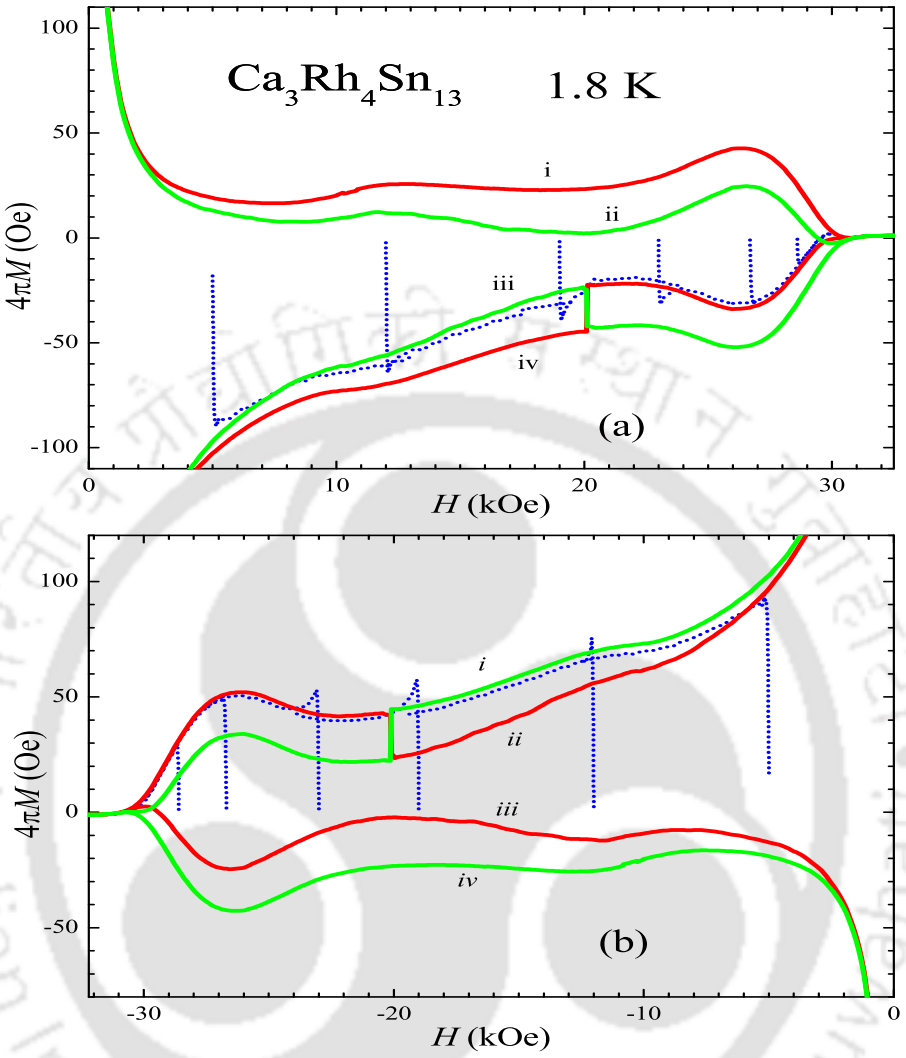

Figure 4.6: *(a) positive field side and (b) negative field side M-H loop at 1.8 K (cf. Fig. 4.4) with field cooled (FC) minor hysteresis curves (blue dotted curves) starting from different field points at 1.8 K.*

in the negative field region. The sample was field cooled at 1.8 K with a negative applied field whose magnitude was less than that of H_S. Then the field was ramped towards -H_{c2}. It was found that this state stabilizes to the high J_c state. Hence this procedure traps the high J_c state compared to the normal *M-H* loops which settles down to low J_c state in the negative field region. Hence this entire exercise of thermodynamic path dependence allows

us to choose whether the vortex lattice will stabilize to low J_c state or high J_c state. Hence, the existence of the new J_c states in both the positive and negative fields is justified in this $Ca_3Rh_4Sn_{13}$ single crystal.

4.3.2 (b) Time relaxed magnetization curve

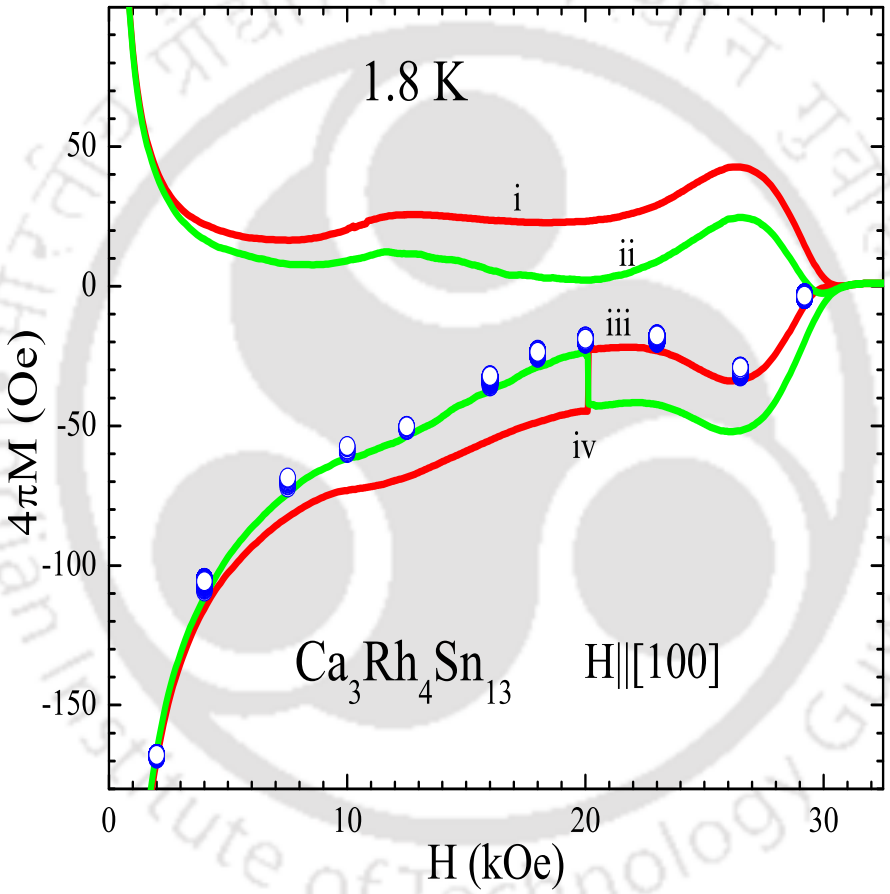

Figure 4.7: *Partial portion of the M-H loop at 1.8 K (cf. Fig. 4.4) with end data points of the time relaxed magnetization (denoted with the blue circles).*

Once again the positive field side of Fig. 4.4 is shown in Fig. 4.7 as red and green curves. We have measured the magnetization relaxation data at particular field points at 1.8 K. The end points of the magnetization relaxation data are plotted inside the *M-H* curve as blue

circles in Fig. 4.7. Interestingly, we note that the magnetization relaxation data coincide with the third (iii) curve which corresponds to the low J_c state. Hence, the time relaxed *M-H* curves successfully achieved the low J_c state in the $Ca_3Rh_4Sn_{13}$ single crystal.

4.4 Discussion of two J_c states using Bean's critical state model

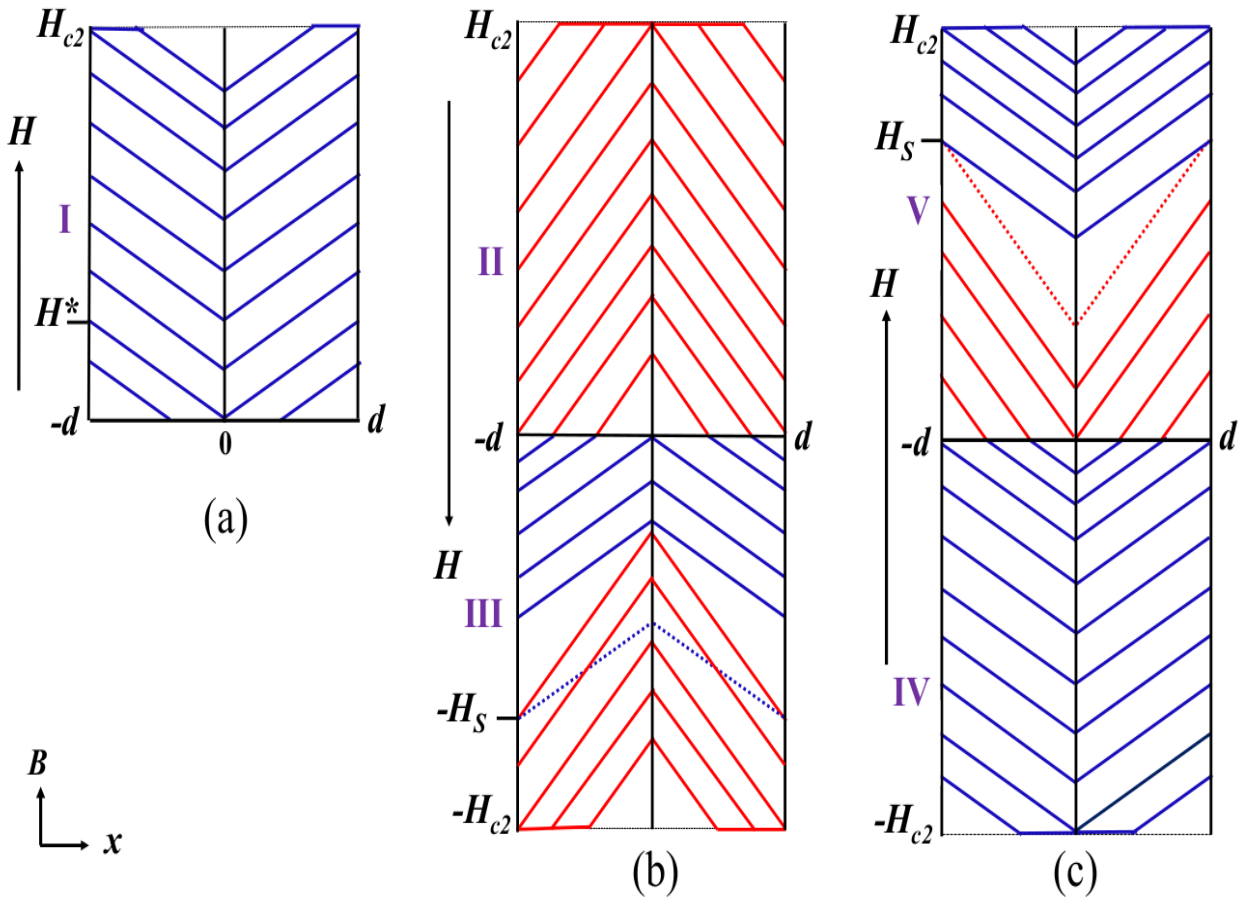

Figure 4.8: *Beans profile (B-x) of the stable field mode M-H at 1.8 K (cf. Fig. 4.2). (a) Beans profile corresponds to the first (I) quadrant. (b) Beans profile corresponding to second (II) and third (III) quadrants. (c) Beans profile corresponding to forth (IV) and fifth (V) quadrants. The blue and red color B-x profiles correspond to the low and high J_c states, respectively. The dotted lines represent the B-x profile (value of J_c) that would have happened if there was no shift at $\mp H_S$. Pictures are not drawn to scale.*

Now we attempt to relate the hysteresis behavior of the type – II superconductors to the critical current density, J_c with the help of Bean's critical state model [20]. To understand the changes in magnetization, field profiles of the *M-H* at 1.8 K data are explained below with the help of Bean's critical state model (Fig. 4.8).

The Bean's profiles, *B-x*, are plots of the local macroscopic field, *B*, versus distance, *x*, from the center of the sample. Fig. 4.8 shows five quadrant Bean's profile representation for an infinite slab of thickness $2d$ with surface at $x=\pm d$ and the applied magnetic field, *H* being parallel to the surface. According to this model, at any point in the sample, the current flowing can have value J_c or zero. When a magnetic field, H ($H > H_{c1}$) is applied to a type – II superconductor, it penetrates the sample with a slope of $\pm\mu_0 J_c$ ($dB/dx = \pm\mu_0 J_c$ for slab). Fig. 4.8(a) is the Bean's profile equivalent to the first (I) quadrant of Fig. 4.2. While increasing the external field, the flux enters the sample from the edges and then moves deeper inside. With a further increase in magnetic field, more and more parts of the sample experience the field. At H^*, the entire sample experiences the field and hence the field, H^* is known as the full penetration field. The slope (dB/dx) becomes zero when the macroscopic field occupies fully inside the sample at upper critical field, H_{c2}.

We have observed from Fig. 4.3(c) that it does not have the shift in magnetization at H_S, the positive field range has larger magnetization hysteresis width than that of the negative field region. This provides us a clue that the entire negative field region (below $-H^*$) has a lower value of J_c than that of the positive field region (above H^*). We speculate that such a choice of J_c in the different directions of the magnetic field may be related with the intrinsic arrangements of the pinning sites of the crystal rather than being a spontaneously broken one.

In the second (II) quadrant (Fig. 4.8(b)), as the external field start to reduce from H_{c2}, the vortices starts to exit through the edges of the sample. As the choice of the J_c in the positive field region is the higher J_c, so the slope *B-x* profiles in Fig. 4.8(b) is drawn accordingly

(red color slopes). As the field crosses zero towards the negative field region (third (III) quadrant) antivortices starts appearing. But the choice of the J_c in the negative field region is lower compared to that of the positive field region and hence the slopes (blue color *B-x* slopes) have been changed accordingly. What happens at -H_S is not easily comprehensible. But the internal perturbations cause the state to go to higher J_c beyond this applied magnetic field, -H_S. Hence, the slopes of the Bean's profile, *B-x* (red color) are changed accordingly. But one thing that may happen at $\mp H_S$ is that a shift has occurred among the energy scales (pining energy with intervortex elastic energy) which have resulted the change of J_c.

In the fourth (IV) quadrant, (Fig. 4.8(c)) where the field is reversed from -H_{c2} to zero, the vortices start to exit the sample. As the choice of the J_c in the negative field region is the lower J_c, hence the slope in *B-x* profile (blue color) is drawn accordingly in Fig. 4.8(c). In the fifth (V) quadrant, where the field crosses zero from the negative side to the positive side we observe a situation similar to the third (III) quadrant. Here also we observe an increase in the values of J_c (red color *B-x* slopes), as the choice in the positive field region is the higher value of J_c. Once the field reaches H_S the internal rearrangement of the energy scales forces the system to go to the low J_c state (blue color slopes). Hence the *B-x* profiles are changed accordingly.

In case of the virgin (I) *M-H* curve, the applied field starts form zero. So, there is no possibility of a vortex antivortex configuration to be generated. Hence the situation is completely different from that of the fifth (V) quadrant. So it goes to the low J_c state and the profiles of *B-x* (blue color slopes) is drawn as shown in Fig. 4.8(a).

For quenched random disorder, the effective pinning at any point of the flux line lattice would be proportional to the fluctuation in the density of pins at that point. In an isothermal magnetization measurement, there is no chance of change in the pinning conditions. As we know, changes in correlation volume, V_c make changes in J_c [18, 19, 69]. So, the possibility

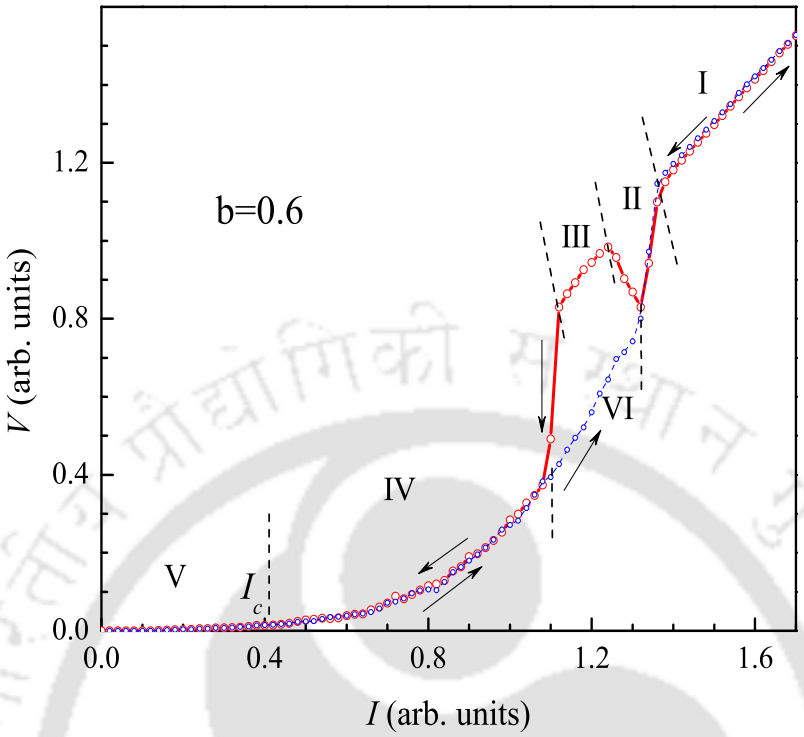

Figure 4.9: *The voltage-current (V(I)) characteristics of the vortex system with b=0.6, Δ= 0.005 and a pin density n_p =1.90. The blue and red curves correspond to the forward and reverse direction V(I) and the dashed lines separate six different vortex flow regions.*

of two J_c states may be due to two different vortex lattice structures because different vortex lattice structures have different elastic constants which change the value of J_c.

4.5 Zero temperature molecular dynamics simulation

Here similar molecular dynamics simulation procedure is employed from section 3.9. Here also we choose N_v=1089, η=1, q=0.1, κ=13 (typical value for the present $Ca_3Rh_4Sn_{13}$ single crystal) and r_p=0.05λ_0. The prefactor U_0 of the pinning potential is randomized by $\Delta\pm$ 0.01 where $\Delta =< U_0 >$. Also, we select our simulation time step, τ as 0.002.

In our simulation, we observed kinks in the *V(I)* characteristics in a small field window from *b*=0.575 to 0.66 and one such *V(I)* curve at *b*=0.60 is shown in Fig. 4.9 . Here, the simulation initiates with a high current value and ramp down to zero (red curve) and

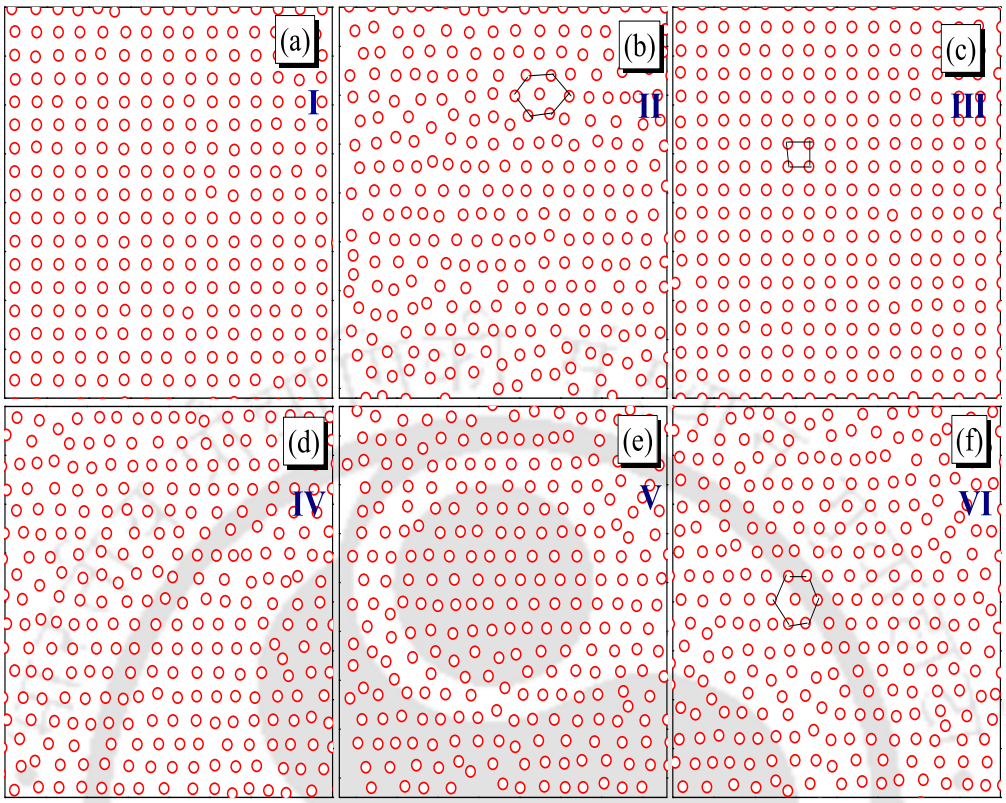

Figure 4.10: *Real space distribution of vortices in six regions of the V(I) characteristics at b=0.6.*

once the current reached zero, we ramp back the current to a high value (blue curve). One can see a noticeable hysteresis in the *V(I)* which initiated from the current value where the kink appears. In Fig. 4.9, I and III are the linearly progressing regions, II is the region where the kink appears, IV and VI are the disordered vortex flow regions. Vortices are almost immobile below the critical current (I_c) and this region is marked as V. It is observed from the *V(I)* characteristics that the kink appears only when the current ramped down (red curve). We also observed that region III has the same current values as region VI but the corresponding voltages are different.

Snapshots of the vortex positions from the six different regions of the *V(I)* curve at *b*=0.60 is plotted in Fig. 4.10. The six regions have current values 1.48 (I), 1.30 (II), 1.20 (III), 0.90 (IV), 0.24 (V) and 1.20 (VI), respectively. The appearance of the ordered square

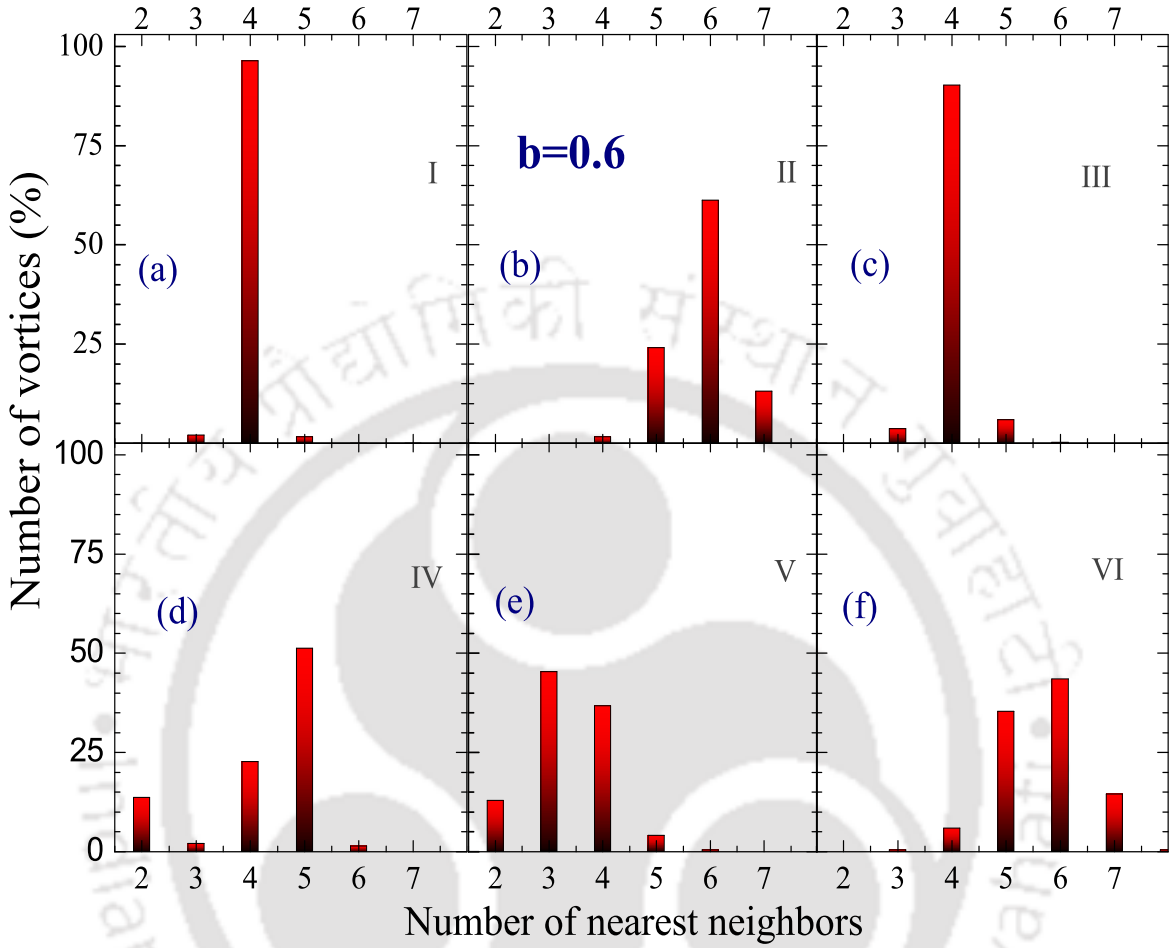

Figure 4.11: *The number of nearest neighbors of the vortices in six different regions at b=0.6.*

vortex lattice in I and III (Fig. 4.10(a) and 4.10(c)) confirms the steady state vortex flow in these regions. The disordered configurations of vortices are observed in the remaining four regions (II, IV, V and VI). It is interesting to mention here that the current values in the regions III and VI are same but the vortex configurations are different.

For getting a quantitative idea about the vortex lattice structure, we have calculated the number of nearest neighbors (NNN) in each region of the *V(I)* at b=0.6 and plotted it in Fig. 4.11. In the ordered flow regime, I and III (Fig. 4.11(a) and (c)) maximum number of

vortices have a NNN value 4 as expected. Majority of the vortices in region II (Fig. 4.11(b)) having NNN values 5,6 and 7 inferred that a section of the square lattice from the region I is changed to hexagonal like lattice structure in the kink area. The disordered vortices of region II again transformed into an ordered square lattice as shown in Fig. 4.11(c).

It is obvious here that the same current in region III and VI show different voltages as a consequence of different vortex lattice structures, i.e., here the ramping directions of the current affecting the structure of the vortex lattice. The region III is obtained from current ramp down and have high voltages while the region VI is obtained from current ramp up with low voltages. This seems to have the same type of phenomenon as compared to the experimentally observed asymmetric *M-H* loops in Fig. 4.3, where the positive field side magnetization curve has a high J_c while the negative field side *M-H* has a low J_c.

4.6 Summary

We have performed the isothermal dc magnetization measurements in an isotropic cubic single crystal of $Ca_3Rh_4Sn_{13}$ in two different methods; *i.e.*, sweep field mode and stable field mode. During the measurements we have observed that the sweep field mode *M-H* data show high critical current densities due to the underlying metastable vortex lattice configurations. The stable field mode magnetization data revealed the existence of a new low critical current density state along with the high critical current density state. Further we probed the two critical current densities via two different measurement methods such as field cooled minor curves and time relaxed magnetization curves.

Chapter 5

Positive magnetization in $Ca_3Rh_4Sn_{13}$ single crystal

5.1 Introduction

The diamagnetic Meissner effect (DME) is the phenomenon of the expulsion of magnetic flux from a superconductor during its transition to the superconducting state, is one of the crucial property of a superconductor. On the contrary to DME, one another phenomenon known as the paramagnetic meissner effect (PME), or Wohlleben effect, in which the field-cooled (FC) magnetization of some of the high and low temperature superconducting samples is paramagnetic below the transition temperature T_c, has been reported several times in the literature [3, 37–41]. This anomalous paramagnetic effect has been interpreted in the framework of various models such as Josephson junctions, spontaneous supercurrents due to vortex fluctuations and d-wave superconductivity etc [80, 116–118]. However, the discovery of such effects in conventional superconductors like Nb and Al indicated that the origin of PME might be less exotic [3, 119]. Recent studies pointed out that this phenomenon may arise due to flux trapping on field cooling and its subsequent compression [40, 83]. However, Zharkov [42] revealed that if supercurrents flow in different directions in a material

then according to Ginzburg–Landau (GL) theory the material can show positive or negative magnetization. The investigations further revealed that various metastable states having positive and negative magnetization do exist in such a model. Under certain conditions the energy difference between the ground state and these metastable states is minimal. Hence, it may be convenient to access these states experimentally.

Recent studies in a weakly pinned $Ca_3Rh_4Sn_{13}$ single crystal have shown the appearance of positive magnetization on field cooling (PMFC) the sample at low applied magnetic fields [40]. In this chapter, we mainly focussed on the isofield dc magnetization measurements in $Ca_3Rh_4Sn_{13}$ single crystal. After that we investigated the metastable vortex states at the onset of the surface superconductivity and the possible ways of transitions across these metastable states. We have also studied the surface superconductivity effects in $Ca_3Rh_4Sn_{13}$ single crystal.

5.2 Positive magnetization on field cooling in $Ca_3Rh_4Sn_{13}$ single crystal

Fig. 5.1 shows the temperature dependence of the field-cooled cool-down magnetization ($M_{FCC}(T)$) curves normalized with the value of magnetization at 1.7 K (M_{FCC}(1.7 K)) under different applied magnetic fields. Precautions have been taken so that the remanent field in superconducting magnet does not affect the results. In the SQUID–VSM, we set the amplitude of vibration of the sample – the vibration amplitude, (a_v) as 1 mm. Inset of Fig. 5.1 shows the enlarged view of the rectangular portion where one can notice the PMFC modulations of the $M_{FCC}(T)$. After the PMFC modulation once again the sign of the magnetization changes and the sample becomes diamagnetic and this is due to the surface superconductivity effects. The end point of surface superconductivity region is marked by T_{c3} by a procedure prescribed elsewhere [3]. This is the first observation of surface su-

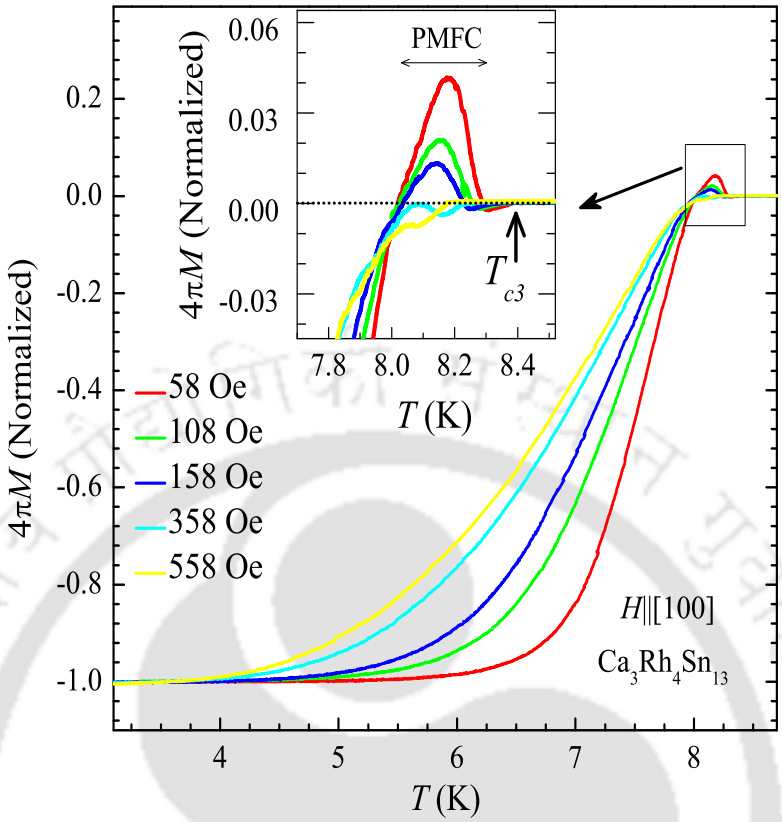

Figure 5.1: *Normalized field-cooled cool-down magnetization curves (normalized with the value of magnetization at 1.7 K) at various low magnetic fields, H = 58 Oe, 108 Oe, 158 Oe, 358 Oe and 558 Oe. The inset shows the expanded portion of the rectangular region which highlights the PMFC region.*

perconductivity in $Ca_3Rh_4Sn_{13}$ single crystals. The arrow in the inset shows the T_{c3} point of the $M_{FCC}(T)$ curve of an applied field, H = 58 Oe. As the applied magnetic field increases, in small steps, the magnitude of peak of PMFC decreases in the $M_{FCC}(T)$ curves and almost vanishes around 358 Oe. Above this applied magnetic field the sample is always diamagnetic below T_{c3} as should be the behavior of a conventional superconductor.

5.2.1 Vibration amplitude (a_v) dependence of PMFC

Now it will be worthwhile to investigate this anomalous paramagnetic feature in the $M_{FCC}(T)$ curve under different sets of experimental conditions. The field inhomogeneity experienced

by the sample over a scan length of 2.8 mm is found to be negligibly small. Hence, it would be interesting to record the $M_{FCC}(T)$ by varying vibrational amplitude (a_v) for fixed magnetic field, H. Fig. 5.2 demonstrates the plot of $M_{FCC}(T)$ curves at 80 Oe with a_v values 0.5 mm, 1 mm, 2 mm and 5 mm. For the smallest amplitude of vibration, 0.5 mm $M_{FCC}(T)$ curve shows paramagnetic peak as is displayed in the inset of Fig. 5.2. While for an a_v of 2 mm $M_{FCC}(T)$ curve remained always diamagnetic through out the entire temperature range as is shown clearly in inset of Fig. 5.2. It is worth mentioning that all the $M_{FCC}(T)$ curves recorded under different amplitudes of vibration merges around 7.9 K denoted as T^* in Fig. 5.2. Below this temperature, T^*, all the $M_{FCC}(T)$ curves merge together and become a single curve. Even below T_{c3} and the onset of the PMFC region (marked by T_{pon} in the inset of Fig. 5.2) the curves do not split considerably. Hence the metastability features in the PMFC region is accessible with the changes in the amplitude of vibration.

5.2.2 Switching of magnetization in the PMFC region

We have explored the extent to which these metastable states are stable by performing magnetization vs. time measurements. We also have demonstrated the effect of switching from one a_v to another and its memory effects during switching. All the panels of Fig. 5.3 depict the robustness of changes in magnetization with that of time due to the changes in the value of a_v at fixed values of applied field and temperature in the PMFC region. The change in the value of magnetization is instantaneous and the magnitude of the magnetization does not changes even after 1800 sec. The panel (a) shows a single step when the value of a_v is changed from 0.5 mm to 1 mm. The panel (b) shows two steps when the value of a_v changes from 0.5 mm to 2 mm with an intermediate step of 1 mm. The panel (c) displays not only the switching but also displays when the value of a_v is reverted to 0.5 mm from 2 mm via 1 mm. It is worth to mention that in this constant field and temperature the sign of magnetization changes from positive to negative when the value of a_v changes from 0.5

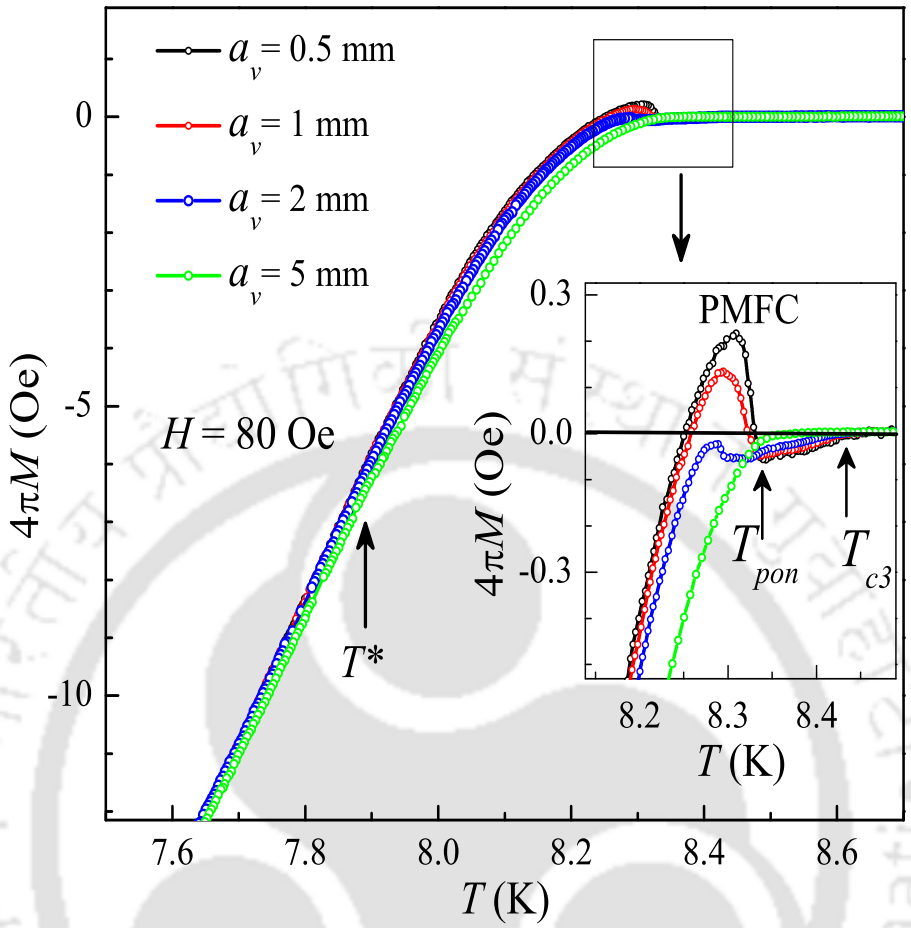

Figure 5.2: *$M_{FCC}(T)$ curves of H = 80 Oe with various vibration amplitudes (a_v). Magnetization values are different in between T^* and T_{c3}. The inset shows the expanded portion of the rectangular region of the main panel.*

mm to 2 mm. So the sample can switched from the paramagnetic state to the diamagnetic state and reverted back. So the bistability of memory device with respect to the sign of the magnetization in addition to the multistability of the memory device with respect to the magnitude of the magnetization is well accounted in this figure. Further it is important to note that there is no relaxation of the magnitude of magnetization which remains constant in time. The noise level was observed to increase with the decrease in the value of a_v.

Further we report here the thermal stability of this device, which is shown in the two panels of Fig. 5.4. The panel (a) shows the $M_{FCC}(T)$ curves at a constant applied field of 55

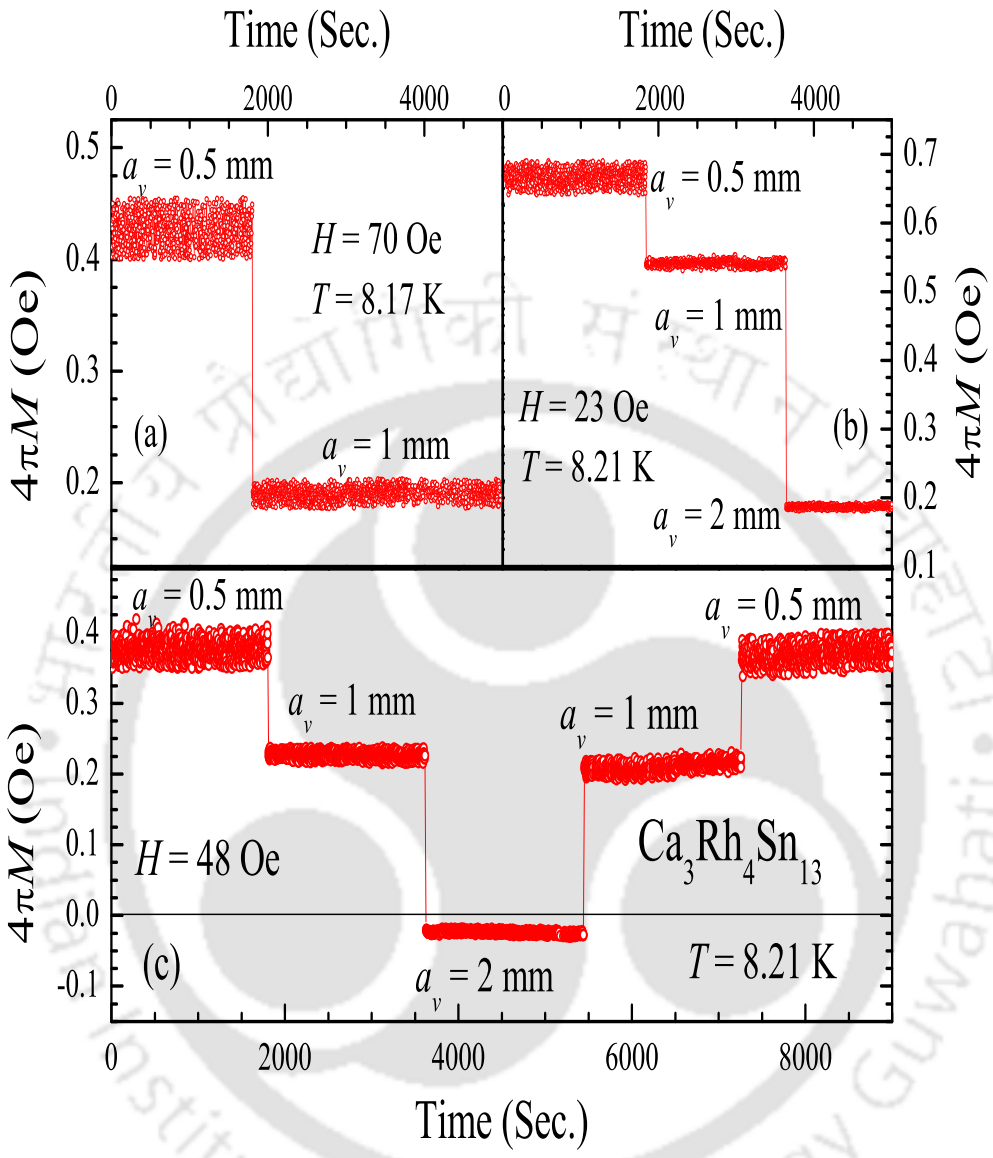

Figure 5.3: *Magnetization vs. time plots with different a_v selected from the PMFC region of constant H and T. (a) H = 70 Oe and T = 8.17 K (b) H = 23 Oe and T = 8.21 K (c) H = 48 Oe and T = 8.21 K. We have changed a_v in a time interval of 1800 seconds (30 minutes) everywhere.*

Oe for two values of a_v, 0.5 mm (red curve) and 1 mm (black curve). To check the thermal stability of the device we changed the values of a_v while recording the $M_{FCC}(T)$ data. So the blue $M_{FCC}(T)$ curve is a result depicted from this experiment. The data for the blue $M_{FCC}(T)$ curve was recorded with a value of a_v = 0.5 mm till 8.25 K where it is observed

to follow the usual path of the red curve. Then suddenly the value of a_v was changed to 1 mm and then $M_{FCC}(T)$ data was recorded. It was found that the $M_{FCC}(T)$ follows the black curve as expected. At 8.20 K the value of a_v was reverted to 0.5 mm. Then the $M_{FCC}(T)$ was recorded both with increasing the temperature as well as decreasing the temperature. But in both these conditions it trace back the red curve. So the paths of the $M_{FCC}(T)$ for various values of a_v is very robust and distinct in the PMFC region.

Fig. 5.4(b) elucidates the switching behavior of the PMFC region of $M_{FCC}(T)$ at 80 Oe where the black and red curves correspond to a_v of 2 mm and 1 mm, respectively. The blue $M_{FCC}(T)$ curve is initiated above T_{c3}, and cooled down under an applied field of 80 Oe, with an a_v of 1 mm. As the temperature reached 8.29 K, the a_v was changed back and forth from 1 mm to 2 mm, a couple of times. We find that the value of the magnetization coincides with that of the black to red curves. Even when we increase or decrease the temperature of a_v = 2 mm the blue curve traces the black curve. Hence, Fig. 5.4 indicates the stability of the magnetization curves at different a_v even with a small variation of temperature.

Normally, a superconductor placed in an external magnetic field generates the diamagnetic shielding current to screen out the external magnetic field from entering the sample interior. However, the surface layers of the sample has lots of defects which make its T_c to be slightly lower than the bulk of the material [39]. Hence for small applied magnetic fields at a temperature region just below the T_c (of the bulk), it is possible to generate currents in the surface which are in opposite direction to the shielding currents in the bulk. These type of surface currents are generally attributed as paramagnetic currents. The competition between the diamagnetic shielding current and paramagnetic current determines whether the net magnetization will be negative or positive [42].

Generally, to explore the net magnetization, we place the sample inside the detection coils of the S–VSM and vibrate it with an amplitude a_v. If a_v = 0 then the net magnetization is zero because the current loops are not affected. Such a situation is depicted in Fig. 5.5(i).

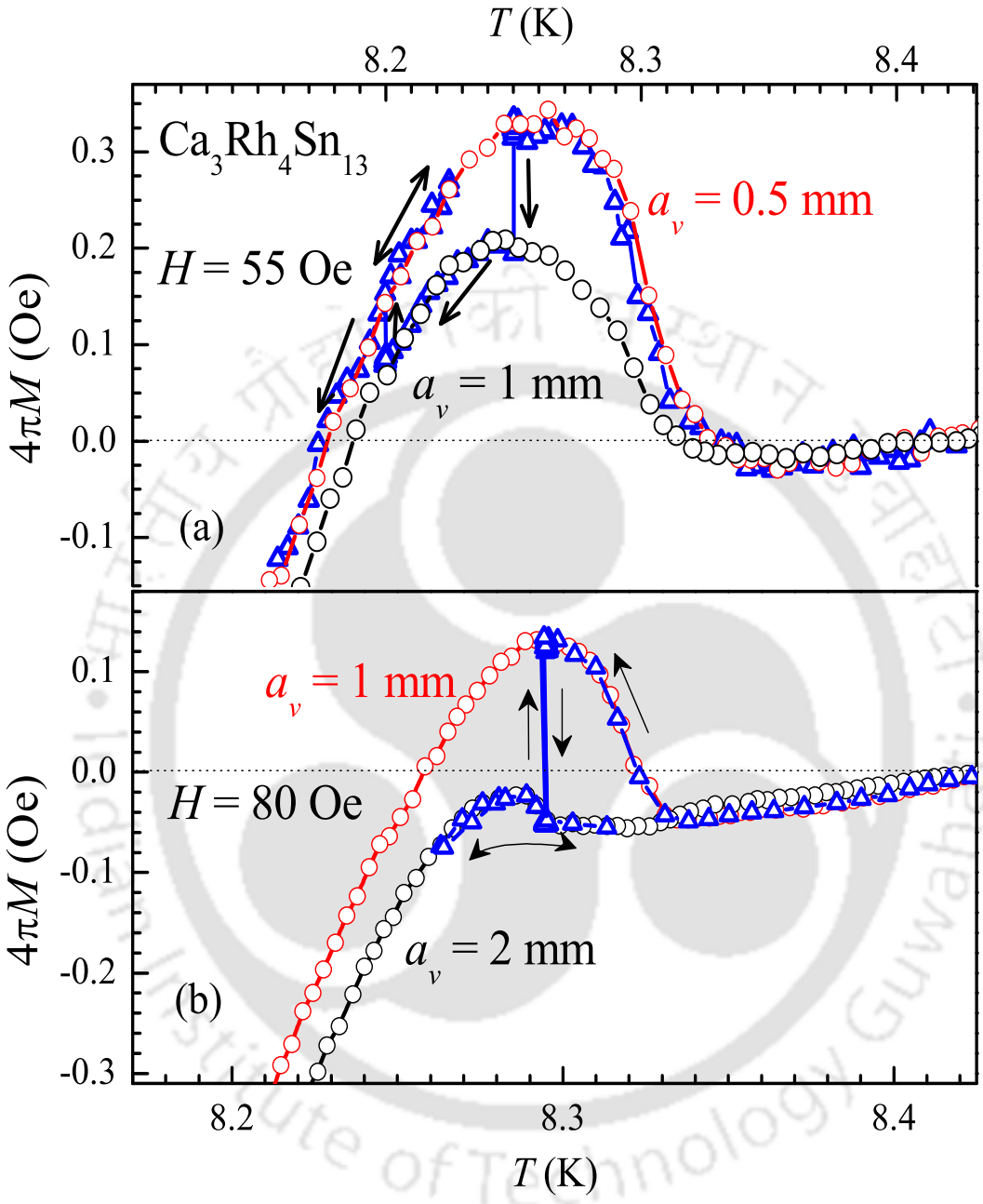

Figure 5.4: *(a) The black and red curves correspond to $M_{FCC}(T)$ curves of a_v values 1 mm and 0.5 mm, respectively, at H = 55 Oe. (b) The black and red $M_{FCC}(T)$ curves correspond to a_v values of 2 mm and 1 mm, respectively at H = 80 Oe. The blue curve in panel (a) and (b) is recorded for observing the thermal stability.*

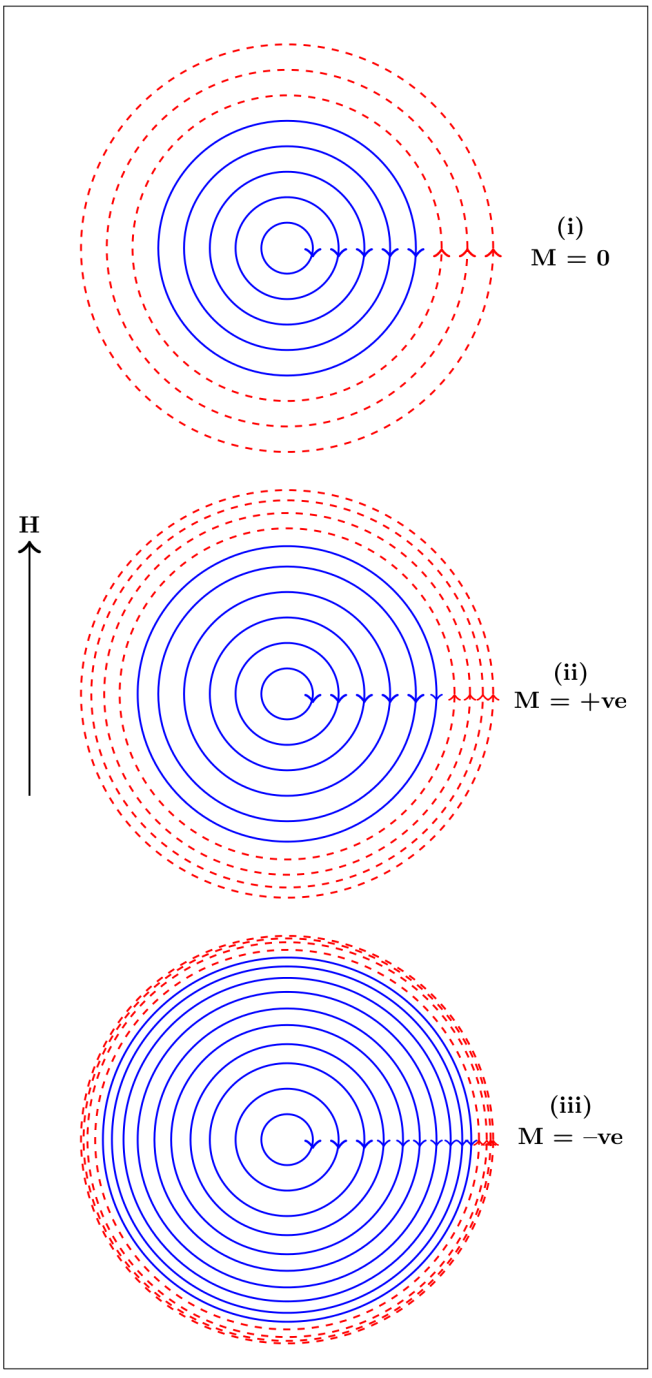

Figure 5.5: *Schematic representation of circulating currents in the superconducting specimen when the net magnetization is (i) zero (ii) paramagnetic (iii) diamagnetic. The red and blue current loops represent the paramagnetic and the diamagnetic currents, respectively.*

Here, the red circles (dotted) represent the paramagnetic current loops and the blue circles (solid) represent the diamagnetic current loops. If we put a small a_v then the paramagnetic current loops representing the surface of the sample are only perturbed as shown in Fig. 5.5(ii) (*cf.* The inter-distance spacing between the red circles are decreased as compared to Fig. 5.5(i)). Hence, the detection coils of the S–VSM receive the signal of a positive magnetization. Now as the value of a_v is increased, it start affecting the currents much deeper inside the sample. This is seen in Fig. 5.5(iii) where both the paramagnetic (red circles) and the diamagnetic shielding currents (blue circles) are affected. If the situation is such that the contribution from the diamagnetic shielding currents (i.e., blue circles) outweighs the contribution of the paramagnetic currents (i.e., red circles) then the net magnetization can be negative as depicted in Fig. 5.5(iii). Hence, this simple model provides a reasonable explanation of the experimental data reported here.

From Fig.s 5.2, 5.3(c) and 5.4(b), it is evident that the present $Ca_3Rh_4Sn_{13}$ single crystal can be used as a magnetic switch. i.e., one can switch the magnetization from paramagnetic to diamagnetic and vice versa by simply changing the a_v of the sample back and forth under a constant H and T in the PMFC region. Also, one can think of designing a binary memory device with the help of $Ca_3Rh_4Sn_{13}$ samples by utilizing the PMFC region by detecting the phase of the magnetization in the PMFC region. For this purpose consider the paramagnetic magnetization as 1 and the diamagnetic magnetization as 0. Mount the sample in a holder and attach it with a vibrating motor. A solenoid can supply a uniform dc magnetic field. By selecting a suitable temperature from the PMFC region, one can detect the flux excluded by the sample with the help of detection coils. By changing the a_v of the motor, one can make 1 or 0 (paramagnetic or diamagnetic magnetization). Therefore, one such crystal of $Ca_3Rh_4Sn_{13}$ in a PMFC state can act as one data bit. By combining eight such crystals (along with vibrating motors and detection coils), one can make a memory of one byte. Therefore, such an array of crystals offers a binary memory device.

5.3 Observation of surface superconductivity in $Ca_3Rh_4Sn_{13}$ single crystal

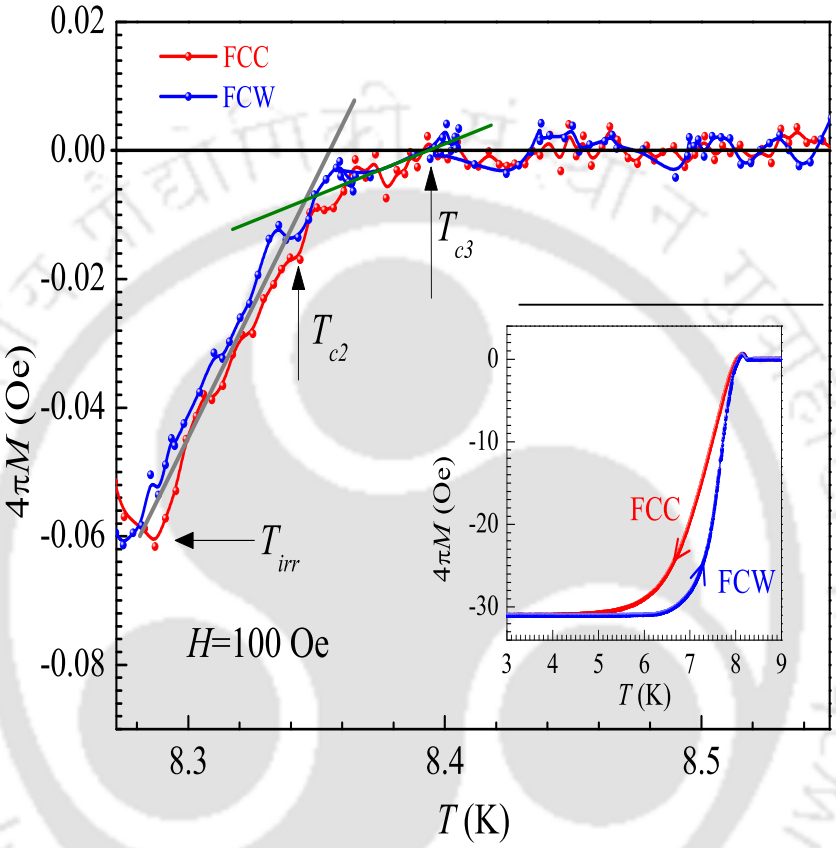

Figure 5.6: *Inset shows the M-T curves at H=100 Oe measured in two different mechanisms - field cooled cool-down (FCC) and field cooled warm-up (FCW). Main panel shows a portion of the high temperature side M-T at 100 Oe, where one can clearly notice the data points T_{irr}, T_{c2} and T_{c3}. The solid lines just indicate the slope change in magnetization data. The gray color solid line helps to predict the position of T_{c2} and the green line helps to predict the position of T_{c3}.*

Inset of Fig. 5.6 shows the magnetization vs. temperature (*M-T*) curves at 100 Oe which are obtained via the field cooled cool-down (FCC) and the field cooled warm-up (FCW) methods. We have marked all important data points by a procedure prescribed elsewhere [120]. The main panel of Fig. 5.6 shows a portion after the PMFC region where one can

notice the irreversibility point, T_{irr}, upper critical temperature point (or superconducting transition temperature), T_{c2} and third critical point, T_{c3}. The irreversibility of the $M_{FCC}(T)$ and $M_{FCW}(T)$ curves ends at the point, T_{irr}. After T_{irr}, we noticed a slope change in *M-T* which we denoted as the upper critical point, T_{c2}. After T_{c2}, the slope changes again indicating the onset of the surface superconductivity, T_{c3}. The diamagnetic region between T_{c2} and T_{c3} is evolved due to the surface superconductivity effects of the $Ca_3Rh_4Sn_{13}$ single crystal.

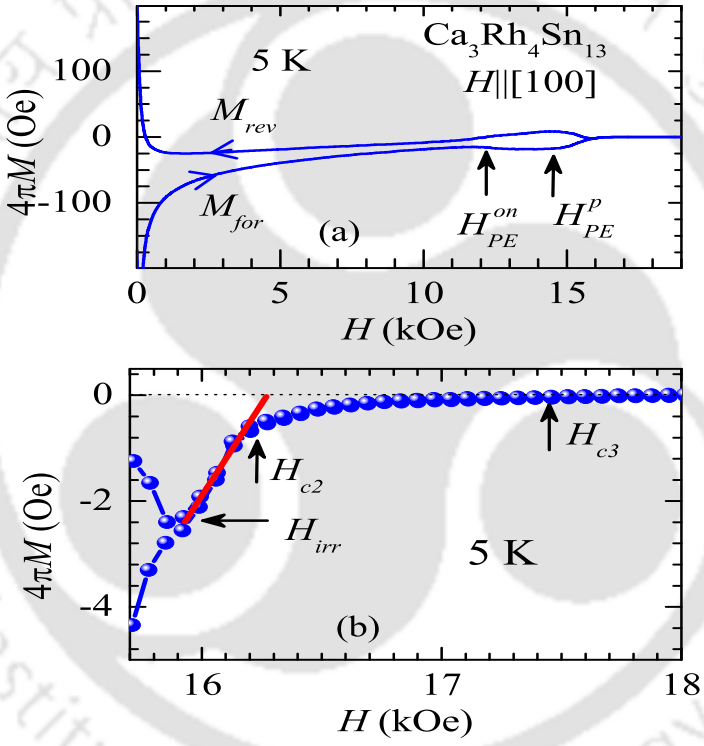

Figure 5.7: *(a) A portion of the isothermal M-H loop at 5 K measured by the stable field mode technique. The forward and reverse magnetization curves are denoted as M_{for} and M_{rev}, respectively. Panel (b) shows the high field side region of the M–H at 5 K. The red line shows the extrapolation of magnetization from H_{irr}, which predicts the position of H_{c2}.*

We have also observed the surface superconductivity effects while performing the isothermal magnetization measurements by the stable field mode technique. Fig. 5.7(a) shows a portion of the *M-H* loop at 5 K (measured by the stable field mode technique) where the anomalous modulations in the forward and reverse magnetization curves represent the PE

phenomenon. The onset and peak fields of the PE anomaly are noted in figure. Fig. 5.7(b) shows the expanded portion of the *M–H* at 5 K where one can see the irreversibility field point (H_{irr}), upper critical field point, H_{c2} and third critical field point, H_{c3}. As expected, the forward and reverse magnetization curves show irreversible nature in the mixed state. The peak effect disappeared at the irreversibility point H_{irr}. In between H_{irr} and H_{c3} there exist a long reversible region. The linear extrapolation of the magnetization line from the H_{irr} determines the H_{c2} (see the red line). The magnetization becomes zero at the H_{c3} field point. The diamagnetic region between H_{c2} and H_{c3} occurs due to the surface superconductivity effect of the superconducting specimen.

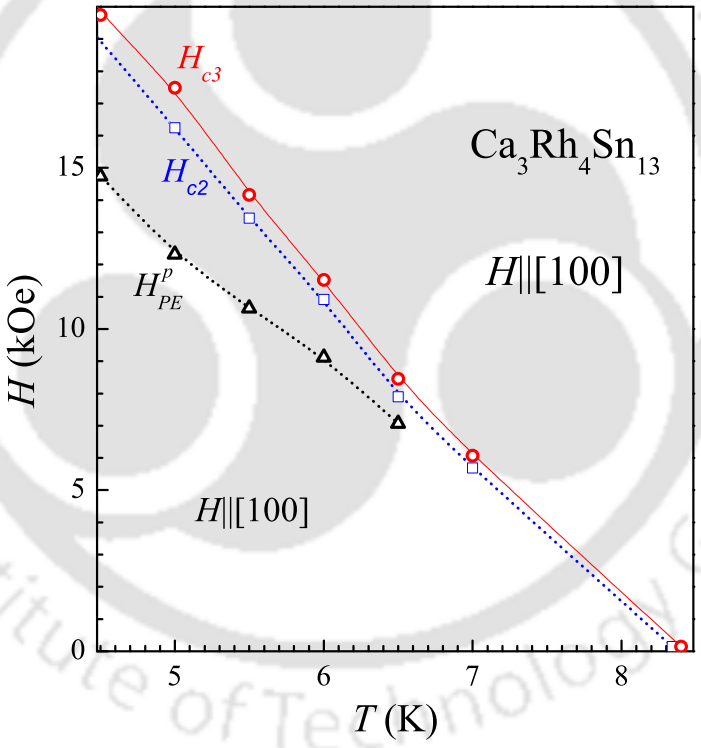

Figure 5.8: *Partial (H-T) phase diagram of the cubic single crystal, $Ca_3Rh_4Sn_{13}$.*

For getting a clear picture of the extent of surface superconductivity effects, we plot the partial (*H, T*) phase diagram (Fig. 5.8) of $Ca_3Rh_4Sn_{13}$ single crystal. The observed PE line is as same as the line obtained from the sweep field mode data (*cf.* Fig. 3.13). All the three curves show monotonic variation of field with increasing temperature. We

observe that the H_{c2} and H_{c3} lines almost merge in the low field, high temperature side. Similar merging behavior of H_{c2} and H_{c3} is observed in a single crystal of Niobium [3]. The field point H_{c3} is a surface enhanced crossover line where one observes the first nucleation of the superconducting islands in the system. Therefore, when superconductivity occurs in $Ca_3Rh_4Sn_{13}$, it tends to nucleate at the surface of the sample, not in the interior. As mentioned in section 1.9, it was predicted that the superconductivity within a surface layer of thickness about the coherence length can exist up to 1.7 H_{c2}, when magnetic field is applied to a superconducting interface of radius of curvature greater than the coherence length [78]. The present $Ca_3Rh_4Sn_{13}$ single crystal shows a value of H_{c3}/H_{c2} as 1.1.

5.4 Summary

In conclusion, we have performed the isofield magnetization measurements in a weakly pinned low T_c superconductor, $Ca_3Rh_4Sn_{13}$ and observed the positive magnetization on field cooling in low applied magnetic fields. We have observed various metastable states in the positive magnetization region of this superconductor. Also, we have provided the experimental evidences for the switching of paramagnetic state to diamagnetic state and vice versa in the positive magnetization region by changing the vibration amplitude of the sample. These crystals can be used in magnetic switching and binary memory device applications. We also observed the signature of surface superconductivity effects in this single crystal.

Chapter 6

Conclusions

After the discovery of high T_c superconductors, vortex phase diagram of low T_c type – II superconductors have been revisited several times to search for similarities/differences with that of the high T_c superconductors. This thesis mainly focused on the results of dc as well as ac magnetization measurements performed in a conventional cubic low T_c superconductor, $Ca_3Rh_4Sn_{13}$. Magnetic measurements in single crystals of $Ca_3Rh_4Sn_{13}$ have shown several interesting features of the vortex matter like second magnetization peak (SMP), peak effect (PE), positive magnetization on field cooling (PMFC) etc.

To emphasize the similarity in the notion of inverse melting in $YBa_2Cu_3O_{7-\delta}$ and $Bi_2Sr_2CaCu_2O_8$ [30, 74] we observe that Bragg glass phase is sandwiched between the vortex glass phase on the low temperature side and an amorphous phase on the high temperature side in the phase diagram. We have shown that an ordered vortex state can be disordered both by enhancement and lowering of temperature. With a small increment of the pinning strength in $Ca_3Rh_4Sn_{13}$ single crystals, the temperature independent nature of the SMP line can be changed to one with a positive slope, resulting in the appearance of an inverse melting region in a portion of the phase diagram. We also observed step changes in equilibrium magnetization across SMP and PE regions which confirms the first order nature of these anomalies. Another noteworthy result which has been revealed is the appearance

of the spinodal line for the Bragg glass/vortex glass transition, which affirms its first order nature.

We have studied the spectral fluctuations in the magnetization data of this single crystal at various regions of the phase space with the help of isothermal magnetization measurements. Two different kinds of resonance frequencies in the power spectra of magnetic fluctuations were observed across the SMP and PE region. It was proved that distinct resonant frequencies are associated with the SMP and PE phenomena. Such low frequency resonances are quite unusual in the vortex lattice. Deep inside the mixed phase $1/f^{1.8}$ nature of the spectral fluctuations were observed. This power law behavior in the noise spectra possibly indicates the self-organized critical nature of the ordered state of the vortex lattice. We have also studied the zero temperature transport analysis of low T_c type – II superconductors with the help of molecular dynamic simulation. Here also we observed a power law nature of the noise in the dynamic phase of the vortices.

We have also studied the metastable effects of the $Ca_3Rh_4Sn_{13}$ single crystals at various regions of the phase space. The difference in the sweep field mode and stable field mode magnetization data of $Ca_3Rh_4Sn_{13}$ is studied. The observed asymmetry in the stable field mode magnetization data directly reveal the existence of two critical current densities in this particular single crystal. The sweep field mode M–H data show high critical current densities due to the underlying metastable vortex lattice configurations. The methods, such as field cooled (FC) minor curves and time relaxed magnetization curves confirm the existence of the two critical current density.

Upon field cooling below T_c under low applied magnetic fields, the $Ca_3Rh_4Sn_{13}$ crystal shows an unusual phenomenon of positive magnetization. We were able to show such phenomena are metastable and the diamagnetism can be reverted by changing the experimental conditions. Further, it is also observed that such metastable states do exist in this field temperature region. In chapter 5, we were able to demonstrate that the switching between these

metastable states or in other words from the positive magnetization state to the negative magnetization state, which can be used in switching devices and binary memory devices.

6.1 Future directions

The present $Ca_3Rh_4Sn_{13}$ single crystals show different vortex phases in its phase diagram. Detailed ac susceptibility measurements may result more information about these vortex phases and this can be done by varying the amplitude and frequency of the ac magnetic field. Transport measurements across different vortex phases also help to probe the characteristics of the vortex matter in its dynamical phase. One can study the characteristics of order-disorder transitions by varying the pins inside the sample. For this purpose one can employ ion-irradiation technique and notice the changes in SMP, PE and PMFC with variation of pins. Small angle neutron scattering (SANS) technique is one of the method to directly visualize the vortices of a superconductor. So employing the SANS experiment helps to gather information about different vortex phases in different experimental conditions.

Appendix A

Crystal structure of $Ca_3Rh_4Sn_{13}$

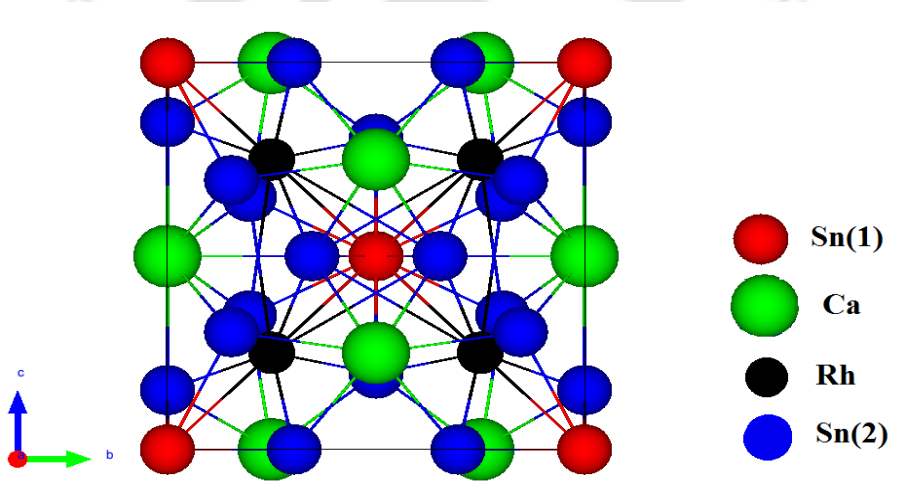

Figure A.1: *Unit cell of $Ca_3Rh_4Sn_{13}$ crystal.*

The crystal structure of $Ca_3Rh_4Sn_{13}$ is isostructural with $Yb_3Rh_4Sn_{13}$ [44, 121, 122]. These are cubic crystals with the space group Pm3n and a lattice parameter of about 9.7 Å. Hodea et al. [121] explained the crystal structure with the help of three dimensional Patterson series. They explained all major peaks in the Patterson series by placing 24 Sn atoms in the 24 fold (0yz) position with y ≈ 2z-0.30, the Rh atoms in the 8-fold {1/4,1/4,1/4} position, the 6 Ca atom in the {1/4,1/2,0} position and 2 Sn atoms in the 2 fold {0,0,0} position of the Pm3n space group.

X-Ray powder diffraction

The crystalline phase identification was done by comparing the experimental XRD patterns to the standards compiled by NIMS data base [123]. Fig. A.2 shows the structurally refined XRD pattern of crystal Y using the standard Rietveld refinement program with the help of

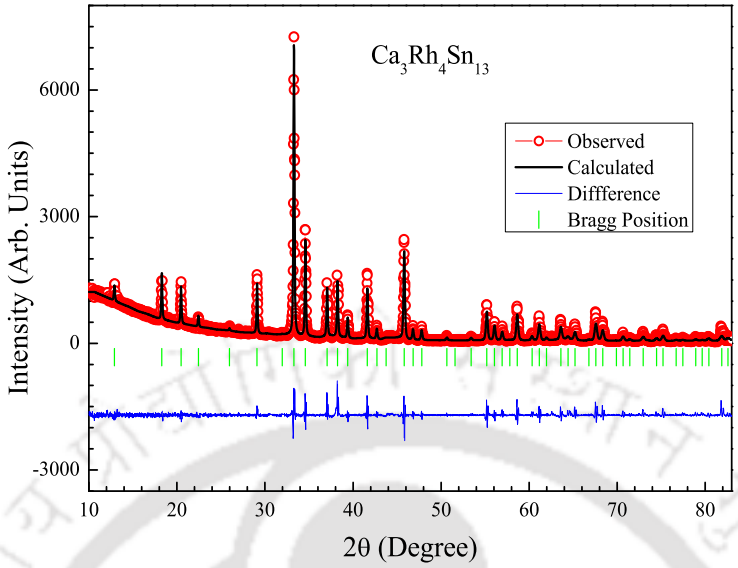

Figure A.2: *Observed and fitted X-ray diffraction pattern of $Ca_3Rh_4Sn_{13}$ crystal (crystal Y).*

Table.1: Crystal parameters obtained from Rietveld refinement

No.	Parameter		Crystal X	Crystal Y
1	Lattice constant, a (Å)		9.700050	9.694633
2	Sn(2) atom coordinates	X	0	0
		Y	0.15338	0.15136
		Z	0.30361	0.30402
3	Bond angles (Degree)	Sn(2)-Sn(1)-Sn(2)	66.2367	66.3713
		Sn(2)-Ca-Sn(2)	67.6114	67.9108
		Sn(2)-Rh-Sn(2)	85.7222	85.3611

Fullprof software. Crystal X shows almost 100% cite occupancy factor for all ions, however, crystal Y shows a 99.82% cite occupancy for Ca ion and 99.78% for Sn(1) ion. Other structural parameters like lattice constant, Sn(2) atom coordinates (other atom coordinates are unaffected) and bond angles which are different in X and Y crystals are shown in the table 1.

From the X-RD refinement data, we observed that the structural parameters of crystal X almost match with the standard $Ca_3Rh_4Sn_{13}$ crystal parameters of NIMS data [123] where as the crystal Y shows a small deviation from it.

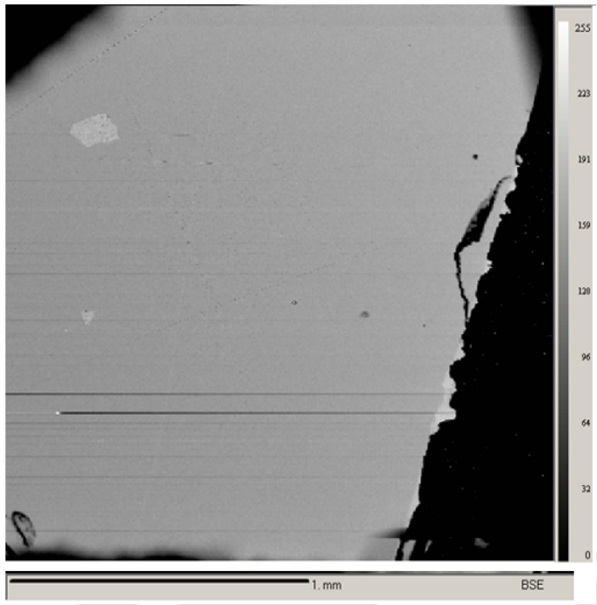

Figure A.3: *Surface image of $Ca_3Rh_4Sn_{13}$ single crystal (crystal Y) obtained from electron probe micro-analyzer*

Analysis of $Ca_3Rh_4Sn_{13}$ single crystal using electron probe micro-analyzer (EPMA)

Further we performed electron probe micro-analyzer (EPMA) measurement in crystal Y for getting the quantitative elemental analysis very precisely. Table 2 shows the results obtained from the EPMA analysis. From table 2, one can see that the atomic percentage of Ca is only 11.45 where the ideal atomic percentage is 15. The atomic percentage of Sn is 68.42 where the ideal atomic percentage is 65.

The properties of the vortex state highly depends on the crystal structure and presence of impurities. From X-RD and EPMA, it is evident that the crystal Y have slightly higher concentration of point disorders. Apart from point disorders other types of disorder like faults, dislocations, etc cannot be ruled out in theses crystals [45].

Table 2: Data obtained from EPMA

Atom	Beam current (nA)	Ix (c/s/nA)	Pk/Bg	Weight%	Norm Weight%		Atomic%
Ca	10.63	219.66	3.74	4.34	4.31		11.45
Rh	10.63	40.16	37.18	19.58	19.45		20.13
Sn	10.63	329.19	92.12	76.75	76.24		68.42
Total				100.67	100		100

Bibliography

[1] J. G. Bednorz and K. A. Müller, Zeitschrift für Physik B Condensed Matter **64**, 189 (1986).

[2] X. S. Ling, S. R. Park, B. A. McClain, S. M. Choi, D. C. Dender, and J. W. Lynn, Phys. Rev. Lett. **86**, 712 (2001).

[3] P. Das, C. V. Tomy, S. S. Banerjee, H. Takeya, S. Ramakrishnan, and A. K. Grover, Phys. Rev. B **78**, 214504 (2008).

[4] S. S. Banerjee, S. Saha, N. G. Patil, S. Ramakrishnan, A. K. Grover, S. Bhattacharya, G. Ravikumar, P. K. Mishra, T. V. C. Rao, V. C. Sahni, et al., Physica C **308**, 25 (1998).

[5] A. M. Troyanovski, M. van Hecke, N. Saha, J. Aarts, and P. Kes, Phys. Rev. Lett. **89**, 147006 (2002).

[6] A. D. Thakur, S. S. Banerjee, M. J. Higgins, S. Ramakrishnan, and A. K. Grover, Phys. Rev. B **72**, 134524 (2005).

[7] D. Jaiswal-Nagar, A. D. Thakur, S. Ramakrishnan, A. K. Grover, D. Pal, and H. Takeya, Phys. Rev. B **74**, 184514 (2006).

[8] P. Das, C. V. Tomy, H. Takeya, S. Ramakrishnan, and A. K. Grover, Physica C **469**, 151 (2009).

[9] S. Sarkar, D. Pal, P. L. Paulose, S. Ramakrishnan, A. K. Grover, C. V. Tomy, D. Dasgupta, B. K. Sarma, G. Balakrishnan, and D. M. Paul, Phys. Rev. B **64**, 144510 (2001).

[10] C. V. Tomy, G. Balakrishnan, and D. M. Paul, Phy. Rev. B **56**, 8346 (1997).

[11] S. Sarkar, P. L. Paulose, S. Ramakrishnan, A. K. Grover, C. V. Tomy, G. Balakrishnan, and D. M. Paul, Phys. C **356**, 181 (2001).

[12] S. Sarkar, D. Pal, S. S. Banerjee, S. Ramakrishnan, A. K. Grover, C. V. Tomy, G. Ravikumar, P. K. Mishra, V. C. Sahni, G. Balakrishnan, et al., Phys. Rev. B **61**, 12394 (2000).

[13] T. Nishizaki and N. Kobayashi, Supercond. Sci. Technol. **13**, 1 (2000).

[14] D. Pal, S. Ramakrishnan, A. K. Grover, D. Dasgupta, and B. K. Sarma, Phy. Rev. B **63**, 132505 (2001).

[15] M. Daeumling, J. M. Seuntjens, and D. C. Larbalestier, Nature (London) **346**, 332 (1990).

[16] B. Khaykovich, E. Zeldov, D. Majer, T. W. Li, P. H. Kes, and M.Konczykowski, Phys. Rev. Lett. **76**, 2555 (1996).

[17] D. Giller, B. Kalisky, I. Shapiro, B. Y. Shapiro, A. Shaulov, and Y. Yeshurun, Physica C **388-389**, 731 (2003).

[18] A. I. Larkin and Y. N. Ovchinnikov, J. Low Temp. Phys. **34**, 409 (1979).

[19] A. I. Larkin and Y. N. Ovchinnikov, Sov. Phys. JETP **38**, 854 (1974).

[20] C. P. Bean, Rev. Mod. Phys. **38**, 36 (1964).

[21] A. B. Pippard, Phil. Mag. **19**, 217 (1969).

[22] T. Nishizaki, T. Naito, S. Okayasu, A. Iwase, and N. Kobayashi, Phy. Rev. B **61**, 3649 (2000).

[23] K. Shibata, T. Nishizaki, T. Sasaki, and N. Kobayashi, Phy. Rev. B **66**, 214518 (2002).

[24] E. Zeldov, D. Majer, M. Konczykowski, V. B. Geshkenbein, V. M. Vinokur, and H. Shtrikman, Nature **375**, 373 (1995).

[25] G. Ravikumar, P. K. Mishra, V. C. Sahni, S. S. Banerjee, S. Ramakrishnan, A. K. Grover, P. L. Gammel, D. J. Bishop, E. Bucher, M. J. Higgins, et al., Phys. C **322**, 145 (1999).

[26] T. Giamarchi and P. L. Doussal, Phys. Rev. Lett. **72**, 1530 (1994).

[27] T. Giamarchi and P. L. Doussal, Phys. Rev. B **52**, 1242 (1995).

[28] T. Giamarchi and P. L. Doussal, Phys. Rev. B **55**, 6577 (1997).

[29] D. T. Fuchs, E. Zeldov, T. Tamegai, S. Ooi, M. Rappaport, and H. Shtrikman, Phy. Rev. Lett. **80**, 4971 (1998).

[30] N. Avraham, B. Khaykovich, Y. Myasoedov, M. Rappaport, H. Shtrikman, D. E. Feldman, T. Tamegai, P. H. Kes, M. Li, M. Konczykowski, et al., Nature **411**, 451 (2001).

[31] M. Marchevsky, M. J. Higgins, and S. Bhattacharya, Nature **409**, 591 (2001).

[32] Y. Paltiel, E. Zeldov, Y. Myasoedov, M. L. Rappaport, G. Jung, S. Bhattacharya, M. J. Higgins, Z. L. Xiao, E. Y. Andrei, P. L. Gammel, et al., Phys. Rev. Lett. **85**, 3712 (2000).

[33] A. Thakur, D. Pal, M. Higgins, S. Ramakrishnan, and A. Grover, Phys. C **466**, 181 (2007).

[34] C. Rastovski, K. J. Schlesinger, W. J. Gannon, C. D. Dewhurst, L. DeBeer-Schmitt, N. D. Zhigadlo, J. Karpinski, and M. R. Eskildsen, Phys. Rev. Lett. **111**, 107002 (2013).

[35] S. Okuma, T. Ichimura, H. Takeya, and K. Hirata, Physica C **469**, 1093 (2009).

[36] S. Okuma, D. Shimamoto, and N. Kokubo, Phys. Rev. B **85**, 064508 (2012).

[37] P. Svedlindh, K. Niskanen, P. Norling, P. Nordblad, L. Lundgren, B. Lonnberg, and T. Lundstrom, Phy. C **162**, 1365 (1989).

[38] W. Braunisch, N. Knauf, V. Kataev, S. Neuhausen, A. Grutz, A. Kock, B. Roden, D. Khomskii, and D. Wohlleben, Phy. Rev. Lett. **68**, 1908 (1992).

[39] P. Kostic, B. Veal, A. P. Paulikas, U. Welp, V. R. Todt, C. Gu, U. Geiser, J. M. Williams, K. D. Carlson, and R. A. Klemm, Phys. Rev. B **53**, 791 (1996).

[40] P. D. Kulkarni, S. S. Banerjee, C. V. Tomy, G. Balakrishnan, D. M. Paul, S. Ramakrishnan, and A. K. Grover, Phys. Rev. B **84**, 014501 (2011).

[41] S. Riedling, G. Brauchle, R. Lucht, K. Rohberg, H. v. Lohneysen, H. Claus, A. Erb, and G. Muller-Vogt, Phys. Rev. B **49**, 13283 (1994).

[42] G. F. Zharkov, Phys. Rev. B **63**, 214502 (2001).

[43] J. P. Remeika, G. P. Espinosa, A. S. Cooper, H. Barz, J. M. Rowell, D. B. McWhan, J. M. Vanderberg, D. E. Moncton, Z. Fisk, L. D. Woolf, et al., Solid State Commun. **34**, 923 (1980).

[44] G. P. Espinosa, Mater. Res. Bull. **15**, 791 (1980).

[45] M. S. Babu, A. Thamizhavel, S. Ramakrishnan, C. V. Tomy, A. K. Grover, and D. Pal, Supercond. Sci. Technol. **26**, 125016 (2013).

[46] U. Essmann and H. Trauble, Phy. Lett. **24A**, 526 (1967).

[47] Michael Tinkham, *Introduction to superconductivity* (Dover publications, Inc, Mineola, NY, 2008).

[48] J. B. Ketterson and S. N. Song, *Superconductivity* (Cambridge University Press U. K., First Edition, 1999).

[49] H. K. Onnes, Leiden Comm. **102b**, 122b (1911).

[50] W. Meissner and R. Ochsenfeld, Naturwissenschaften **21**, 787 (1933).

[51] F. London and H. London, Proc. Roy. Soc. (London) **A149**, 71 (1935).

[52] V. L. Ginzburg and L. D. Landau, Zh. Eksperim. I Teor. Fiz. **20**, 1064 (1950).

[53] J. Bardeen, L. N. Cooper, and J. R. Schrieffer, Phy. Rev. **108**, 1175 (1957).

[54] Charles P. Poole Jr. and Horacio A. Farach and Richard J. Creswick and Ruslan Prozorov, *Superconductivity* (Elsevier Science and Technology Books, 2007).

[55] A. A. Abrikosov, Sov. Phy. JETP **5**, 1174 (1957).

[56] J. Silcox and R. W. Rollins, Appl. Phys. Lett. **2**, 231 (1963).

[57] J. Silcox and R. W. Rollins, Rev. Mod. Phys. **36**, 52 (1964).

[58] R. Labusch, Physics Lett. **22**, 9 (1966).

[59] A. M. Campbell and J. E. Evetts, Adv. Phys. **21**, 199 (1972).

[60] E. H. Brandt, Phys. Rev. B **34**, 6514 (1986).

[61] D. R. Nelson, Phys. Rev. Lett. **60**, 1973 (1988).

[62] D. R. Nelson and H. S. Seung, Phys. Rev. B **39**, 9153 (1989).

[63] J. Kierfeld and V. Vinokur, Phys. Rev. B **69**, 024501 (2004).

[64] G. Blatter, M. V. Feigel'man, V. B. Geshkenbein, A. I. Larkin, and V. M. Vinokor, Rev. Mod. Phy **66**, 1125 (1994).

[65] E. H. Brandt, Rep. Prog. Phys. **58**, 1465 (1995).

[66] T. Giamarchi and S. Bhattacharya, in *High Magnetic Fields*, edited by L. P. L. C. Berthier and G. Martinez (Springer, 2002), pp. 314–360.

[67] T. Giamarchi and P. L. Doussal, cond-mat/9705096 (1997).

[68] D. G. Grier, C. A. Bolle, P. L. Gammel, D. J. Bishop, D. B. Mitzi, and A. Kapitulnik, Phys. Rev. Lett. **66**, 2270 (1991).

[69] A. I. Larkin, Sov. Phys. JETP **31**, 784 (1974).

[70] W. A. Fietz and W. W. Webb, Phy. Rev. B **178**, 657 (1969).

[71] A. M. Troyanovski, M. van Hecke, N. Saha, J. Aarts, and P. H. Kes, Phys. Rev. Lett. **89**, 712 (2001).

[72] D. S. Fisher, M. P. A. Fisher, and D. A. Hue, Phys. Rev. B **43**, 130 (1991).

[73] S. Kokkaliaris, P. A. J. de Groot, S. N. Gordeev, A. A. Zhukov, R. Gagnon, and L. Taillefer, Phys. Rev. Lett. **82**, 5116 (1999).

[74] D. Pal, S. Ramakrishnan, A. K. Grover, D. Dasgupta, and B. K. Sarma, Supercond. Sci. Technol. **15**, 258 (2002).

[75] S. Banerjee, A. K. Grover, M. J. Higgins, G. I. Menon, P. K. Mishra, D. Pal, S. Ramakrishnan, T. V. C. Rao, G. Ravikumar, V. C. Sahni, et al., Phy. C **355**, 39 (2001).

[76] S. Banerjee, S. Ramakrishnan, D. Pal, S. Sarkar, A. K. Grover, G. Ravikumar, P. K. Mishra, T. V. C. Rao, V. C. Sahni, C. Tomy, et al., J. Phy. Soc. Jpn **69**, 262 (2000).

[77] D. Saint-James and G. Sarma and E. J. Thomas, *Type - II superconductivity* (Pergamon Press Ltd., Headington Hill Hall, Oxford, 1969).

[78] D. Saint-James and P. G. de Gennes, Phys. Lett. **7**, 306 (1963).

[79] W. Braunisch, N. Knauf, G. Bauer, A. Kock, A. Becker, B. Freitag, A. Grutz, V. Kataev, S. Neuhausen, B. Rodin, et al., Phys. Rev. B **48**, 4030 (1993).

[80] M. Sigreist and T. M. Rice, Rev. Mod. Phy. **67**, 503 (1995).

[81] D. Dominguez, E. A. Jagla, and C. A. Balseiro, Phys. Rev. Lett. **72**, 2773 (1994).

[82] D. J. Thompson, M. S. M. Minhaj, L. E. Wenger, and J. T. Chen, Phys. Rev. Lett. **75**, 529 (1995).

[83] A. E. Koshelev and A. I. Larkin, Phys. Rev. B **52**, 13559 (1995).

[84] V. V. Moshchalkov, X. G. Qiu, and V. Brundoncx, Phys. Rev. B **55**, 11793 (1997).

[85] G. Ravikumar and H. Kupfer, Phys. C **402**, 67 (2004).

[86] W. Henderson, E. Y. Andrei, M. J. Higgins, and S. Bhattacharya, Phys. Rev. Lett. **77**, 2077 (1996).

[87] B. Sas, F. Portier, K. Vad, B. Keszei, L. F. Kiss, N. Hegman, I. Puha, S. Meszaros, and F. I. B. Williams, Phys. Rev. B **61**, 9118 (2000).

[88] A. D. Thakur, S. S. Banerjee, M. J. Higgins, S. Ramakrishnan, and A. K. Grover, Pramana–Journal of Physics **66**, 159 (2006).

[89] S. S. Banerjee, N. G. Patil, S. Ramakrishnan, A. K. Grover, S. Bhattacharya, G. Ravikumar, P. K. Mishra, T. V. C. Rao, V. C. Sahni, and M. J. Higgins, Appl. Phys. Lett. **74**, 126 (1999).

[90] Y. Paltiel, E. Zeldov, Y. N. Myasoedov, H. Shtrikman, S. Bhattacharya, M. J. Higgins, Z. L. Xiaok, E. Y. Andreik, P. L. Gammel, and D. J. Bishop, Nature **403**, 398 (2000).

[91] D. Kulkarni, M. Singh, D. Karmakar, T. C. Rao, P. Mishra, G. Ravikumar, K. Bhagwat, and H. Kupfer, Phys. C **385**, 346 (2003).

[92] G. Ravikumar, V. C. Sahni, A. K. Grover, S. Ramakrishnan, P. L. Gammel, D. J. Bishop, E. Bucher, M. J. Higgins, and S. Bhattacharya, Phys. Rev. B **63**, 024505 (2000).

[93] S. S. Banerjee, N. G. Patil, S. Ramakrishnan, A. K. Grover, M. J. Higgins, C. V. Tomy, G. Balakrishnan, and D. M. Paul, Phys. Rev. B **59**, 6043 (1999).

[94] N.W. Ashcroft and N.D. Mermin, *Solid State Physics* (Thompson, First Edition, 2003).

[95] X.S Ling and J. I. Budnick, *Magnetic susceptibility of superconductors and other spin systems* (Plenum Press, New York., First Edition, p.377, 1991).

[96] D. Pal, S. Ramakrishnan, and A. K. Grover, Phy. Rev. B **65**, 096502 (2002).

[97] M. V. Marchevsky, Ph.D. thesis, University of Leiden, The Netharlands (1997).

[98] Z. L. Xiao, O. Dogru, E. Y. Andrei, P. Shuk, and M. Greenblatt, Phy. Rev. Lett **92**, 227004 (2004).

[99] T. Nishizaki, N. Tomoyuki, and K. Norio, Phy. Rev. B **58**, 11169 (1998).

[100] N. Morozov, E. Zeldov, D. Majer, and M. Konczykowski, Phy. Rev. B **54**, R3784 (1996).

[101] S. Mohan, J. Sinha, S. S. Banerjee, A. K. Sood, S. Ramakrishnan, and A. K. Grover, Phys. Rev. Lett. **103**, 167001 (2009).

[102] P. Bak, C. Tang, and K. Wiesenfeld, Phys. Rev. Lett. **59**, 381 (1980).

[103] S. Field, J. Witt, F. Nori, and X. Ling, Phys. Rev. Lett. **74**, 1206 (1995).

[104] C. Reichhardt, C. J. O. Reichhardt, I. Martin, and A. R. Bishop, Phy. Rev. Lett. **90**, 026401 (2003).

[105] M. Chandran, R. T. Scalettar, and G. T. Zimanyi, Phy. Rev. B **67**, 052507 (2003).

[106] X. B. Xu, H. Fangohr, S. Y. Ding, F. Zhou, X. N. Xu, Z. H. Wang, M. Gu, D. Q. Shi, and S. X. Dou, Phy. Rev. B **83**, 014501 (2011).

[107] M. P. Allen and D. J. Tildesley, *Computer Simulation of Liquids* (Clarendon Press, Oxford Science Publications, 1989).

[108] D. K. Christen, H. R. Kerchner, S. T. Sekula, and P. Thorel, Phy. Rev. B **21**, 102 (1980).

[109] B. Obst, Phys. Lett. A **28**, 662 (1969).

[110] M. Yethiraj, D. K. Christen, D. M. Paul, P. Miranovi, and J. R.Thompson, Phys. Rev. Lett. **82**, 5112 (1999).

[111] C. D. Dewhurst, S. J. Levett, and D. M. Paul, Phys. Rev. B **72**, 014542 (2005).

[112] D. Cribier, Y. Simon, and P. Thorel, Phys. Rev. Lett. **28**, 1370 (1972).

[113] C. Rastovski, K. J. Schlesinger, W. J. G. snd C. D. Dewhurst, L. DeBeer-Schmitt, N. D. Zhigadlo, J. Karpinski, and M. R. Eskildsen, Phys. Rev. Lett. **108**, 167001 (2013).

[114] S. J. Levett, Ph.D. thesis, University of Warwick, Coventry CV4 7AL, UK (2003).

[115] M. Wertheimer and J. le G. Gilchrist, J. Phys. Chem. Solids **74**, 184514 (1967).

[116] D. Dominguez, E. A. Jagla, and C. A. Balseiro, Phys. Rev. Lett. **72**, 2773 (1994).

[117] M. S. Li, Phy. Rep. **376**, 133 (2003).

[118] F. V. Kusmartsev, Phys. Rev. Lett. **69**, 2268 (1992).

[119] A. K. Geim, S. V. Dubonos, J. G. S. Lok, M. Henini, and J. C. Maan, Nature **396**, 144 (1998).

[120] S. Kumar, A. D. Thakur, R. Singh, A. Thamizhavel, C. V. Tomy, and A. K. Grover, AIP Conf. Proceedings **1447**, 909 (2012).

[121] J. L. Hodeau, J. Chenavas, M. Marezio, and J. P. remeika, Solid State Comm. **36**, 839 (1980).

[122] J. L. Hodeau, M. Marezio, J. P. remeika, and C. H. Chen, Solid State Comm. **42**, 97 (1982).

[123] http://tinyurl.com/pe3qee9 (URL).